

Simulation of HV-CMOS detectors for beam monitoring in particle therapy (Simulation von HV-CMOS Detektoren zur Strahlüberwachung in der Teilchentherapie)

Master thesis
of

Pietro Marchesi

at the Institute of Experimental Particle Physics

Reviewer:	Prof. Dr. Ulrich Husemann
Second Reviewer:	Prof. Dr. Markus Klute
Advisor:	Dr. Alexander Dierlamm
Second Advisor:	Bogdan Topko

Research period: 02.12.2023 – 03.06.2024

ETP-KA/2024-03

Erklärung zur Selbstständigkeit

Ich versichere wahrheitsgemäß die Arbeit selbstständig verfasst, alle benutzten Hilfsmittel vollständig und genau angegeben und alles kenntlich gemacht zu haben, was aus Arbeiten anderer unverändert oder mit Abänderungen entnommen wurde sowie die Satzung des KIT zur Sicherung guter wissenschaftlicher Praxis in der jeweils gültigen Fassung beachtet zu haben.

Karlsruhe, den 29.05.2024, _____
Pietro Marchesi

Abstract

At the present time, cancer continues to be a disease affecting an ever increasing number of people and for which we have not found a definitive cure. This is not helped by the fact that the word cancer encompasses a vast variety of conditions, each affecting different organs and with distinct physiological characteristics. As diverse as these illnesses are, so too are the therapeutic measures taken to combat them.

Along the commonly known therapies for cancer, e.g. radio- and chemotherapy, there is an emerging treatment option: ion therapy. A beam of ionizing particles (like protons or carbon ions) can be used to induce the death of cancerous cells. It has the advantage of better preserving healthy tissues by concentrating the energy deposition on the malignant cells. This is possible thanks to the peculiar energy absorption curve of accelerated massive particles in matter in comparison to photons. A precise beam monitoring system is required in order to ensure that the energy is deposited exactly where it is needed to induce the death of the aforementioned malignant formations, and not elsewhere, and therefore to avoid unnecessary irradiation of the patient. One possibility to achieve that goal is by using semiconductor detectors, in particular the High-Voltage Complementary Metal–Oxide–Semiconductor (HV-CMOS) detectors.

This work will concentrate on some aspects of the development of such technology for medical applications, including the developing of appropriate simulations using the Allpix² framework, as well as a radiation hardness evaluation of the system. In the scope of this project, a graphical user interface also designed to operate the detectors by consolidating the already available Python scripts (developed by Bogdan Topko and Martin Pittermann).

The detector is being developed in cooperation with the Heidelberg Ion-Beam Therapy Center (HIT) with the prospect of replacing the current beam monitoring system comprised of multi-wire chambers with semiconductor devices. The latter show some key benefits in comparison to the former: faster response time (critical for the safety of the patient in case of malfunctions), higher resistance to vibrations in noisy environments and the possibility of operation inside magnetic fields [1].

Contents

1. Introduction	1
1.1. Why ion therapy?	1
1.2. The Heidelberg Ion-Beam Therapy Center: Beam monitoring system	3
1.2.1. Requirements for a beam monitoring system	4
1.3. High-Voltage CMOS detectors	5
1.3.1. Silicon detectors	5
1.3.2. The pn-junction	7
1.3.3. CMOS detectors	8
1.4. Radiation damage in silicon sensors	9
1.4.1. Bulk damage	9
1.4.2. Surface damage	9
1.4.3. Annealing	9
1.5. Fluence and energy dose	10
1.6. The HitPix detector	10
2. Sentaurus TCAD simulations	13
2.1. Geometry models	13
2.1.1. ISO topology	14
2.1.2. STD topology	15
2.2. Sentaurus Device module	15
2.2.1. File	15
2.2.2. Electrodes	15
2.2.3. Physical models	16
2.2.4. Plots	17
2.2.5. Math	17
2.2.6. Solve	18
2.2.7. Radiation damage	19
2.2.7.1. Bulk damage	19
2.2.7.2. Surface damage model	20
2.3. Charge carrier lifetime in the SRH Model	22
2.4. Electric fields	24
2.4.1. ISO topology	24
2.4.2. STD topology	24
2.5. Leakage current	26
2.6. Conclusions	27
3. Allpix Squared simulations and beam profile reconstruction	29
3.1. Motivation	29
3.2. Beam profile reconstruction	31
3.2.1. Interpolation	31
3.2.2. Reconstruction algorithms	33

3.3.	Allpix Squared simulations	36
3.3.1.	Configuration	36
3.3.2.	STD topology: systematic shift	39
3.3.3.	Charge collection in irradiated sensors	40
3.3.4.	Detector efficiency and cluster size on irradiated sensors	41
3.3.5.	Algorithm validation	44
3.3.5.1.	Matrix alignment	45
3.3.5.2.	Online reconstruction	46
3.3.5.3.	Performance of the simple algorithm with respect to the Gaussian fit in experimental data	49
3.3.5.4.	Simple algorithm's performance in simulations	49
3.3.6.	Limits of the interpolation algorithm	51
3.3.7.	5x5 matrix geometry simulation, alignment precision	53
3.3.8.	Algorithm performance in a simulated 5x5 matrix	54
3.4.	Conclusions	57
4.	Graphical user interface for the HitPix detectors	59
4.1.	Home screen	59
4.1.1.	Configuration section	59
4.1.2.	Data acquisition section	60
4.1.2.1.	Advanced settings	61
4.1.3.	Plotting section	61
4.2.	IV-curve measurement tool	63
4.3.	S-curve measurement tool	65
4.4.	DAC-tuning tool	68
5.	Conclusions and outlook	71
Appendix		73
A.	Sentaurus simulations	73
A.1.	Pixel topologies and geometry models	73
A.2.	Sentaurus graphical interface	76
B.	AllPix Squared simulations	76
B.1.	Interpolation	76
B.2.	Time of arrival	76
B.3.	Real 2x5 geometry	76
B.4.	Reconstruction without de-noising	78
B.5.	Detector definition	78
Bibliography		81

List of Figures

1.1. Bragg peak: Dose deposited in dependence on the depth	2
1.2. Real treatment plan with carbon ions for a glioblastoma	3
1.3. Current beam monitoring setup at HIT	4
1.4. Silicon band structure	6
1.5. Silicon lattice width and without impurities	6
1.6. Carrier concentration on a pn-junction	7
1.7. Structure of and signal generation on a CMOS sensor	8
1.8. Render of the final HitPix 13×13 array	10
1.9. Schematic illustration of the HitPix pixel electronics	11
1.10. Pixel readout modes	11
1.11. Adders projection in HitPix3	12
1.12. Elements of the HitPix data acquisition system	12
2.1. Pixel topologies of the HitPix detector family	14
2.2. Adjustment of the SRH lifetime to experimental data	23
2.3. Electric fields for the ISO and STD topology	25
2.4. Depth dependency of the z -component of the electric field for the ISO topology	25
2.5. Depth dependency of the z -component of the electric field for the STD topology	26
2.6. Simulated leakage current for ISO topology pixels a function of the bias voltage before and after irradiation	27
3.1. HitPix 5×5 mockup	29
3.2. Histogram of hits in adders mode for an 1×5 HitPix 2 array	30
3.3. Visualisation of the interpolation algorithm in adders mode	32
3.4. Real 2×5 geometry in adders mode before and after interpolation	33
3.5. Systematic deviation in the position reconstruction with STD topology . . .	40
3.6. Pixel charge in irradiated and non-irradiated sensors	41
3.7. Efficiency maps of ISO sensors before and after irradiation	43
3.8. Cluster size in ISO sensors before and after irradiation	43
3.9. Profile reconstruction from experimental data at HIT - Width overestimation	44
3.10. 2×5 matrix alignment	45
3.11. Beam intensity profile at HIT	46
3.12. Reconstruction performance in online mode - Exponential rolling average .	48
3.13. Position and width deviations of the simple algorithm from results using the Gaussian algorithm in experimental data of the 2×5 matrix	49
3.14. Position and width deviations of the simple algorithm from results using the Gaussian algorithm in simulated data of the 2×5 matrix	50
3.15. Position and width deviations for variable gap size	52
3.16. Position and rotation misalignments measured from a 5×5 array mockup . .	53
3.17. Position reconstruction deviation in a simulated 5×5 matrix for different scenarios	55
3.18. Width reconstruction deviation in a simulated 5×5 matrix for different scenarios	56

4.1.	GUI's homepage	60
4.2.	GUI during data acquisition	61
4.3.	GUI's homepage: Scan settings menu for a HitPix 3 detector	62
4.4.	GUI dataset viewer	63
4.5.	GUI's IV-curve measurement tool	64
4.6.	GUI S-curve measurement tool	66
4.7.	GUI's S-curve measurement tool with expanded menus	66
4.8.	GUI S-curve plot	67
4.9.	DAC tuning tool	69
A.1.	Sentaurus mesh for the ISO topology	73
A.2.	STD pixel structure with dimensions	74
A.3.	ISO pixel structure with dimensions	75
A.4.	Overview of the Sentaurus Workbench interface	76
B.5.	Section of an interpolated 5x5 matrix with adders profiles	77
B.6.	Time of arrival histogram	77
B.7.	Real 2x5 geometry and coordinate system used for matrix alignment	78
B.8.	Width reconstruction without de-noising	78

List of Tables

1.1. Beam parameters at HIT	3
2.1. Bulk radiation damage model	20
2.2. Perugia 2019 Surface Damage Model	21
2.3. SRH lifetime model	23
3.1. Simulation settings: STD topology systematic shift	40
3.2. Simulation settings: Test of charge collection on irradiated and non-irradiated sensors	41
3.3. Simulation settings: Test of the detector's efficiency and cluster size	42
3.4. Simulation settings: Algorithm validation with HitPix 2 2×5 matrix	44
3.5. Simulation settings: Test of the interpolation algorithm for different gap widths	51
3.6. Simulation settings: 5×5 matrix simulation	54

1. Introduction

This thesis explores different aspects of the development of the HitPix detector family, which are HV-CMOS detectors intended for beam monitoring at an ion therapy facility. The usefulness of this therapy is motivated in the first chapter, which also presents some important theoretical backgrounds and the design concept of the HitPix detectors.

One of the main goals is to design a simulation framework able to predict the behaviour of the HitPix sensors under irradiation, for which an adequate model of the charge propagation within the sensor is crucial. Therefore, chapter 2 is dedicated to the computation of the electrical fields under reversed bias condition for the two topologies of HitPix and describes the settings and assumptions made to perform said simulations. The effects of radiation damage on those fields are also explored by implementing models for surface and bulk damage and recomputing the fields for the scenario of radiation damaged sensors. The results of chapter 2 serve as an input for the detector simulation framework developed using Allpix Squared in chapter 3.

Since the HitPix detectors are expected to be used in beam monitoring, robust and fast algorithms have to be implemented to reconstruct two main beam characteristics: its position and its width. The algorithm development and its testing in real data as well as in simulated scenarios using the Allpix Squared framework are discussed in chapter 3. Some other important aspects of the sensors like their efficiency and cluster size before and after irradiation are also briefly explored within that chapter.

Lastly, a graphical user interface (GUI) is designed to consolidate the already available python scripts (used to operate the data acquisition system from the command console) into an user friendly and flexible interface. An user manual to that interface is provided in chapter 4.

1.1. Why ion therapy?

One of the standard treatments for malignant tumors is irradiation with photons to trigger cell death in the affected tissues. The energy is deposited via photon-matter interactions along the beam path. This process depends on the depth within the patient. Such a dependence is depicted in figure 1.1, and shows the key difference between an irradiation with charged ions and with photons: photons transfer significant amounts of energy to the tissue prior to reaching the tumor. Ions, on the other hand, exhibit a peak in energy transfer at a certain depth (Bragg peak), which avoids deposition on healthy tissue, specially after the tumor thanks to the steep fall of the curve after the peak.

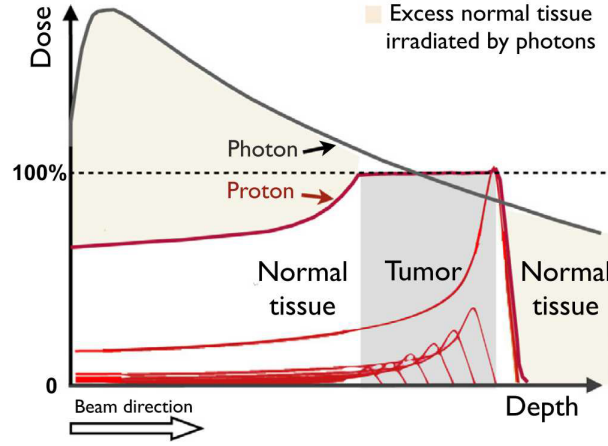


Figure 1.1.: Dose deposited in tissue in dependence on the depth (from [1]). For photons (black curve), the tissue before the tumor receives a high dose. For protons, the highest deposition takes place at a certain depth (Bragg-peak) depending on the energy of the beam. Proton beams can be combined over a range of energies to achieve an homogeneous deposition over the tumor. [1][2]

Furthermore, ion radiotherapy has the benefit of producing more complex damage to the DNA thanks to the greater Linear Energy Transfer (LET) of ions in comparison with photons. DNA damage from ions can arise, for example, from single- and double-strand breaks and base pair damage. Clustered multiple double strand breaks, specially, are thought to be responsible for a higher rate of cell death (since this kind of DNA damage are very difficult to repair) and further motivates the use of ions for tumor therapy. [3]

The origin of the Bragg peak lies in the energy loss of massive particles through a material. The mean energy loss per path length within a material is described in the case of protons in the range $0.1 \leq \beta\gamma \leq 1000$ by the Bethe equation:

$$\left\langle -\frac{dE}{dx} \right\rangle = \frac{Kz^2Z}{A\beta^2} \left[\frac{1}{2} \ln \frac{2m_e c^2 \beta^2 \gamma^2 W_{\max}}{I^2} - \beta^2 - \frac{\delta(\beta\gamma)}{2} \right] \quad (1.1)$$

Here, K is a constant, z and Z the charge number of incident and absorber particles respectively, A the atomic mass of the absorber, β the light speed normalized velocity, γ the relativistic Lorentz factor, m_e the electron mass, W_{\max} the maximum energy transfer of an electron in a single collision, I the mean excitation energy and $\delta(\beta\gamma)$ a density effect correction [4].

The key aspect which can be derived from the Bethe equation is that, during its passage through matter, the particle loses energy and hence speed, increasing the energy loss per unit path length. That is the reason why the most energy is deposited at the end, since the velocity of the particle is lowest.

The importance of the Bragg peak and its relevance for cancer treatment becomes clear, for instance, in cases where the tumor lies within the brain and as much healthy tissue as possible has to be preserved. A real treatment plan for one of such cases is shown in figure 1.2. In this case, the treatment was performed at the Heidelberg Ion-Beam Therapy Center (HIT) with carbon ions. The 50-year-old patient showed a remarkable improvement six weeks after the treatment with no loss on neurological stability [5].

Cases like the one presented in figure 1.2 reveal not only the utility of the procedure, but also the paramount importance of ensuring that the beam trajectory and width are under tight control. Deviations in these parameters can lead to irradiation and subsequent damage of vital tissue, e.g. the brain stem.

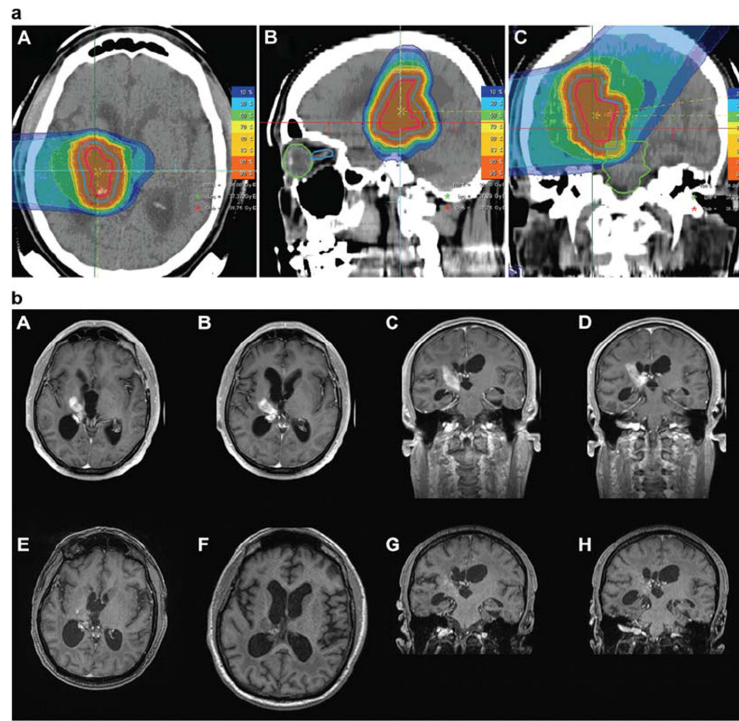


Figure 1.2.: Treatment plan with carbon ions (a) and results for a glioblastoma (b) (from [5]). Subfigure (a) shows the dose in different areas surrounding the lesion, the pictures A-C are different projections of the patient's head. Warmer colours indicate higher dose. The pictures A-D in subfigure (b) show images before the treatment, the last row 6 weeks after the treatment. Notice the disappearance of the tumor (white lesion). [5]

Table 1.1.: Energy, intensity and full width at half maximum (FWHM) ranges for proton and carbon ion beams at HIT

	Protons	Carbon ions
Energy (MeV/u)	48 – 221	89 – 430
Intensity (1/s)	$8 \cdot 10^7 - 2 \cdot 10^{10}$	$2 \cdot 10^6 - 5 \cdot 10^8$
FWHM (mm)	8.1 – 32.9	3.4 – 20

1.2. The Heidelberg Ion-Beam Therapy Center: Beam monitoring system

The Heidelberg Ion-Beam Therapy Center (HIT) is a facility located at the Heidelberg University Hospital consisting of a synchrotron (which accelerates ions) and three therapy rooms. Carbon ions and protons are the common choice for treatments [1]. HIT began operations in 2009 irradiating the first patient in November of that year [6].

The accelerator and beam guiding systems are designed to deliver protons and carbons at 255 different energy steps, six different widths and fifteen intensities. The width and intensity at which a beam can be configured depends on the selected energy range. A table with ranges for the available energy, intensity and width is presented in table 1.1.

Currently, a set of two multi-wire proportional chambers (MWPCs) with a 2 mm channel pitch is operated in a perpendicular configuration to measure the beam position and width in x - and y -directions. Ionisation chambers (ICs) are employed to monitor the beam intensity (and, hence, the dose to the patient) [1]. A picture of the setup is provided in figure 1.3.

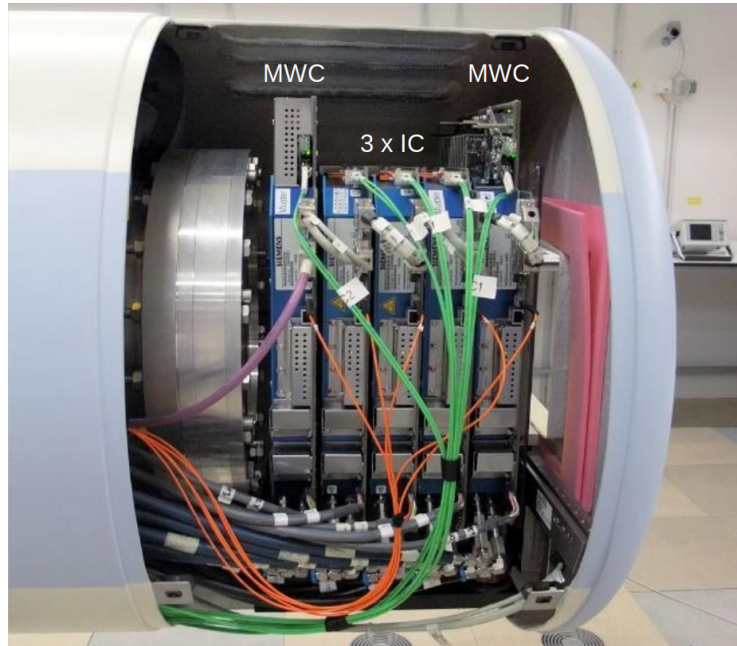


Figure 1.3.: Beam monitoring setup at HIT: two MWPCs (left and right, labeled as MWC) and three ICs (center). Modified from [7], originally from Ivan Perić.

1.2.1. Requirements for a beam monitoring system

A monitoring system for clinical purposes should be capable of giving accurate enough feedback about the radiation reaching the patient, not only because of safety reasons, but also to ensure that the treatment plan is performed adequately as to increase its healing properties and reduce the side effects. Some important aspects to consider and desired specifications for the upcoming beam monitoring concept at HIT are (after [1]):

- **Spatial resolution:** Expected to be better than $200\ \mu\text{m}$ (current resolution achievable by the MWPC).
- **Measurement of the beam width:** Expected to be better than 10% for a Gaussian profile. For the duration of this work, a beam width resolution of $400\ \mu\text{m}$ is strived for.
- **Feedback speed:** The reconstruction of the beam position and width is expected to occur within $100\ \mu\text{s}$ and relied to the control interface in a time span no greater than $100\ \mu\text{s}$.
- **Radiation hardness:** During normal clinical operation, the detector is not expected to be irradiated homogeneously, but to receive a higher 1-MeV neutron equivalent fluence (see section 1.5) mainly in the middle of approximately $3 \times 10^{14}\ \text{cm}^{-2}$ with carbon ions and $3 \times 10^{15}\ \text{cm}^{-2}$ with protons. The detector is expected to withstand these conditions for five years. The replacement procedures of the detector system after this time period is not to take longer than one day, more regular maintenance should be possible in less than a couple of hours.

More detailed information and requirements can be found in [1].

1.3. High-Voltage CMOS detectors

1.3.1. Silicon detectors

Silicon detectors are solid state detectors widely used in high energy particle physics, among other fields. Their working principle is the collection of charge carriers generated within the silicon volume by an ionisation event.

In solid state lattices, the discrete energy levels of the electrons overlap to form so-called energy bands representing an interval of possible energies that an electron is allowed to possess. For the electronic properties of solid state bodies, two bands are usually relevant: the conduction and the valence band. Within the valence band, electrons do not have enough energy to be assumed as free, since they are tightly bound to the atomic nucleus. Within the conduction band, on the contrary, electrons have additional energy which allows them to propagate more or less freely through the atomic lattice. There may be an energy interval between the conduction and the valence band for which no states are available. This is often referred to as a band gap. If the gap is sufficiently wide, no transitions from the valence to the conduction band are possible, leading to an unpopulated conduction band and, therefore, to an insulator material. On the other hand, the aforementioned bands may overlap, favoring the population of the conduction band and hence electrical conductivity. This is the case of electrically conductive materials like metals. Finally, an intermediate case may present in which there is a band gap but the energy difference is overcomable by an appropriate excitation of the electrons, like in the case of an ionisation event. In this instance, we speak about semiconductor materials.

The transition of an electron between two states can be triggered by different energy absorption or emission processes. Thermal excitation may be enough to bring an electron to an energy state which is close by, for example. However, for the electron to jump to or from energy states which are farther apart usually photon and phonon absorption or emission may be required. Furthermore, an ionising particle can impart the necessary energy to an bound electron in the valence band for it to jump into the conduction band. A given transition may occur between electron states with different energy but same momentum via a photon absorption, in which case we speak about a *direct transition*. However, sometimes the states do not have the same momentum, hence needing the coupling to a phonon to transfer the momentum difference. This is called *indirect transition*.

As a semiconductor, silicon possesses a valence band maximum and a conduction band minimum which are separated by a energy gap of around 1.1 eV. These points do not occur at the same momentum value, therefore an additional phonon with the right difference momentum is required for the transition to take place. A direct transition without phonon absorption is possible, but at a higher energy. An illustration of the energy band diagram for silicon is provided in figure 1.4.

Additional energy levels close to the valence or conduction band can be created within the band gap. This is achieved by doping, i.e., adding trace amounts of select elements to the silicon lattice. These elements have either three valence electrons (p-doping, e.g. boron) or five valence electrons (n-doping, e.g. phosphorus), in contrast to silicon, which has four electrons covalently bound to other four neighbouring silicon atoms to form the lattice. The integration of the doping elements into this lattice leads to missing bonds in the case of p-dopants, or loosely bound electrons in the case of n-dopants, as shown in figure 1.5. The former gives raise to *acceptor levels* with an energy slightly higher than the edge of the valence band. The latter creates *donor levels* with energies slightly lower than edge of the conduction band.

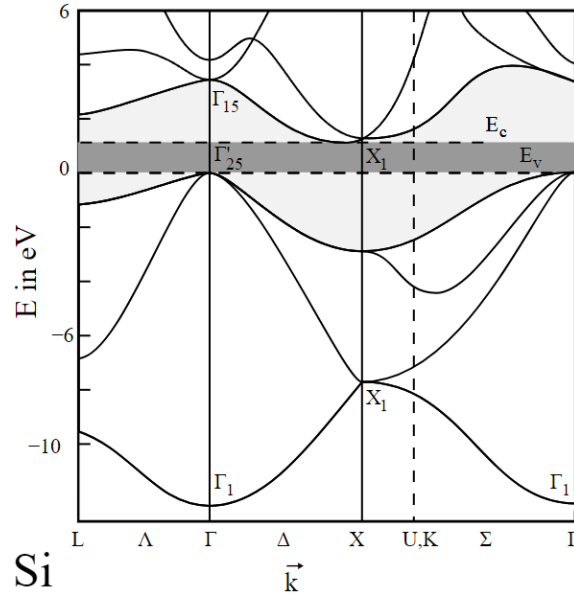


Figure 1.4.: Silicon band structure, showing the energy of a crystal electron in dependence on the momentum. The maximum of the valence band (at the Γ -point) and the minimum of the conduction band (left from the X -point) are separated by an 1.1eV energy gap (coloured in grey between the edge of the valence band E_V and the edge of the conduction band E_C). An indirect transition between the two bands is possible through additional phonon absorption (which increases the momentum of the electron up to the X -point). The direct transition at the Γ -point is also possible, but the energy difference is higher (around three times the band gap). From [8].

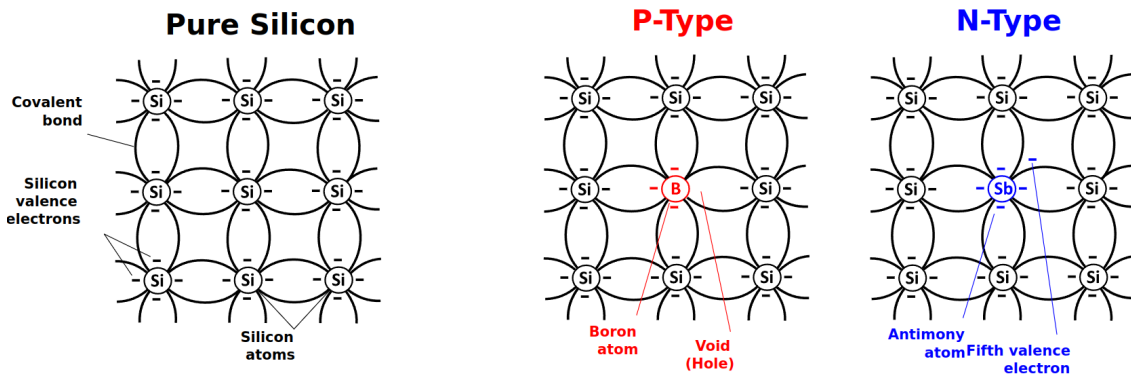


Figure 1.5.: Silicon lattice with and without impurities. From [9]

Electrons in the valence band can easily jump to acceptor states (the respective hole occupying the acceptor state then shifts to the valence band). Likewise, the transition of electrons from the donor states to the conduction band is easily triggered, leaving the donor state occupied by a hole. Thermal energies are sufficient to induce this kind of excitations, changing the electrical properties of the material.

In pure silicon, the signal of an ionising particle (i.e. produced electron-hole pairs) is around four orders of magnitude smaller than the noise (normal occupation of the conduction band by electrons of the valence band because of thermal excitation). In order to detect a particle at all, it is necessary to first reduce the noise. This can be accomplished by depleting the detector material from free charge carriers. [10]

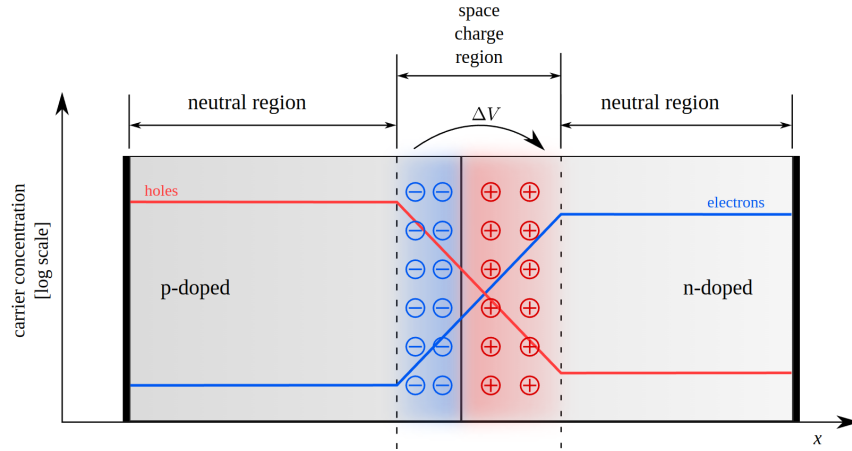


Figure 1.6.: Equilibrium state of a pn-junction (from [12]). An electric field arises between the charged regions. This electric field in the space charge region (also called depletion region) hinders further diffusion of free charge carriers. Almost no free charge carriers are present in the depletion region. The atoms within the depletion region are not neutral after diffusion since charge carriers left their position in the lattice and recombined, leaving fixed uncompensated charged regions behind (blue and red regions in the figure).

1.3.2. The pn-junction

One way to deplete the detector volume of free charge carriers is to use silicon with an n-type region and a p-type region, both of which are in contact. Since the p-type region is rich in holes but poor in electrons (and vice versa for the n-type region), holes diffuse from the p- to the n-region and electrons diffuse from the n- to the p-region. In the process, both charge carriers recombine. As a result, the two previously neutral regions are now electrically charged, since electrons or holes have diffused to the oppositely doped volume. As a consequence, an electric field is created. In equilibrium, this field opposes further diffusion of charge carriers, the diffusion and electrical potentials are equal in strength. A region depleted of free charge carriers is so created between the n- and p-doped materials: the depletion region. A depiction of the equilibrium state is provided in figure 1.6.

Within the depletion region there are almost no *majority charge carriers* (free electrons in the n-type region and holes in the p-type region). As a result, the noise is greatly reduced. Also, because of the electric field, the silicon volume now behaves as a diode. Electron-hole pairs created by an ionisation event will drift in opposite directions before recombination, and hence be separated, thanks to the built-in electric field. These charges move through the electric field to the electrodes and, in doing so, generate a signal which can be detected (Shockley-Ramo-Theorem, see [11]). Charges generated outside the depletion region can reach the electrodes and contribute to the signal, but this process is slow since it relies on the diffusion of the charges. Furthermore, charge carrier pairs may recombine during diffusion, resulting in a reduced collected charge.

The width of the depletion region can be increased by means of a reverse bias. This is achieved by connecting the positive pole of a power supply to the n-type region and the negative pole to the p-type region. Because of this new potential difference, holes are forced to drift further into the p-type region, widening the depletion region. The same holds true for the electrons, which diffuse into the n-region. A wider depletion region allows the collection of charge carriers over a greater volume in the detector.

More detailed information about silicon detectors can be found in [10].

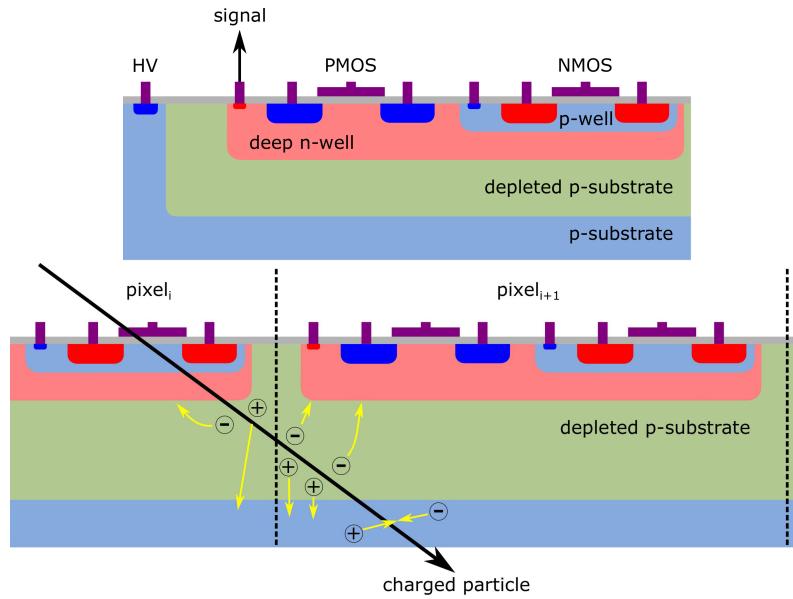


Figure 1.7.: Structure of a common CMOS pixel (top) and corresponding signal generation (bottom). The deep n-well contains and shields the integrated electronics. A voltage (HV) is applied between the front and either the front or the back plane of the chip to create the depletion zone. Electrons and holes are separated by the electric field within the depletion zone and collected by the electrodes in order to produce a signal. From [14].

1.3.3. CMOS detectors

CMOS detectors are a type of monolithic silicon detectors with integrated electronics. Monolithic detectors have the advantage of not needing a separate readout chip like hybrid silicon detectors, reducing the material needs and, with that, additional scattering of the beam. Moreover, since the electronics are embedded into the body of the silicon itself, no bonding with front-end electronics is required, which lowers cost of production. [1]

The use of high voltage CMOS chips (HV-CMOS) makes it possible to use reverse bias voltages of more than 100 V, increasing the width of the depletion region and the charge collected. For comparison, a substrate bias voltage of -6 V was chosen for the final ALPIDE chip (which uses the TowerJazz 180 nm CMOS imaging sensor process) for the ALICE experiment at the LHC. [13]

Thanks to the strong electric field achievable in HV-CMOS, fast charge collection is possible (taking only some nanoseconds), which has the additional benefit of avoiding charge trapping in radiation damaged sensors [1]. Fast separation of the charge carriers also limits the recombination of electron-hole-pairs following ionisation. The common structure of a CMOS pixel is depicted in figure 1.7.

Semiconductor devices based on the CMOS fabrication process are versatile and readily available in the market (mainly in the form of imaging devices for smartphones and cameras) for a reasonable price thanks to economy of scale. As a reference, the cost of a square meter of post-processed CMOS detector wafer lies between 80 000 to 90 000 €. For comparison, a square meter of a hybrid detector can be purchased for around 2 000 000 € [14]. The sensors can be found in a variety of sizes (usually around a couple of centimeters) from well known producers like Hamamatsu, Sony, Toshiba or Hynix [15].

TSI Semiconductors was chosen as the foundry for the HitPix detector chips. A production round of five wafers with 48 reticles has a cost point of around 150 000 €. The delivered wafers for HitPix 3 have shown a yield of 90%.

1.4. Radiation damage in silicon sensors

The next section follows [10].

1.4.1. Bulk damage

Interactions between the radiation and the silicon lattice lead to irreversible damage of the material caused by the recoil of the atoms following the interaction. This may lead to missing silicon atoms in the lattice (vacancies), silicon or impurity atoms displaced to the space between regular lattice points (interstitials), substitution of silicon atoms by impurities at the lattice points (impurity substitute) and other defects that may be also a combination of the effects above (di-vacancies, di-interstitials, etc...). Moreover, the induced defects can lead to the inactivation of the acceptor or donor centers, which is referred to as *acceptor* or *donor removal* (depending on the case) and lead to an altered doping behaviour of the silicon. The end result is a deformed lattice and a detector with altered leakage current, depletion voltage and charge collection efficiency.

The position of the defect energy levels within the band gap determines which property is altered. New energy levels close to the middle of the gap lead to larger leakage currents because of a detriment in the charge carrier lifetime. Donor levels near the conduction band and acceptor levels near the valence band induce changes in the depletion voltage because of alterations in the doping behaviour. Additionally, deep levels with long lifetimes generated as a consequence of radiation damage can trap charges from the conduction band causing a decrease in the amount of collected charge and thus a weaker signal. The charge trapping effects become significant at fluences higher than $1 \times 10^{15} \text{ cm}^{-2}$.

1.4.2. Surface damage

While electron-hole pairs are mobile within the detector bulk and can recombine easily, this is not the case for charge carrier pairs generated within insulator layers like the silicon oxide covering the bulk. After ionisation in the oxide, electrons can drift easily, before recombination, to the electrode thanks to their much higher mobility in comparison to holes. Holes, on the other hand, drift slowly and concentrate on the oxide-silicon interface, where the lattice mismatch and loose bounds favor the accumulation of holes.

One repercussion of this effect is a positive charge at the interface between oxide and silicon which alters the band structure and charge distribution along the interface. The now positively charged region may lead to the accumulation of electrons and negative traps from the bulk at the other side of the interface. In the end, this causes changes in the noise and cross-talk between nodes.

1.4.3. Annealing

The variations of the electrical properties of silicon are not stationary in general. In the case of bulk damage, the time dependence is due to the fact that interstitials and vacancies show a high mobility at temperatures over 150K and can therefore diffuse and combine/recombine. This effect is called *beneficial annealing* when advantageous and *reverse annealing* when detrimental, and shows a temperature dependence. In general, defect diffusion over time leads always to a reduction of the leakage current, first a reduction and then an increase in the depletion voltage (or vice versa) as well as to a decrease in hole trapping probability and increase in electron trapping probability.

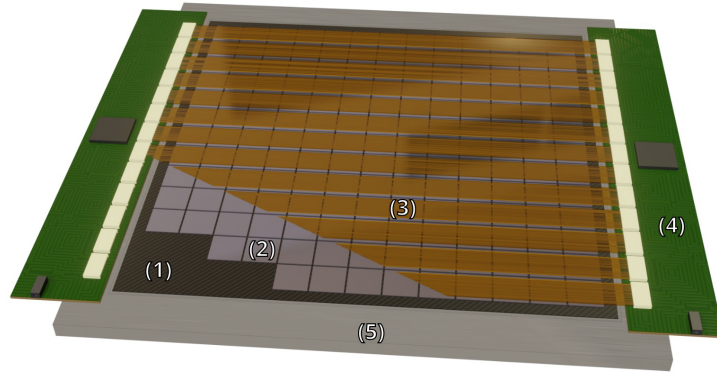


Figure 1.8.: Rendered image of the final detector array, comprising 13×13 detector chips (2) fixed over a carbon fiber plate (1) and bonded with flex cables (3). The electronic boards (4) are attached to a stabilizing frame (5). From [1]

1.5. Fluence and energy dose

In order to normalize the damage done by fluences of different types of radiations, the NIEL (non-ionizing energy loss) scaling hypothesis is usually applied:

$$\Phi_{\text{neq}}^{1\text{MeV}} = \alpha \cdot \Phi \quad (1.2)$$

The NIEL hypothesis connects the non-ionizing energy deposition of a fluence Φ of a given particle type and energy with the non-ionizing energy loss of a fluence $\Phi_{\text{neq}}^{1\text{MeV}}$ of 1 MeV neutrons. The latter variable is called *neutron equivalent* fluence, the proportionality parameter α is referred to as *hardness factor*, and depends on the particle type and energy.

The total ionizing dose (TID) dose transferred to a material by a beam of particles, on the other hand, can be calculated from the fluence as:

$$D = \Phi \cdot \frac{dE}{dx} \quad (1.3)$$

where $\frac{dE}{dx}$ is the *mass stopping power*, which corresponds to the energy loss from equation 1.1 normalized to the density of the material. The dose is expressed in Gray (Gy), which is equivalent to 1 J/kg.

1.6. The HitPix detector

With the requirements of section 1.2.1 in mind, a new silicon detector (**HitPix**) is being developed with the aim of replacing the current MWPC system at HIT. It is based on the HV-CMOS fabrication process and is being developed in cooperation with the Heidelberg Ion-Beam Therapy Centre. The final detector array is envisioned to have 13×13 chips (see figure 1.8).

Silicon pixelated detectors have some benefits over MWPCs. Pixel detectors allow higher resolutions and the reconstruction of two-dimensional profiles. Furthermore, they deliver faster signals (in the order of nanoseconds) since the charge collection in silicon detectors is not limited by the drift time of charge carriers in gas (in the order of microseconds). Silicon detectors are also better suited for future MRI-guided therapy systems, since they can be operated within magnetic fields and are resistant against acoustic vibrations (wire vibrations in MWPC lead to a loss in resolution). [1]

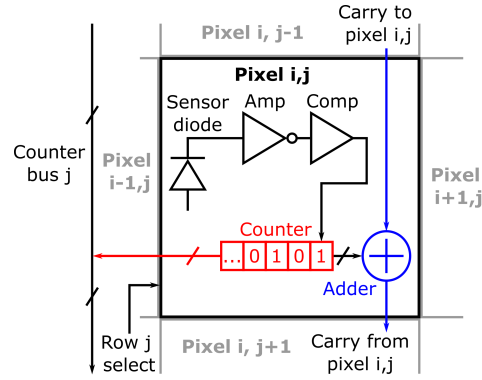


Figure 1.9.: Simplified schematics of the pixel integrated electronics. The signal is enhanced by an amplifier and sent to a comparator circuit, where a threshold is applied. Each hit is stored in the counter. From [1].

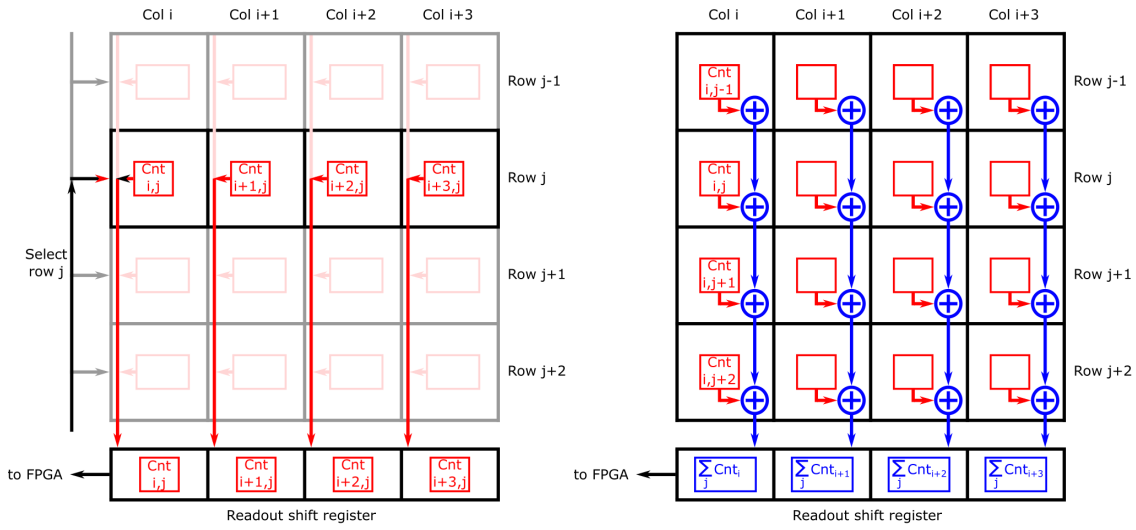


Figure 1.10.: Simplified illustration of the counters (left) and adders (right) readout. The hits stored in the counters can be read out using the counters bus (the information of each individual pixel is retrieved) or the adders bus (where only the sum gets propagated and read out). From [1].

There have been three revisions of the HitPix sensor design up to this date. While HitPix1 [16] had 24x24 pixels, the later generations have a matrix of 48x48 pixels with 200 μm pixel pitch (which corresponds to an active area of 9.6 mm). HitPix2 [17] has a pixel topology with three different deep n-wells per pixel (STD topology). The iteration of the design, HitPix3, is built in a topology with only one deep n-well which covers the whole pixel (see figure 2.1).

The readout of the pixel information are depicted in figures 1.9 and 1.10. There are two available readout modes available for the HitPix sensors: counter mode, in which the counts stored in each pixel are read out individually, and adders mode, in which only the sum of the hit counts in one row or column is propagated and read out. The decisive advantage of adders mode over the counters mode is the speed at which the stored data can be retrieved. Since in each readout cycle there are fewer data points to be read and sent (n in adders vs $n \times n$ in counters mode with n being the number of pixels in one row), the readout can be finished faster.

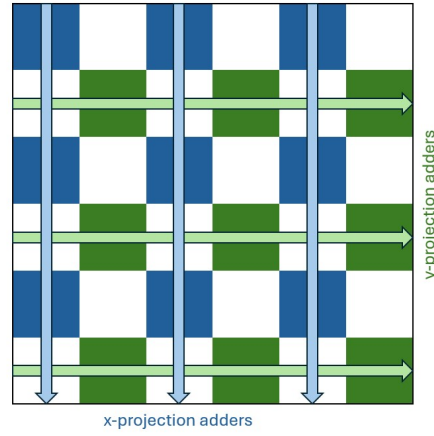


Figure 1.11.: Simplified representation of the adders projection in HitPix3. Only the coloured pixels in a row or column contribute to the adders' sum in the respective projection (x or y): The blue fields in each column and the green fields in one row are summed up to create the x and y projections. As a consequence, HitPix 3 delivers two projections with the data on 24 of the 48 total columns. In comparison, HitPix2 outputs 48 values, one for the sum of each column in the 48x48 array.

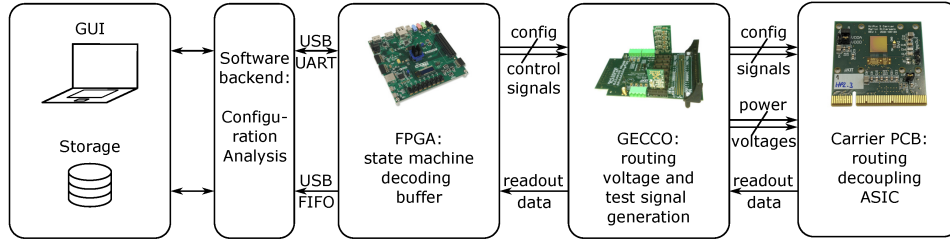


Figure 1.12.: Elements of the HitPix data acquisition system. From [1].

HitPix2 is able to read the adders projection in one dimension only, while the newest HitPix3 has a two dimensional adders projection in x - and y -direction, albeit with a loss of resolution (see figure 1.11). A typical frame size amounts to 30 μ s, which can be higher to compensate for lower intensities.

The data acquisition system comprises the elements illustrated in figure 1.12. The sensor is wire-bonded to a PCB, which is in turn connected via PCIe to a Generic Configuration and Control board (GECCO board) that also manages the voltages, test signals and links the detector with the FPGA board. The FPGA board operates the firmware of the sensor, which is uploaded to it by the interface implemented in the computer, from where the detector is operated by the user.[1]

2. Sentaurus TCAD simulations

In order to more accurately reproduce the propagation of charge carriers in the bulk of the HitPix detector, electric fields have been simulated for the available pixel topologies. These simulations can be used as an input for the Allpix² [18] simulation framework as a further refinement step. The fields have been generated for non-irradiated and irradiated sensors as well in order to investigate the effect of prolonged use of the detectors.

For this purpose, a commercial solution from Synopsys has been used. Synopsys Sentaurus Technology Computer Aided Design (TCAD) [19] is a comprehensive software suit used to simulate the properties and response of solid state devices. The simulations can model stationary states of the devices as well as non stationary processes which are driven by changes of the model parameters (like the bias voltage of the detector or the free charge carrier distribution). Sentaurus is also able to predict the behaviour of the device after an external event like, for example, a traversing particle interacting with the detector.

The simulation workflow (within the scope of this work) starts with the creation of a geometry model of the device using the *Sentaurus Structure Editor* module. This model is the input for the device simulation using the *Sentaurus Device* module. The simulation parameters have to be tailored to the conditions and characteristics of the HitPix detector, which are set, viewed and controlled by a command file and the *Sentaurus Workbench* module. The workbench is used to plan different scenarios by inserting the corresponding parameters into a tabular form following a tree pattern. The software then creates a separate command file for each scenario and runs the simulation. Detailed information about the simulation settings configured in the command file of *Sentaurus Device* can be found in the provided manual ([20]).

In the following sections, the application of this workflow for the HitPix detector will be presented.

2.1. Geometry models

The workflow starts with the design of a geometry model for each pixel topology. It is sufficient to concentrate on the volume of a single pixel, since the electric field within the pixel matrix is periodic. With that in mind, periodic boundary conditions on each contact surface of the simulation volume with other neighbouring pixels are applied to ensure the continuity and periodicity of the solution.

As described in the last chapter, the HitPix sensor family has been conceived and designed with two different pixel topologies (STD and ISO, see figure 2.1). The pixel pitch is in all cases $200 \times 200 \mu\text{m}^2$.

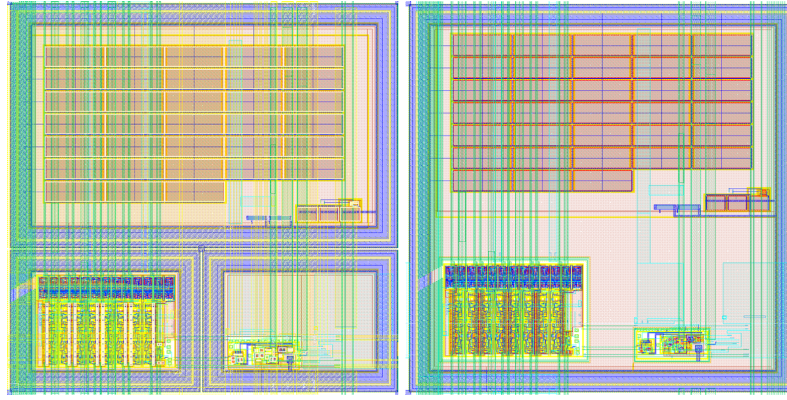


Figure 2.1.: Pixel topologies of the HitPix detector family. The STD topology (left picture) consists of three regions separated by highly doped p-guards. The upper pixel part is sensitive, while the two lower ones contain the integrated electronics (counter and adder on the bottom left and comparator and amplifier on the bottom right). The ISO topology (right picture) has only one sensitive region which extends to the whole pixel. Modified from [17]

All topologies use highly p-doped rings (p-guards) which are present at the contact region between pixel cells (blue regions in figure 2.1). These highly doped volumes at the boundaries have shown to be problematic in simulation, hindering convergence of the solution if periodic boundary conditions were enforced. In order to overcome this difficulty, the geometry model was centered at the corner point between four pixels, limiting the presence of highly doped regions at the boundaries. The convergence behaviour improved immensely after this modification was applied.

The author thanks Ekaterina Trifonova for the information about the pixel geometries, inner structure and material characteristics.

2.1.1. ISO topology

The ISO topology was implemented with the dimensions and geometry depicted in figures A.1 and A.3 (appendix). The doping profile of the bulk is constant throughout the whole silicon bulk with a boron concentration of $N_A = 4 \times 10^{13} \text{ cm}^{-3}$ for a material resistivity of 370 Ohm cm. The doping profiles of the deep n-wells and the p-guards are Gaussian in z -direction, with a peak concentration at the bulk surface. The phosphorus peak concentration of the n-well was set to $N_D = 1 \times 10^{16} \text{ cm}^{-3}$ with a junction line (point at which the effective doping equals that of the bulk) at $8 \mu\text{m}$ depth. In the case of the p-guards, the boron peak concentration was set to $N_A = 1 \times 10^{17} \text{ cm}^{-3}$ with a junction line at $1.7 \mu\text{m}$ depth. A lateral diffusion was applied to both profiles so that the doping concentration does not change abruptly at the lateral boundary (in x - and y -direction) of the deep n-wells.

Once the geometry and the doping profiles are defined, the *mesh* can be generated. The mesh is comprised by a point grid representing the points at which the simulation variables are computed. A finer mesh leads to a higher spatial resolution of the simulation variables, at the cost of computing time. A too coarse mesh, however, leads to problems in the convergence of the simulation. A balance between computing time and result accuracy has to be found, therefore different meshing regions and criteria were defined in the Sentaurus Structure Editor depending on the expected amount of change of the simulation variables. For example: the electric potential is expected to vary strongly near the n-wells but remain more or less constant deep within the bulk. Hence, a finer mesh should be chosen near the detector surface and the n-wells, while a coarser mesh can be used for the rest of the bulk. The mesh for the ISO topology is depicted in figure A.1 (in the appendix).

2.1.2. STD topology

The doping profiles of the STD topology are analogous to those of the ISO topology (as well as the resistivity). The geometry features three deep n-wells instead of one. Only the bigger well is sensitive. The bias voltage is applied to the contacts over all wells. The back contact is the same as in the ISO topology. An analogous meshing strategy was applied. The schematics of the STD topology as simulated are provided in figure A.2 (in the appendix).

2.2. Sentaurus Device module

Once the mesh and geometrical models are finished, they are used as an input for the *Sentaurus Device* module. The simulation is configured via a command file with different sections, which are going to be briefly described next. Detailed information about the models within this section can be found in [20]. The following paragraphs are based on the information therein.

2.2.1. File

The **File** section defines standard input and output files:

```
File {
  * Input Files
  Grid      = "std_corners.tdr"
  Parameter = "@parameter@"
  * Output Files
  Current   = "n@node@_std_current"
  Plot      = "n@node@_std_plot"
  Output    = "n@node@_std_output"
  Parameter = "n@node@_sdevice.par"
}
```

The **Grid** statement points to the geometry model with mesh created in the previous step. The **Parameter** statement is used to alter standard parameter values (physical constants, material specific values, etc.) and it points, in this case, to a file specified in the *Sentaurus Workbench* graphical interface (which is depicted in figure A.4) via the command `@parameter@`. The way in which the parameters are changed (formula, input from the workbench's cells, ...) is configured in that file. The statements **Current**, **Plot**, **Output** and **Parameter** set the names of the output files for the current step of the simulation, the simulation results, the log and the corresponding preprocessed parameter file used for that node (i.e. the concrete values obtained after applying the formulas or inputs specified in the input parameter file), respectively. The command `@node@` adds the number of the node corresponding to the simulation which is running (last cell of the tree, see figure A.4) to the file name.

2.2.2. Electrodes

The *Electrode* section sets the initial state of the electrode sets in the simulation:

```
Electrode {
  { Name="front"      Voltage=0 }
  { Name="back"       Voltage=0 }
}
```

In this work, two sets of electrodes are defined in both topologies: back and front. The front electrode set comprises all the grey pads in figures A.3 and A.2 and are treated as a single electrode in the command file, meaning that all share the same state (voltage, in this case) during the simulation. Same also applies for the back electrodes, which are the same in both topologies and analogous to the front electrodes in the ISO topology (see figure A.3).

2.2.3. Physical models

The *Physics* section sets the models which are going to be used during the simulation:

```
Physics {
  Temperature = @Temperature@
  Fermi
  Mobility(
    DopingDep
    eHighFieldSaturation hHighFieldSaturation
    CarrierCarrierScattering (ConwellWeisskopf)
  )
  Recombination(
    SRH(
      DopingDependence TempDependence
      ElectricField(
        Lifetime=Hurkx
        DensityCorrection=none
      )
    )
    Auger
    eAvalanche (vanOverstraeten Eparallel)
    hAvalanche (vanOverstraeten Eparallel)
  )
  EffectiveIntrinsicDensity(Slotboom)
}
```

The **Temperature** statement sets the temperature corresponding to the values given in the workbench's interface. The next statements activate Fermi statistics and configure the mobility models for the simulation, taking into account the mobility degradation as a consequence of scattering with the doping centers (according to the Masetti model [21]), carrier carrier scattering (based in [22] and [23] as well as the Conwell-Weisskopf theory [24]) and mobility (drift velocity) saturation for electrons and holes (following the Canali model [25]).

Furthermore, recombination of the charge carriers in the bulk is considered via the Shockley-Read-Hall (SRH, implemented in the form stated in [20]) and the Auger mechanisms. The SRH model is set to scale with the doping concentrations and the temperature. The associated lifetimes will be tuned to the HitPix detectors later using leakage current measurements. Field enhancement is also activated for the SRH model, which lowers the SRH lifetimes wherever a strong electric field is present. This is done according to the Hurkx model [26].

Avalanche generation is enabled and follows the van Overstraeten - de Man model (based in [27] and [28]) with the parallel component of the electric field as the driving force. Finally, doping-induced bandgap narrowing is taken into consideration via the Slotboom model (based in [29], [30], [31] and [32]).

The coupled defect level recombination (CDL) option (which can also be enabled in this section) activates the coupling between trap levels, allowing not only transitions of charge carriers between defect levels and bands, but also between defect levels themselves. It is intentionally deactivated for simulations in which the radiation damage is not considered since it was shown to cause high leakage currents. CDL is therefore only active if radiation damage models are active too. This behaviour was also observed in [33].

2.2.4. Plots

The Plot section contains the variables which should be provided once the simulation has finished. Relevant for this work are:

```
Plot {
  Doping DonorConcentration AcceptorConcentration
  eDensity hDensity SpaceCharge
  TotalCurrentDensity TotalCurrentDensity/Vector
  Potential ElectricField ElectricField/Vector
  eInterfaceTrappedCharge hInterfaceTrappedCharge
  TotalTrapConcentration eTrappedCharge hTrappedCharge
  SRHRecombination AugerRecombination SurfaceRecombination
  TotalRecombination CDL CDL1 CDL2 CDL3
  eCurrentDensity eCurrentDensity/Vector
  hCurrentDensity hCurrentDensity/Vector
  eAvalanche hAvalanche
  * (...)
}
```

2.2.5. Math

The *Math* section controls some of the computational parameters of the iterative solution buildup process:

```
Math {
  NumberOfThreads=32
  *-- Numeric/Solver Controls --*
  Method=PARDISO Extrapolate Derivatives
  Iterations=8 NotDamped=50 RelErrControl Digits=7
  Transient=BE Wallclock
  *-- Periodic boundary conditions --*
  PeriodicBC(
    (Direction=0 Coordinates=(-100.0 100.0))
    (Direction=1 Coordinates=(-100.0 100.0))
  )
}
```

Relevant for this work is the definition of periodic boundary conditions at the edges of the simulation volume (=1 pixel), so that the produced electric fields can be mapped onto the 48x48 pixel array, yielding a continuous field over the whole sensor volume.

2.2.6. Solve

Finally, the **Solve** section describes the way in which the final solution is going to be computed:

```

Solve {
*- Buildup of initial solution:
  Coupled(Iterations=100){ Poisson }
  Coupled(Iterations=100){ Poisson Electron Hole }
*- Iteration towards the final solution
  Quasistationary(
    InitialStep=0.01 MinStep=1e-15 MaxStep=0.2
    Increment = 2 Decrement = 3
    Goal{ Name="front" Voltage= 1.8 }
  ){ Coupled( Iterations=5 ){ Poisson Electron Hole } }
  Quasistationary(
    InitialStep=0.01 MinStep=1e-15 MaxStep=0.2
    Increment = 2 Decrement = 3
    Goal{ Name="back" Voltage= -100.0 }
  ){ Coupled( Iterations=5 ){ Poisson Electron Hole } }
}

```

The first two **Coupled** commands create an initial solution by first solving the Poisson equation:

$$\nabla \cdot (\epsilon \nabla \phi - \vec{P}) = -q(p - n + N_D - N_A) - \rho_{\text{trap}} \quad (2.1)$$

Here ϵ represents the electrical permittivity, \vec{P} the polarisation of the material, q the elementary charge, n/p the electron/hole densities N_D/N_A the concentration of ionized donors/acceptors and ρ the charge density of traps and fixed charges.

The electron/hole densities for Fermi statistics are defined as:

$$n = N_C F_{1/2} \left(\frac{E_{F,n} - E_C}{kT} \right), \text{ with } E_{F,n} = -q\Phi_n \quad (2.2)$$

$$p = N_V F_{1/2} \left(\frac{E_V - E_{F,p}}{kT} \right), \text{ with } E_{F,p} = -q\Phi_p \quad (2.3)$$

where N_C and N_V are the effective density of states, $F_{1/2}$ is the Fermi integral of order 1/2, $\Phi_{n/p}$ are the quasi-Fermi potentials for electrons and holes, and $E_{C/V}$ are the conduction and valence band edges. The latter can be computed using:

$$E_C = -\chi - q(\phi - \phi_{\text{ref}}) \quad (2.4)$$

$$E_V = E_C - E_{g,\text{eff}} \quad (2.5)$$

with the electrostatic potential ϕ , the electron affinity χ and a constant reference potential ϕ_{ref} . According to the manual, this reference potential is set to the intrinsic Fermi level of silicon if there is silicon in any simulated semiconductor structure [20].

From there, and based on that solution, the coupled system of Poisson and continuity equations for electrons and holes is solved in order to get the electrostatic potential and the electron/hole densities. The continuity equations are given by:

$$\nabla \cdot \vec{J}_n = q(R_{\text{net},n} - G_{\text{net},n}) + q \frac{\partial p}{\partial t} \quad (2.6)$$

$$-\nabla \cdot \vec{J}_p = q(R_{\text{net},p} - G_{\text{net},p}) + q \frac{\partial p}{\partial t} \quad (2.7)$$

The variables R_i and G_i denote the electron or hole net recombination rates and generation rates and \vec{J}_i represents the electron or hole current densities. Solving the Poisson equation first before the coupled system works better than solving the coupled equations together at the beginning.

Taking this solution as a starting point, the electrode voltages are changed slowly via the **Quasistationary** steps and a new solution is computed. This process continues until the final state is reached (if the solution process converges). The **Step** statements control how fast the procedure is carried out. The **Increment** and **Decrement** commands determine how much higher or lower the step becomes after a successful or failed iteration step, respectively.

After the last iteration is complete, the plots are saved to a file which can be interactively viewed using the *Sentaurus Visual* module.

2.2.7. Radiation damage

As described in the introductory section, prolonged irradiation induces defects in the sensor. Lattice defects behave in many cases like additional energy levels. Therefore, radiation damage models can be built around additional acceptor and donor levels, whose characteristics can be optimized to fit the experimental evidence for a given device.

Two models will be used in this work to reproduce bulk and surface damage in the simulations of the HitPix detectors and, by doing so, attempt to evaluate their effects after a fluence of $1 \times 10^{15} \text{ n}_{\text{eq}} \text{ cm}^{-2}$.

When comparing simulations and experiments in the following sections, one has to consider that the radiation model is not completely tuned to the HitPix sensors and, therefore, the results are to be understood as rough estimates of the expected behaviour of the sensors.

2.2.7.1. Bulk damage

The bulk radiation damage is implemented by making use of the model developed in [33] (Eber Model), which is available for $T = 253 \text{ K}$ and $T = 273 \text{ K}$ as well as for proton and neutron irradiation. It features two discrete energy levels in the form of a deep acceptor and a deep donor to reproduce the bulk traps.

The parameters for $T = 273 \text{ K}$ (see Table 2.1) and a proton fluence of $1 \times 10^{15} \text{ n}_{\text{eq}} \text{ cm}^{-2}$ are used. In this case, CDL is activated to allow the coupling between trap levels as commented in section 2.2.3. Lastly, the command **Add2TotalDoping** integrates the traps into the doping profile, including them into the acceptors or donors (according to the sign of the trap). This changes their concentration and the total doping concentration and is relevant for doping-dependent calculations in some models (e.g. mobility or lifetime).

Table 2.1.: Bulk radiation damage model for T=273K. Fluence Φ in n_{eq}/cm^{-2} . From [33].

Type	Energy [eV]	Concentration [cm^{-3}]	σ_e [cm^2]	σ_h [cm^2]
Deep donor	$E_V + 0.48$	$-3.96 \cdot 10^{14} + 5.598 \cdot \Phi$	$0.954 \cdot 10^{-14}$	$1.65 \cdot 10^{-14}$
Deep acceptor	$E_C - 0.525$	$0.65 \cdot 10^{14} + 1.189 \cdot \Phi$	$1.65 \cdot 10^{-14}$	$0.954 \cdot 10^{-14}$

```

*— Eber model for bulk radiation damage (proton irradiation) —*

#if @fluence@ > 0
  Physics ( material = "Silicon" ){
    Recombination( CDL )
    Traps(
      ( Donor Level fromValBand Add2TotalDoping
        Conc=!(puts [expr @fluence@*5.598-3.96e14])!
        EnergyMid=0.48
        eXsection=0.954e-14 hXsection=1.65e-14 )
      ( Acceptor Level fromCondBand Add2TotalDoping
        Conc=!(puts [expr @fluence@*1.189+0.65e14])!
        EnergyMid=0.525
        eXsection=1.65e-14 hXsection=0.954e-14 )
    )
  }
#endif

```

2.2.7.2. Surface damage model

For the simulation of surface damage at the interface between the silicon oxide layers and the bulk, the Perugia 2019 Surface Damage Model has been chosen (see [34]). It features an additional acceptor band right below the conduction band and an additional donor band right above the valence band. Furthermore, the fixed charge at the interface is also considered.

The Perugia Model was tuned to gated diodes, MOS capacitors and MOSFETs from Fondazione Bruno Kessler, Hamamatsu Photonics and Infineon Technologies to extract dose-dependent model parameters for each of them individually. A wide range of techniques was applied to measure the necessary parameters depending on the type of the device under test. For example, the flat-band voltage in MOS capacitors experiences a shift towards more negative values due to radiation damage which is linked with a rise in the fixed oxide charge at the silicon-oxide/Si interface. Additionally, traps at the interface change the capacitance-voltage characteristics of the device. On gated diodes, the surface generation velocity and the interface trap states density are proportional to each other and can be studied by means of current-voltage measurements. The changes in the flat-band voltage of these devices are similar to those described above. [34]

Determining a dose from the fluence applied to the detector is not a straightforward matter considering that the detectors at HIT are expected to be exposed to particles of different energies (and to different types of ions). As explained in section 1.5, each particle type and energy is linked to a specific ionizing dose according to the Bethe equation. Therefore, beams with different settings contribute differently to the TID depending on those settings. Since the total proton fluence for each type of beam over the years is unknown, an exact dose calculation is not possible. An estimate is to be made at this point.

Table 2.2.: Perugia 2019 Surface Damage Model at a dose of 84 Mrad. The values of Q_{ox} , Nit_{acc} and Nit_{don} are mean values of the parameters provided in [34] for different detector types and manufacturers (top table). The acceptor and donor energies are not discrete values but bands below and above the conduction and valence bands (bottom table). The parameters $\sigma_{e/h}$ represent the cross section for electrons and holes.

Detector	Q_{ox} [10^{11}cm^{-2}]	Nit_{acc} [10^{11}cm^{-2}]	Nit_{don} [10^{11}cm^{-2}]
HPK	7.14	13.02	23.57
IFX 8"	17.57	17.33	16.72
IFX 6"	12.35	18.66	21.67
FBK	12.15	32.53	15.14
Average	12.30	20.38	19.27

Type	Energy [eV]	σ_e [cm^2]	σ_h [cm^2]
Deep acceptor	$E_C \geq E \geq E_C - 0.56$	10^{-16}	10^{-15}
Deep donor	$E_V + 0.6 \geq E \geq E_V$	10^{-15}	10^{-16}

The fluence used to estimate the radiation damage in this work is set to $\Phi = 1 \times 10^{15} \text{ cm}^{-2}$. Considering the definitions of the neutron equivalent fluence in section 1.5, equation 1.1, the hardness factors for protons reported in [35] and the proton energies output by the accelerator at HIT, the worst case scenario (for proton beams only) would correspond to the constant use of a beam consisting on 48.12 MeV protons. The associated stopping power of silicon can be calculated from equation 1.1 and the silicon density, resulting in $9.93 \text{ MeV cm}^2/\text{g}$. According to [35], the hardness factor of protons with that energy is around $\alpha = 1.9$. Thus, the total ionizing dose (TID) for this scenario amounts to:

$$\text{TID} = \frac{\Phi_{\text{neq}}^{1\text{MeV}}}{\alpha} \cdot \frac{dE}{dx} = 0.84 \text{ MGy} = 84 \text{ Mrad} \quad (2.8)$$

The Perugia model is dependent on the fixed oxide charge at the interface (Q_{ox}) as well as on the additional concentrations of acceptors (Nit_{acc}) and donors (Nit_{don}) at the interface. For the sake of generality, the mean values of the model parameters for the different devices studied in the project were used for the TCAD simulation of the HitPix structures (for the dose calculated above). The parameters are summarized in table 2.2.

Sentaurus takes the spectral density of the trap levels as input for the statement **Conc** in the case of an uniform trap definition (like the bands in Table 2.2). The spectral density is easily derived from the concentration. It holds

$$N = \int_0^\infty D(E) dE$$

with the trap concentration N and the trap spectral density $D(E)$. Since the bands are uniform, there is no energy dependency in D and one can assume:

$$N = D \cdot \Delta E$$

In this case, ΔE is the width of the band.

```

*— Perugia 2019 Model for surface radiation damage —*

#if ( @Qox@ > 0 || @Nit_acc@ > 0 || @Nit_don@ > 0 )
  Physics ( MaterialInterface = "Silicon/SiO2" ){
    Recombination( CDL )
    Traps(
      #if @Qox@ > 0 ( FixedCharge Conc=@Qox@ ) #endif
      #if @Nit_acc@ > 0
        ( Acceptor Uniform fromCondBand Add2TotalDoping
          Conc=!(puts [expr @Nit_acc@/(0.56)])!
          EnergyMid=0.28 EnergySig=0.56
          eXsection=1e-16 hXsection=1e-15 )
        #endif
      #if @Nit_don@ > 0
        ( Donor Uniform fromValBand Add2TotalDoping
          Conc=!(puts [expr @Nit_don@/(0.6)])!
          EnergyMid=0.30 EnergySig=0.60
          eXsection=1e-15 hXsection=1e-16 )
        #endif
      )
    }
  #endif

```

2.3. Charge carrier lifetime in the SRH Model

Electron-hole pairs generated within the silicon bulk may appear and recombine through different channels. Particularly relevant is the Shockley-Read-Hall model [36][37], which is an inter-band recombination mechanism through which charge carriers annihilate thanks to defect levels within the band gap. The electrons and holes have a lifetime associated with the recombination mechanism, which determines some of the electrical properties of the detector, the leakage current among them.

The SRH lifetime is mathematically modelled in Allpix Squared as follows [38]:

$$\tau(N, T) = \tau_0 \cdot \frac{1}{1 + \frac{N}{N_{\text{ref}}}} \cdot \left(\frac{T_{\text{ref}}}{T} \right)^{3/2} \quad (2.9)$$

The equation above scales a reference lifetime τ_0 first with a doping dependent and then with temperature dependent term. There is also a dependency on the strength of the electric field in Sentaurus TCAD (see section 2.2.3), which is omitted for the simulations with Allpix Squared. The equation and parameters in equation 2.9 are defined consistently in Sentaurus as well as in Allpix Squared. The equation holds for electrons and holes separately.

Table 2.3.: Simulation parameters (reference doping, reference temperature and reference lifetime) implemented in Allpix Squared and Sentaurus TCAD. Except for the reference lifetime τ_0 , the remaining parameters are the default values in Allpix Squared and are taken from [38]. The reference lifetimes are scaled by a factor of 0.025 with respect to the default values, as explained in the text.

Parameters	N_{ref}	T_{ref}	τ_0
Electrons	$1 \times 10^{16} \text{ cm}^{-3}$	300 K	$0.025 \cdot 1 \times 10^{-5} \text{ s}$
Holes	$7.1 \times 10^{15} \text{ cm}^{-3}$	300 K	$0.025 \cdot 4 \times 10^{-4} \text{ s}$

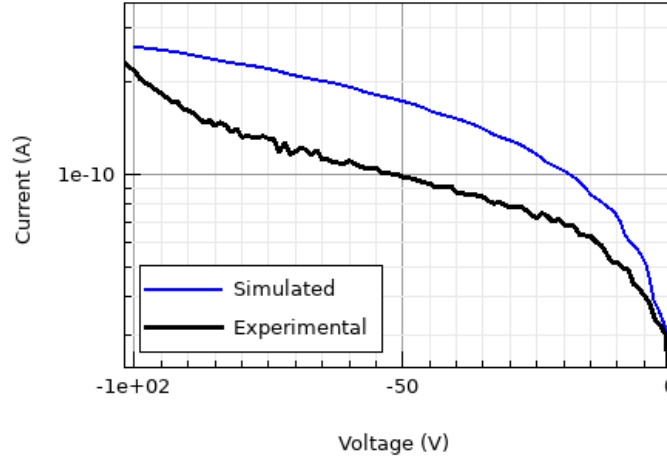


Figure 2.2.: Simulation results for the tuning of the SRH lifetime to experimental data taken from a HitPix 2 STD 1×1 array. The simulated data corresponds to the leakage current of one single pixel in STD topology, thus the experimental curve for the whole 48×48 pixel array had to be scaled with a factor $1/(48 \cdot 48)$ to reflect the measurement data.

Since the silicon delivered by different manufacturers is unique in composition and quality, each detector has to be characterised to determine the individual material properties of the detector under investigation. In this case, the SRH lifetime has to be ascertained. Considering that the charge carrier generation and recombination rates influences the leakage current, the parameters in equation 2.9 can be estimated by comparing the simulated and experimental IV-curves. To that end, the measured values of a HitPix 2 detector chip (with STD topology) were used and the parameter τ_0 was varied until the simulated and experimental curves approximately match. Since the reference lifetimes τ_0 are different for holes and electrons, both were scaled with the same factor using the default values stated in [38] as a starting point. The rest of the values were fixed and are provided in table 2.3 for reference. A temperature of 293 K was assumed during this simulation.

The results of this procedure can be seen in figure 2.2: The default lifetimes have to be scaled with a factor of 0.025 to match the experimental measurements within a factor of two. This is sufficient, considering the fact that a similar variability is observed in the leakage current curves from sensors of the same type and wafer, as seen in [39]. It should be noted that a match for a bias voltage of 100V was aimed for, as it is in this regime where the simulations are going to be performed. These estimates for the SRH lifetimes are going to be used for the rest of the simulations in this work.

2.4. Electric fields

With the knowledge extracted from the previous section and after ensuring that the computations would converge under the given configurations, the simulation of the electric fields for both HitPix topologies was performed using the geometries presented in the appendix.

2.4.1. ISO topology

The produced electric fields for the ISO topology are presented in figure 2.3. There is a noticeable difference between the irradiated against the non irradiated sensors regarding the depth of the depletion zone.

The decrease in field depth for the irradiated sensors is explainable considering the definition of the defect levels within the bulk (see section 2.2.7.1). In Sentaurus, acceptor levels are uncharged when occupied and negatively charged otherwise. Analogously, donor levels are positively charged when occupied. Hence, mainly holes are trapped within the p-doped bulk by occupying the donor levels. Near highly n-doped regions like the implants, the net effect is the opposite: the acceptor levels show a higher occupancy and, thus, electrons are trapped. The net effect is a change in the doping behaviour and, in this case, to a lower width of the depletion area. The trap occupancy is also temperature dependent, this explains why the field depth also changes for different temperatures in irradiated sensors. A graph depicting the electric field strength at a given depth is provided as well in figure 2.4 for illustration. The linearity of the electric field still seems to be a good approximation, even for irradiated sensors.

2.4.2. STD topology

For completeness, the fields for the STD topology are presented in figures 2.3 and 2.5. The depiction is not as simple as for the ISO topology because of the asymmetry of the topology. In order to convey the most information possible, the plane for the visualisation of the cross section is chosen so that the sensitive (biggest) n-well and the lower left n-well are crossed by it (cf. left picture in figure 2.1). The results look very similar to those for the ISO topology and follow the same patterns.

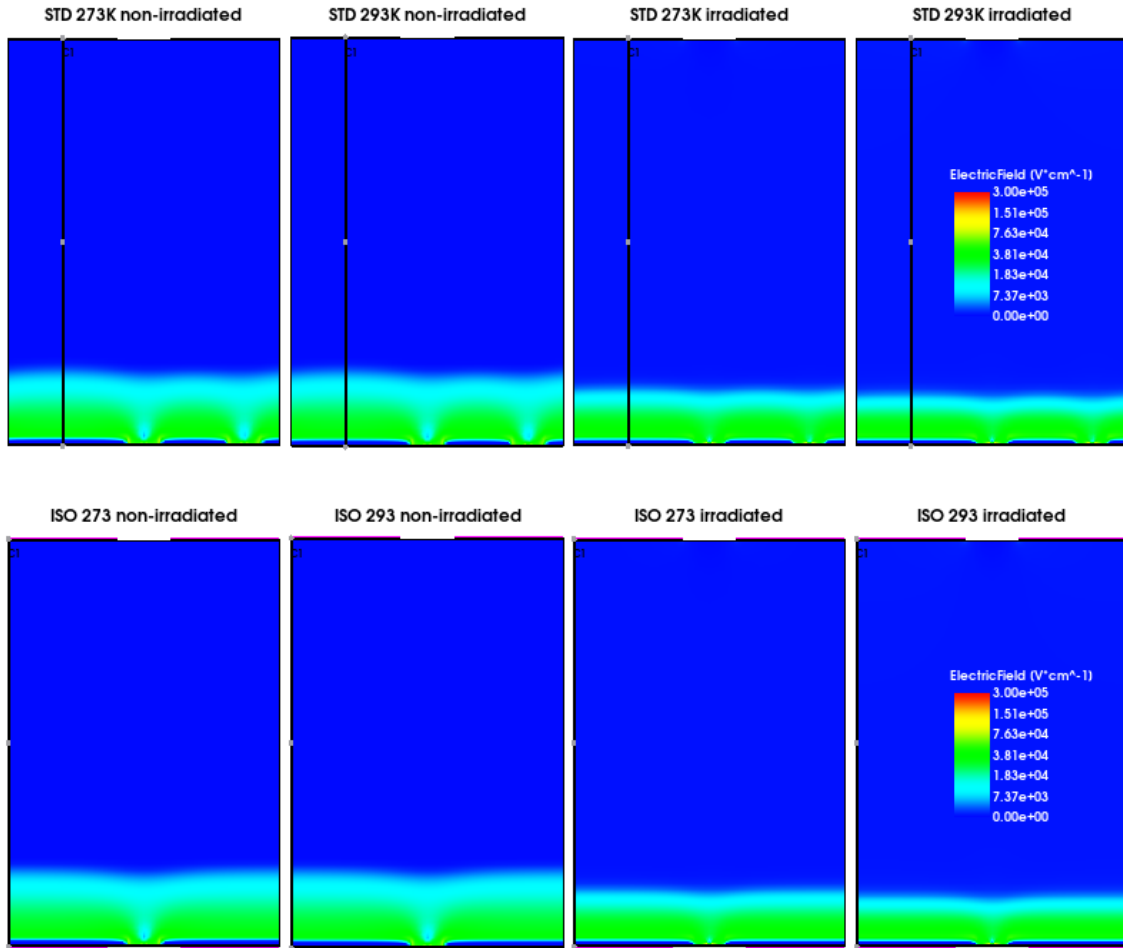


Figure 2.3.: Electric field strength with ISO (top) and STD (bottom) topology for 273 K and 293 K and two irradiation states at a reverse bias voltage of -100 V. The color gradient uses an *asinh* scale for better visibility, and it is common to all. The grey dots on the center left (top row) and left margin (bottom row) of the plots represent the line at which the electric field z-component is read in figure 2.4.

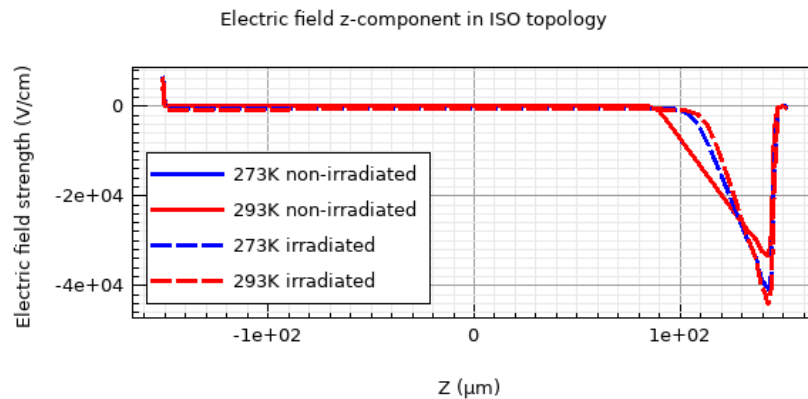


Figure 2.4.: Depth dependency of the z -component of the electric field for the ISO topology at a reverse bias voltage of -100 V. The values are taken along the grey dots in figure 2.3. The curves for the non-irradiated sensors overlap and are therefore not visible at the same time.

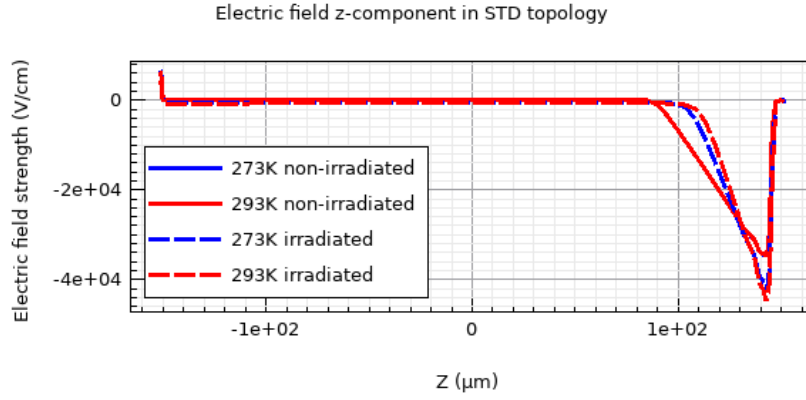


Figure 2.5.: Depth dependency of the z -component of the electric field for the STD topology at a reverse bias voltage of -100 V. The values are taken along the grey dots in figure 2.3. The curves for the non-irradiated sensors overlap and are therefore not visible at the same time.

2.5. Leakage current

Irradiation of the detector leads to further damage of the silicon lattice and, hence, to additional defects which can lead to an increase of the leakage current, as discussed in section 1.4. This can also be incorporated in the TCAD simulations. The leakage current curves for the ISO topology sensor under different conditions are provided in figure 2.6. The curves for the ISO topology are practically identical to those of the STD topology.

The leakage current breakdown of the sensor as seen in figure 2.2 (which starts at around 100 V) could not be reproduced in the TCAD simulations at the simulated voltages and could not be seen in the curves for the irradiated sensors either. Reasons for that could be the necessity for a more detailed and experimentally-guided modelling of the avalanche generation processes or the presence of impurities in the real materials (which are not included into the simulations). Imperfections in the lithographic production could also lead to a earlier onset of the breakdown.

The simulated leakage current curves for the ISO irradiated sensors are within approximately one order of magnitude from the values reported in [16] (after adequate scaling from the 48×48 matrix to one pixel and before breakdown) for both simulated temperatures. These simulated curves nevertheless show higher currents than measured, although the fluence under which the measurements were performed in [16] is slightly higher than assumed in simulation and, therefore, it is to be expected that the leakage current be also slightly higher.

In an other study ([39]), the current-voltage-curves (IV-curves) of three non-irradiated and four irradiated HitPix 3 ISO sensors (all different) were measured. These measurements yielded average leakage current values of roughly 3×10^{-12} A and 1×10^{-7} A for non-irradiated and irradiated HitPix 3 ISO sensors, respectively, in both cases at 293 K, $V_{\text{bias}} = -100$ V and after down-scaling to one pixel. The former result does not align with the leakage currents shown in figure 2.6. Nevertheless, the simulated IV-curve at 293 K was tuned to a measured HitPix 2 IV-curve (as discussed in section 2.3), so this discrepancy could be attributed to variance within the sensor materials. For irradiated sensors, on the other hand, the measurement in [39] is in better agreement with the simulations (which yield a value of roughly 4×10^{-7} A at $V_{\text{bias}} = -100$ V).

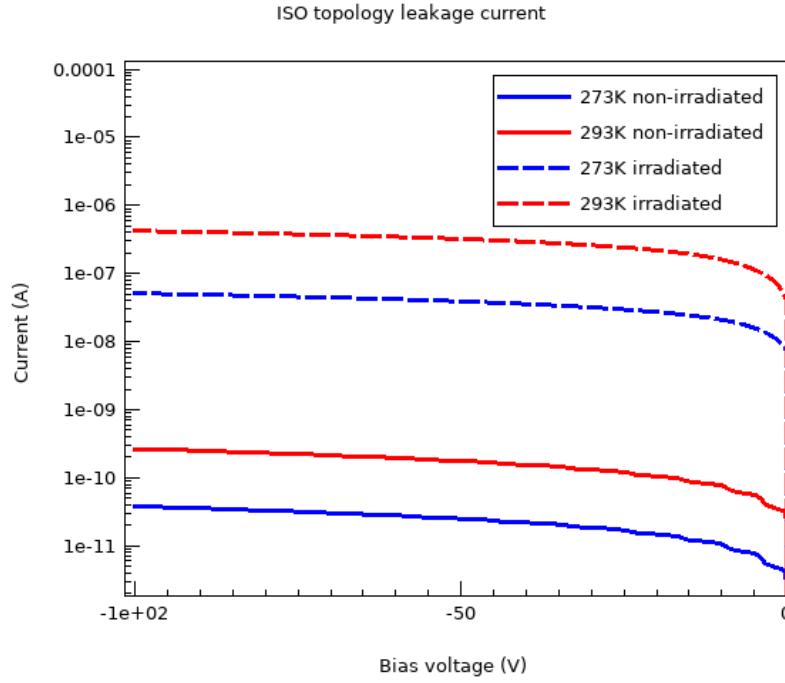


Figure 2.6.: Simulated leakage current for ISO topology pixels as a function of the bias voltage before and after irradiation. The curves for the ISO topology are practically identical to those of the STD topology.

2.6. Conclusions

The two topologies of the HitPix detector family were successfully implemented in the Sentauros TCAD simulation software including models for the surface and bulk damage induced by a fluence of $\Phi = 1 \times 10^{15} \text{ cm}^{-2}$.

The expected charge carrier lifetime was estimated by comparing the simulation results for the leakage current in STD topology pixels with experimental data taken from a HitPix 2 chip (scaled accordingly to the size of one pixel). Electrons and holes are expected to propagate for around $\tau_0 = 250 \text{ ns}$ and $\tau_0 = 10\,000 \text{ ns}$ respectively (before doping and temperature scaling) prior to recombination in non-irradiated sensors. These results will serve as modelling parameters for the Allpix Squared simulations later.

The computed electric fields conserve the linearity observed in the non-irradiated scenarios, but exhibit a decrease in the field depth after radiation damage from approximately 65 to 40-45 microns (depending on the temperature and judging from figure 2.4). As a consequence, it is expected that charge collection will be diminished considering that less charges will be collected swiftly before they recombine. The implications of this will be investigated in more depth later using the Allpix Squared simulation framework. There are practically no differences in the field depth below the sensitive n-wells which are noticeable when comparing both topologies to each other.

The simulated leakage current curves for both topologies look practically identical and show an (expected) increase in the leakage current after irradiation (by approximately a factor 1000). The results for the irradiated sensors with ISO topology were compared to those measured in [16] and [39] and agree within approximately one order of magnitude, although they show higher values than expected. Agreement between experimental and simulated data could be improved by further optimizing the chosen radiation models to the properties of the HitPix detectors.

3. Allpix Squared simulations and beam profile reconstruction

Allpix Squared [18] is the name of an open source framework for detector simulations. It encompasses the various stages of the detection process, from the geometry of the detector, which can be set up using simple geometrical forms, up to the signal transfer and digitization. It accepts fields from other simulation software like Sentaurus TCAD (from which the doping profiles and electric fields from the last chapter have been imported) and uses Geant4 in order to simulate the interactions with the setup, providing information about charge carrier generation and energy deposition, all while remaining relatively simple to use. This software is used to support the development of beam profile reconstruction algorithms for the HitPix monitoring system.

3.1. Motivation

The simulations are being performed not only to understand the behaviour of the HitPix detectors while under testing, but also to develop appropriate analysis algorithms for the reconstruction of two essential beam characteristics: the beam position and the beam width. The need and importance of a precise monitoring of these parameters have been illustrated in the introductory chapter of this work.

The HitPix detectors are conceived as an array of single detector chips, as illustrated in figure 3.1 (mockup board designed by Bogdan Topko and Felix Ehrler). One disadvantage of this approach is the presence of gaps between the chips, which (as it will be shown in this chapter) bias the beam reconstruction if only using a simple algorithm based on the mean and standard deviation of the hits' profile. One of the main objectives is therefore to implement analysis strategies to overcome this difficulty.

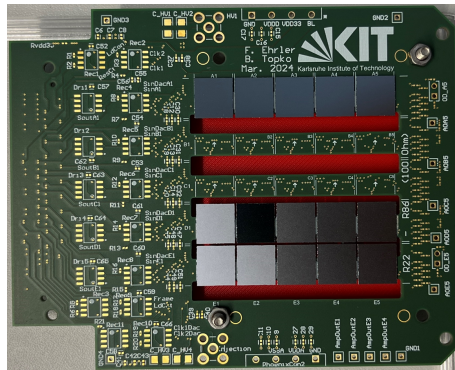


Figure 3.1.: HitPix 5×5 mockup board. The array has been only partially populated with chips as it is only intended for testing of the chip placement.

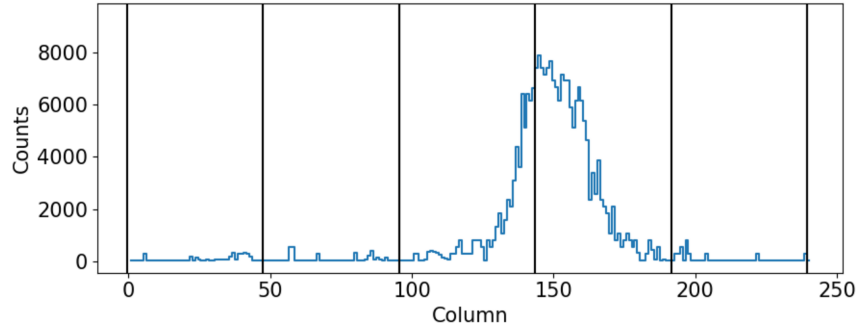


Figure 3.2.: Histogram of hits in adders mode for an 1×5 HitPix 2 array from experimental data provided by Bogdan Topko (carbon ions, $E = 430$ MeV/u and FWHM = 3.4 mm). The vertical lines separate the columns from different detector chips. Each chip has 48 columns of pixels.

The effects of the missing data between the chips can be easily understood by looking at the example data depicted in figure 3.2. It shows the hits registered (in adders mode) for a 1×5 array. Since there is data missing between the third and the fourth chip because of the gap between them, the histogram loses its symmetry. Trying to localize the beam by computing the weighted mean of the histogram would therefore result in a value which is biased to higher column numbers, since the center of mass of the profile is no longer located in the middle (as it would be if the profile was symmetric) but is rather shifted to the right.

A similar effect becomes important for profiles which are near the edge of the array, since the particles going through points outside of the array are not detected (ergo, there is no profile in that part: there is data missing). These not registered hits will not contribute to the weighted mean of the profile and, as a consequence, the center of the beam will be shifted towards the center of the array.

One could argue that a simple algorithm based on the weighted mean is, in consequence, not adequate in this scenario. The specifications of the monitoring system, however, require fast feedback which is not easily achievable by other reconstruction methods (e.g. a Gaussian fit).

That being the case, alternative reconstruction methods based on the mean and standard deviation of the output histograms are going to be explored and implemented with the aim of achieving a robust, reliable and precise algorithm. Since the monitoring system in real treatment scenarios is required to provide fast and reliable feedback, this work will concentrate in developing computation methods for the faster HitPix readout mode (adders mode, see section 1.6).

3.2. Beam profile reconstruction

In the following sections, some important details and considerations about the steps performed during the estimation of the beam characteristics are presented.

3.2.1. Interpolation

A possible solution to the problem described in section 3.1 could be the interpolation of the data, i.e., filling the gaps between the chips in order to approximately restore the symmetry of the profile. There are some aspects that have to be taken into account in order to avoid the introduction of further systematic effects while reconstructing the beam:

- While in counters mode each pixel reports its number of hits individually, in adders mode the hits of all pixels in a row or column are reported together as a sum. Thus, counters mode provides two-dimensional information and adders mode provides only one-dimensional information.
- For a particle going through a given column, it is not possible to determine through which pixel within the column the particle has gone. Therefore, the positions of all pixels within the column are equally valid and should be equally weighted in the calculation of the mean.
- As a consequence of the last points, and since the chips may be rotated by a variable and distinct amount in comparison to other chips, the reconstructed position of the particle will be a smeared projection of a column onto an axis. This smeared projection represents the interval of possible pixel coordinates the particle may have gone through.
- If the rotation of the chips is too big, the gap between them becomes irregular and wedge like. Thus, a strategy has to be found to accurately represent the weight of this region in the calculations at its different positions. However, deciding how many interpolated (filling) points to generate under the condition that the number of points be constant along the gap is not a trivial matter if the distance between the chip edges is variable within a given gap.
- The systematic effects are caused by missing data. When interpolating, i.e. generating additional data, one has to be cautious not to add more data than necessary. That would have a similar but opposite effect: if the data density within the gap becomes higher than in its surroundings because of the additional interpolated data points, the weighted mean (i.e. the center of mass of the profile) will be shifted towards the gap, exactly the same way as the absence of data (zero data density) shifts the mean away from the gap.

Taking into consideration the points above, the following interpolation algorithm has been developed:

1. Compute the distance between edge pixel centers. For an interpolation in x -direction and taking two chips with 48×48 pixels each as an example, the algorithm would compute the distance between the pixel of row n column 48 in one chip and row n column 1 of the neighbouring chip and repeat this for all $n \in [1, 48]$. The same procedure can be applied in y -direction (with the first and last rows of two chips).
2. Calculate how many virtual pixels (with size $200 \mu\text{m} \times 200 \mu\text{m}$) would fit in the connection line between pixel centers. If the resulting number of virtual pixels is not an integer, round up the value to the next integer (overestimating this value by one rather than underestimating it has been shown to work better in scenarios in which the edge pixels are close to each other).

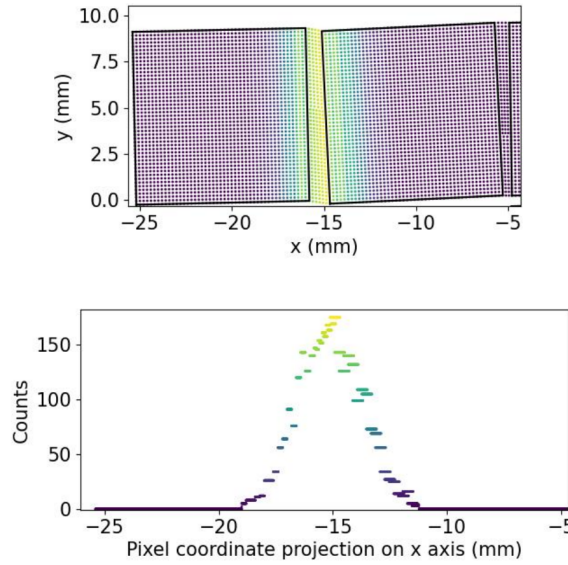


Figure 3.3.: Visualisation of the interpolation algorithm in adders mode for the x -profile. Each point represents the position of a pixel center, its color the hit count. The black lines are the chip boundaries, the pixels in between adjacent chips are virtual pixels generated by the interpolation.

3. If in adders mode, propagate the number of hits in one column to all the pixels in that column. This is done in order to reproduce the possible effects originated by the smeared projection of a rotated chip onto an axis. Calculate the difference in hit counts between equivalent edge pixels.
4. Place the computed number of virtual pixels evenly at the connection line between edge pixels and assign them a linearly interpolated number of hits, hereby bridging the hit count difference between edges.

Examples of the output after the proposed interpolation algorithm is performed are depicted in figures 3.3 and 3.4. Figure 3.3 shows an adders mode output for the x -profile. Figure 3.4 shows the result of applying the interpolation procedure on a 2×5 matrix for the x and y adders projections.

The lower picture in figure 3.3 illustrates some of the features of the algorithm:

- The data points near the peak follow a linear trend, showing the linear interpolation of the hit counts at the gap.
- The smearing of the coordinates of a hit in adders mode is visible and noticeable different on the right and the left side of the profiles. The interval in which the pixel coordinates of one column are spread out is wider on the right side of the profile since the rotation of the chip is higher with respect to the left chip.
- The chosen approach leads to a pixel grid which is approximately homogeneous, the pixel density is very similar to that of the chip itself.

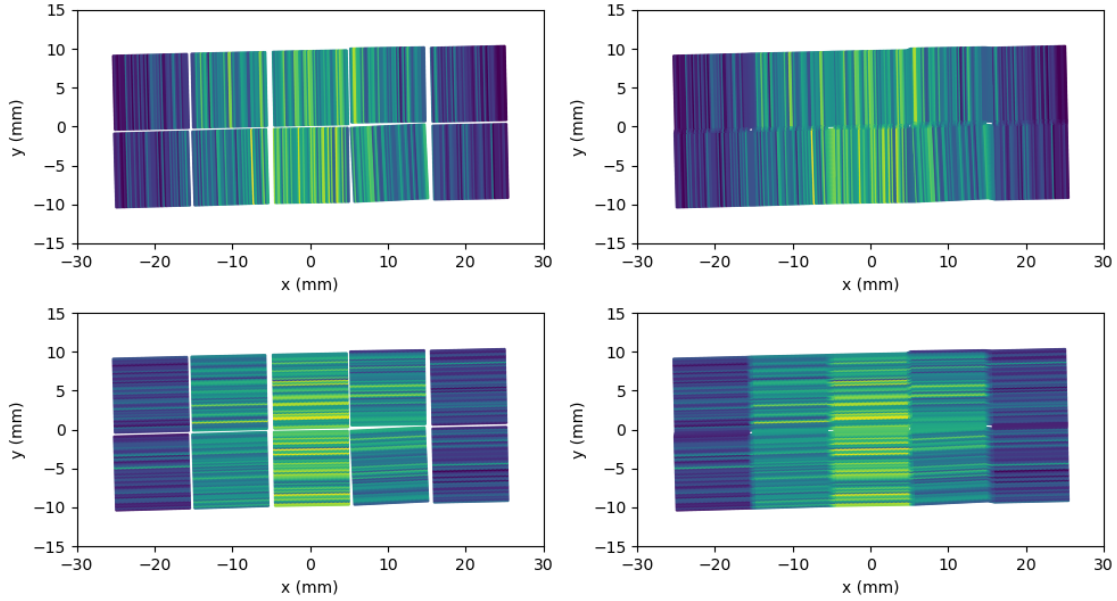


Figure 3.4.: Real 2x5 geometry simulated in adders mode before (left) and after (right) interpolation of the hit profile in for both axis projections. The chips in the real array are HitPix 2 detectors, which only allow one axis projection (upper figures), the other projection was simulated to test the procedure and it is only meant to illustrate the result. The data on each chip column is propagated to all the pixels in the column for the calculations. The arrangement of the chips was derived from optical measurements of the active area of the chips in the matrix. Thanks to Bogdan Topko for the optical measurement of the geometry [40].

3.2.2. Reconstruction algorithms

In the scope of this work, two main beam profile reconstruction strategies will often be compared: the least squares fit to a Gaussian function (abbreviated as *Gaussian fit* for the remainder of this work) and a simple mean/standard deviation algorithm (*simple* algorithm in short). A procedure based on the minimization of the negative log-Likelihood function under the assumption of a Gaussian beam profile was also investigated, but it showed the same bias effects for beams near the edges of the matrix as the simple algorithm, all while still requiring an iterative minimization. It is not clear how this could be implemented in the FPGAs used in the data acquisition system (see section 1.6). For these reasons, the comparisons with this method will be omitted throughout this work. It should be pointed out that the final HitPix matrix will be larger than the area required for monitoring during treatment so that edge effects become less important.

Least squares fits to Gaussian functions are not sensitive to gaps in the data and are more robust when reconstructing beams near the borders of the chip matrix. They deliver, in general, less biased results than their simple counterpart, which makes them a good reference point. The objective is therefore to implement a simple algorithm with comparable accuracy and robustness as a Gaussian fit while not requiring as much computation time and being easier to implement in FPGAs. In the following paragraphs, the main ideas behind this new *simple* algorithm will be discussed.

The monitoring system outputs arrays of information which are used to reconstruct the beam characteristics. The arrays are either one-dimensional (in adders mode), representing the hit counts in each column or row, or two dimensional, containing the hit counts of each pixel. In general, the one-dimensional output is propagated to a two-dimensional array first as depicted in figure 3.3 so as to consider the smearing caused by the rotation of the chips, as explained previously.

In adders mode, a picture like in figure 3.4 can be seen for beams which are wide enough to cover more than one row or column of detector chips. In this illustration, there are five different columns of chips with two chips per column, and each of them delivers a different profile. Looking at the y -profile, for example, it is to be expected that the first and last column will deliver profiles which are not as significant as the one of the middle column or are noisier in comparison, since the beam goes through the center of the 2×5 matrix. The second and fourth columns may deliver a useful part of the profile, but it will be, in any case, different in comparison with the middle profile, which has the majority of the hit counts. In particular, the neighbouring columns will show distributions with a lower amplitude (because of the lower hit counts). Another example is provided in the appendix (see figure B.5).

When using a Gaussian fit to estimate the beam parameters, it is necessary to take into consideration what has been discussed in the last paragraph. One should not fit many different profiles to one curve, as this may influence the results. For this reasons (noise and multiple profiles in one frame), only the row or column (depending if it is the x - or y -profile the one which is being reconstructed) with the largest number of hits is used for the Gaussian reconstruction.

One complication of algorithms based on the mean and standard deviation of the data is that they are fairly sensitive to noise entries, specially if the noise is away from the beam center. To minimize this effect, a noise suppression step (based on the interquartile-range-method) is performed on the remaining data to eliminate outliers. This is done by setting hit counts for pixels far away from the center to zero. In this work, hits at coordinates that are 1.5 interquartile ranges farther away than the first or third quartile of the coordinates of all registered hits are discarded.

Omitting this step leads to a high overestimation of the beam width. Deviations in the range of 500 μm and greater have been observed in simulated data.

Since noise suppression done in this way adds more calculation time for the reconstruction, other methods to reduce noise are preferred for the final version of the detector, like, for example, pixel and column masking and a pixel-by-pixel adjustment of the signal threshold.

The last step is the actual reconstruction of the beam position and width using the cleaned data. The reference method in this work is a least squares fit to a Gaussian function:

$$f(x) = A \exp \left(-\frac{(x - x_0)^2}{2\sigma_x^2} \right) \quad (3.1)$$

The parameters x_0 and σ_x are then taken as estimates of the beam position and width. Since the reconstruction is done using binned (pixel hit counts) data, the associated uncertainty is given by the Poisson distribution, yielding an uncertainty for the hit counts of $\sqrt{N_i}$ for each hit count N_i . The fit is performed by means of the *Scipy* python library under consideration of these uncertainties. The reported uncertainties in the fitted parameters are provided by the fitting algorithm.

For the simple algorithm, the weighted mean of the pixel center coordinates is calculated, whereby the number of hits represent the weights. Similarly, the standard deviation of the data is computed. The estimators for the position and width of the beam (the mean \bar{x} and the standard deviation $\sqrt{\sigma^2}$), are computed as follows:

$$\bar{x} = \frac{1}{N} \sum_i N_i x_i \quad (3.2)$$

$$\sigma^2 = \frac{1}{N-1} \sum_i N_i (x_i - \bar{x})^2 \quad (3.3)$$

Here N_i represent the hit counts of each pixel, x_i the coordinates of the pixels and N the total number of hits.

The Poisson uncertainties on the hit counts are propagated to the (sample) mean \bar{x} and the (sample) standard deviation $\sqrt{\sigma^2}$. It holds:

$$\frac{\partial \bar{x}}{\partial N_i} = -\frac{1}{N^2} \sum_i N_i x_i + \frac{1}{N} x_i = \frac{1}{N} (x_i - \bar{x}) \quad (3.4)$$

$$\Rightarrow (\Delta \bar{x}_N)^2 = \sum_i \left(\frac{\partial \bar{x}}{\partial N_i} \right)^2 (\sqrt{N_i})^2 = \frac{1}{N^2} \sum_i (\bar{x} - x_i)^2 N_i \quad (3.5)$$

Similarly:

$$\frac{\partial}{\partial N_i} (\sqrt{\sigma^2}) = \frac{1}{2\sqrt{\sigma^2}} \cdot \frac{\partial}{\partial N_i} (\sigma^2) = \frac{1}{2\sqrt{\sigma^2}} \cdot \frac{1}{N-1} [(x_i - \bar{x})^2 - \sigma^2] \quad (3.6)$$

$$\Rightarrow (\Delta \sigma_N)^2 = \sum_i \left(\frac{\partial}{\partial N_i} (\sqrt{\sigma^2}) \right)^2 (\sqrt{N_i})^2 \quad (3.7)$$

$$= \frac{1}{4(N-1)^2 \sigma^2} \sum_i [(x_i - \bar{x})^2 - \sigma^2]^2 N_i \quad (3.8)$$

Additionally, the sample mean and variance have an uncertainty which can be calculated as follows[41]:

$$\Delta \bar{x}_s = \frac{\sigma}{\sqrt{N}} \quad (3.9)$$

$$\Delta \sigma_s^2 = \frac{2\sigma^4}{N-1} \quad (3.10)$$

The total uncertainty of the reconstructed parameters is finally estimated as:

$$\Delta \bar{x} = \sqrt{(\Delta \bar{x}_s)^2 + (\Delta \bar{x}_N)^2} \quad (3.11)$$

$$\Delta \sigma = \sqrt{\Delta \sigma_s^2 + (\Delta \sigma_N)^2} \quad (3.12)$$

In adders mode, the hits of one column or row are propagated to all the pixels in the column or row, as described in 3.2.1. This up-scaling of the hits is not important when computing the mean and standard deviation of the data, but becomes relevant when calculating the uncertainties associated with the reconstruction, since it artificially increases the sample size. Therefore, the total number of hits N and the number of hits N_i are scaled down with a factor 48 before making the uncertainty calculations of the simple algorithm.

3.3. Allpix Squared simulations

3.3.1. Configuration

Allpix Squared works in a similar way as Sentaurus TCAD in that it uses a configuration file to set the parameters of the simulations. Some of the essential parts of the modules within this file that are used in this thesis will be presented.

The configuration file starts with a general part introduced by the statement `[Allpix]`.

```
[Allpix]
log_level = "WARNING"
log_format = "DEFAULT"
multithreading = true
workers = 31
model_paths = (...)
detectors_file = (...)
random_seed_core = 5167577923612841943
number_of_events = 30
```

Allpix Squared is able to generate geometries where the detector elements are placed imprecisely so as to reproduce realistic assembly precision. A misalignment in the placement and orientation of the detectors can be defined in the device geometry file, the values are then chosen from a Gaussian distribution with a user defined width. In order to ensure the use of the same randomized geometry for many simulations, the parameter `random_seed_core` can be fixed.

The manner in which the particles are shot and registered at the simulated detector is configured as follows: first, a number of events for each frame is defined in the general configuration module with the statement `number_of_events`. Within each event, a given number of particles (`number_of_particles` in the deposition module below) are shot at the same time. The program then registers which pixels have been set as hit during the event (because the detection threshold of the pixel was exceeded). There is no tracking of the counts yet. The program then repeats this step as many times as it is stated in `number_of_events`. This information can be used later to recreate the hit profile of the frame by histogramming the number of events in which the pixel was registered as hit against the pixels' two dimensional coordinates.

The number of particles shot at the same time is set in the simulation according to the pixel dead time (understood as the minimal time between two signals without pile-up), which is estimated to $3\text{ }\mu\text{s}$ for the HitPix detectors (thanks to Bogdan Topko for the estimate). This dead time can be optimized by the in-pixel analogue electronics settings. The number of particles traversing the detector at the same time within that time window is calculated from the intensity of the beam. The `number_of_events` is then adjusted to the total frame size. If a frame size of $100\text{ }\mu\text{s}$ is desired, for example, 33 events have to be simulated ($33\text{ events} \cdot 3\text{ }\mu\text{s/event} \approx 100\text{ }\mu\text{s}$).

After this section, the module `[GeometryBuilderGeant4]` sets the geometry and, for example, the material present in the surroundings of the detector:

```
[GeometryBuilderGeant4]
world_material = "air"
```

The following `[DepositionGeant4]` section configures the particle source and the list of interactions allowed for the Geant4 module. The number of particles mentioned in the last paragraph can also be set here, as well as the type of beam, its energy, species and size:

```
[ DepositionGeant4 ]
physics_list = FTFP_BERT
beam_direction = 0 0 1
max_step_length = 1.0um
output_plots = 1
source_type = "beam"
number_of_particles = 15
# particle_type = "proton"
particle_type = "ion/6/12/6/0eV/false" # For carbon ions
source_energy = 5161.2MeV
source_position = 0um 0um -5cm
beam_size = 1444um # FWHM/2.355
```

The `physics_list` `FTFP_BERT` is the Geant4 default list. Detailed information about it can be found in [42].

Next is the `ElectricFieldReader` module, which reads the Sentaurus TCAD electric field. After this module, the doping profile is read in the same way by the `DopingProfileReader` module:

```
[ ElectricFieldReader ]
model = "mesh"
output_plots = 1
field_mapping = "PIXEL_FULL_INVERSE"
file_name = "(...)/ISO_293K_intact_ElectricField.apf"

[ DopingProfileReader ]
model = "mesh"
output_plots = true
field_mapping = "PIXEL_FULL_INVERSE"
file_name = "(...)/ISO_293K_intact_DopingConcentration.apf"
```

The standard proprietary `.tdr` files output by Sentaurus cannot be read by Allpix Squared. A conversion has to be made using the `tdx` command tool packed with the software suite. A typical conversion command reads: `tdx -dd "STD_273_intact.tdr"`, which produces the `.grd` and `.dat` files required by Allpix squared. More information can be found in [43].

The `.grd` and `.dat` files resulting from the previous conversion process still have to be processed by Allpix's `mesh_converter` to create the fields which are readable by the modules above. More information about this step can be found in the manual [38].

The TCAD fields imported into Allpix Squared contain only the bulk region of the detector, which extends over a volume of $200 \times 200 \times 300 \mu\text{m}^3$. The metal contacts on the top and bottom of the pixel and the $0.8 \mu\text{m}$ silicon oxide layer on the top of the pixel are external to this volume and are not included (see figure A.3, bottom subfigure). The doping field for irradiated and non irradiated sensors correspond always to those of the non irradiated detectors and do not include the shallow isolation trench depicted in A.3 (bottom subfigure). The electric fields, on the other hand, include the region corresponding to those trenches.

The configuration continues with the definition of the propagation properties of the generated charge carriers. This is done within the `[GenericPropagation]` module:

```
[ GenericPropagation ]

charge_per_step = 50
max_charge_groups = 1000
mobility_model = "masetti_canali"
trapping_model = "ljubljana"
spatial_precision = 1mm
integration_time = 250ns
output_plots = 1

temperature = 293K
fluence = 1e+15/cm/cm

recombination_model="custom"
lifetime_function_electrons="([0]/(1+x/[1]))*pow([2]/[3], 1.5)"
lifetime_parameters_electrons=2.5e-7s, 1e16/cm/cm/cm, 300K, 293K
lifetime_function_holes="([0]/(1+x/[1]))*pow([2]/[3], 1.5)"
lifetime_parameters_holes=1e-5s, 7.1e15/cm/cm/cm, 300K, 293K
```

The first parameters set how many charges are propagated together and how many groups are propagated in total (increasing the charges per step if necessary). The default value for `charge_per_step` is 10 and was increased to 50 to reduce computation time. The entry `max_charge_groups` was left at its default value.

The integration time represents the maximal period of time over which the propagation of the charge carriers is simulated. It was set to match the scale of the expected recombination lifetime of electrons in the non-irradiated material, which was derived in section 2.3. The result for the parameter τ_0^e (presented in table 2.3) was taken as an orientation value for `integration_time`. The time of arrival histograms (ToA, the time needed for the detection threshold to be met) confirm the choice made at this point. The threshold is surpassed at time points far lower than the configured propagation times, which points to the fact that the necessary charge to register a hit is mainly collected swiftly within the first nanoseconds (see figure B.6 in the appendix).

The last section of this module configures the recombination model. In this case, a re-implementation of the Shockley-Read-Hall model is chosen (as defined in equation 2.9) with the knowledge about the parameters won from the Sentaurus TCAD simulations (table 2.3). It is necessary to input the temperature manually, since it does not automatically apply the temperature set with the parameter `temperature`.

The next module `[PulseTransfer]` generates pulses from the charge carriers arriving at the defined implant in the pixel, which are then digitized by the `[DefaultDigitizer]` module:

```
[ PulseTransfer ]
collect_from_implant = true
output_plots_scale = 100ke
output_plots = 1
```

```
[ DefaultDigitizer ]
output_plots_scale = 100ke
output_plots_bins = 400
output_plots = 1
#ISO
threshold = 9600e
threshold_smearing = 728e
electronics_noise = 160e
#STD
# threshold = 7500e
# threshold_smearing = 390e
# electronics_noise = 140e
```

The **DefaultDigitizer** module allows the simulation of electric noise and setting a signal detection threshold.

Values for the electronic noise and threshold smearing are taken directly from [16]. As an example, threshold charge values are estimated from figures 16 and 18 (also in [16]) assuming $Q = CV$ and computing the capacitance from the given proportionality between the standard deviation of the threshold voltage and charge. However, the threshold voltages of the comparator circuit in HitPix can be set manually by the user to improve the signal-noise-ratio. Charge collection simulations will be conducted later to adjust the threshold charges for irradiated sensors. More on this topic will be discussed in section 3.3.3.

The last modules output text files with data registered during the simulation run and creates root files, which contain graphs and data about the results of the individual modules in the respective run:

```
[ TextWriter ]
include = "PixelHit "

[ DetectorHistogrammer ]
```

In this case, the file created by the **TextWriter** module contains per-event information about which pixels where hit. This is used to reconstruct the frame resulting from the simulation run.

3.3.2. STD topology: systematic shift

Early simulations of the standard topology revealed a systematic shift in the reconstructed y -position of the beam in comparison with the true simulated beam position. To test the presence of this effect, 100 simulations (each one representing one frame) were run with the settings in table 3.1 and in the orientation in figure 2.1 (left). The results are presented in figure 3.5.

There is a clear shift in the reconstructed position in y -direction, which is easy to explain considering the position of the sensitive implant in the STD topology. The biggest n-well (see picture 2.1) is placed $37\text{ }\mu\text{m}$ away from the center, which means that the coordinate system of the grid formed by the sensitive charge collection centers (the big n-wells) and the the grid of the pixel centers are not aligned. The signal is collected at a position $y + 37\text{ }\mu\text{m}$ but the reported coordinate for the hit is y . Therefore, the y -coordinate is systematically being underestimated.

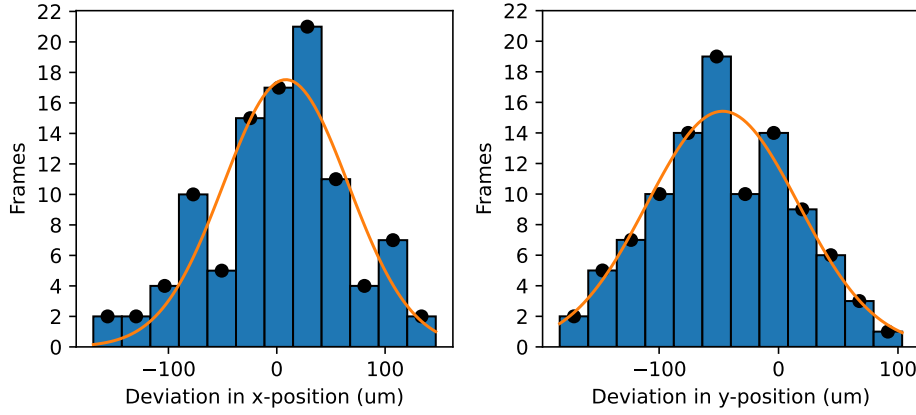


Figure 3.5.: Histogram of the deviations in the position reconstruction observed in STD topology simulations (100 frames) and corresponding Gaussian fit. The fitted parameters are $x_0 = (8 \pm 8) \mu\text{m}$, $\sigma_x = (58 \pm 8) \mu\text{m}$, $y_0 = (-47 \pm 6) \mu\text{m}$, $\sigma_y = (63 \pm 6) \mu\text{m}$. The beam reconstruction was performed using a least squares fit to a Gaussian function.

Table 3.1.: Simulation settings to test the systematic shift seen in simulations with STD topology on a 1×1 matrix. 100 frames in counters mode were simulated.

Events	$N_{\text{tot}} (N_{\text{event}})$	Species
30	18000 (600)	Protons

E (MeV, MeV/u)	FWHM (mm)	\vec{x}_{source} (mm)
221.6 (221.6)	8.1	(0, 0, -50)

Topology	Φ (n _{eq})	T (K)
STD	0	293

3.3.3. Charge collection in irradiated sensors

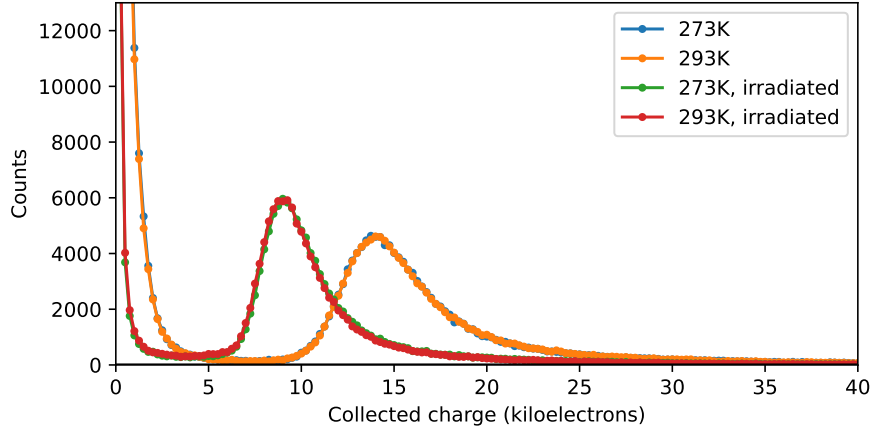
Radiation damage negatively influences the number of charge carriers that reach the electrode after an ionisation event. Fewer electrons reach the electrode due to charge trapping and a lower depth of the depletion zone. To test the extent of these effects, simulations were conducted at two temperatures for irradiated and non-irradiated sensors. The corresponding simulation settings are provided in table 3.2.

A histogram of the raw pixel charge (without electric noise) for all events in the run is provided in figure 3.6. The simulations do not show variations in the charge collection depending on the temperature, which goes against the expectation. Irradiation, on the other hand, leads to a clear decrease in the collected charge of about 35% with respect to the intact sensor (derived from the comparison of the most probable values of the Landau-shaped curves in figure 3.6).

The histograms in figure 3.6 also confirm the validity of the threshold charge stated in section 3.3.1 (`DefaultDigitizer` part), as most of the distribution lies well above that point (9.6 ke^- in the ISO topology). However, for simulations with irradiated sensors and with the same conditions as those stated for this scenario (table 3.2), it seems appropriate to lower this threshold to around 5 ke^- . It should be noted that these thresholds are conservative estimates and could be lowered further, probably improving the efficiency of the detector slightly in comparison to the values reported in section 3.3.4.

Table 3.2.: Simulation settings for the test the charge collection on a 1×1 matrix. Only one frame was simulated.

Events	N_{tot} (N_{event})	Species
180.000	180.000 (1)	Protons
E (MeV, MeV/u)	FWHM (mm)	\vec{x}_{source} (mm)
221.06 (221.06)	8.1	(0, 0, -50)
Topology	Φ (n_{eq})	T (K)
ISO	0 and 10^{15}	273 and 293

**Figure 3.6.:** Histogram of the raw pixel charge (without electric noise) in irradiated and non-irradiated sensors.

3.3.4. Detector efficiency and cluster size on irradiated sensors

The efficiency of the detector and the cluster size were studied in simulations using the settings in table 3.3. This time, the threshold charge was lowered for irradiated sensors to 5 ke^- when using proton beams. Events with only one particle being shot at the detector were simulated. As a reminder: during an *event* in Allpix Square, many particles may be shot at the same time. Therefore, hits from neighbouring particles can combine to one single (larger) cluster and, as a consequence, the single clusters are not distinguishable from each other. Shooting only one particle at a time ensures that this does not happen.

Both evaluations are performed using Allpix Squared's built-in tools. In the software, adjacent hits and clusters are combined to form larger clusters, pixels not assigned to a cluster are assigned to their own cluster. The efficiency assessment is done by correlating the position of a cluster to the particle true position within a given maximal distance between the former and the latter (three times the pixel size in both directions by default).[38]

Regarding the cluster sizes, protons almost always produce clusters comprised by one pixel only. In contrast, carbon ions produce clusters of two or more pixels more often. Two possible explanations for this are the increased ionisation as well as the generation of secondary particles which carry the energy away from the center of the ionisation event. Nevertheless, this trend is reversed after irradiation, which is to be expected due to the lower charge collection after irradiation. These results are presented in figure 3.8.

It should be noted that the cluster size is highly dependent on the threshold set at the detector. The amount of charge created by an ionisation event diminishes with the distance from the particle path through the detector. Therefore, the hits on the edges of the cluster will be due to weaker signals which can be filtered out by increasing the detection threshold.

Table 3.3.: Simulation settings for the test of the detector’s efficiency and cluster size on a 1×1 matrix. Only one particle per event was shot at the detector.

Run	Events	N_{tot} (N_{event})	Species
1	180.000	180.000 (1)	Protons
2	20.000	20.000 (1)	Carbon ions

Run	E (MeV, MeV/u)	FWHM (mm)	\vec{x}_{source} (mm)
1	221.06 (221.06)	8.1	(0, 0, -50)
2	1065.96 (88.83)	9.8	(0, 0, -50)

Run	Topology	Φ (n_{eq})	T (K)
1	ISO	0 and 10^{15}	273 and 293
2	ISO	0 and 10^{15}	273 and 293

Two efficiencies are under study in this section: the detector efficiency and the pixel efficiency. The former takes the hit cluster produced by the ionizing particle and compares the position of the cluster center with the true position of the simulated particle. If a cluster center is found within a given maximal distance (three times the pixel pitch in x - and y -directions by default) from the true particle position, then the particle counts as detected. With this data, an efficiency map of the detector is produced depicting the pixel array and the computed efficiency in dependence on the pixel which was hit by the particle. The latter efficiency, on the other hand, refers to the ratio of detected particles depending on the true simulated position at which the pixels themselves were hit by the particle. The corresponding graph depicts a map of only one pixel and the detection efficiency depending on where the pixels were hit within their $200 \times 200 \mu\text{m}^2$ boundaries.

The results of the efficiency analysis are provided in figure 3.7. No clear temperature dependence can be seen in the simulated data, in contradiction to experimental data [39]. The average detector efficiency computed from the detector efficiency map of the whole sensor before irradiation is around 98%. The average pixel efficiency computed from the pixel efficiency map is 88%. After irradiation, there is a drop in the efficiencies. In particular, the pixels now show a $5 \mu\text{m}$ thick insensitive area at their boundary in the simulated scenario (judging from the pixel efficiency map). The average detector efficiency drops to around 94%, the average pixel efficiency to 85%. Neither the efficiency loss at the pixel border nor on the detector have been observed in simulations done with carbon ions. This is likely due to the fact that carbon ions ionize more and the charge cloud extends over a wider area. Therefore, even particles hitting the border of a pixel will generate charge clouds wide enough to go beyond the insensitive area of the pixel.

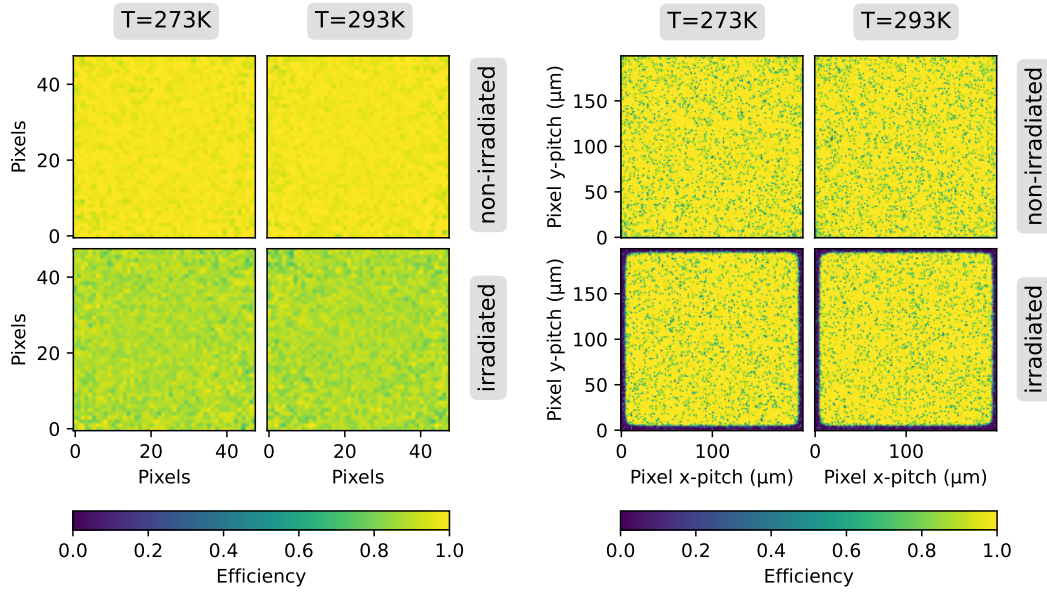


Figure 3.7.: Efficiency maps of ISO sensors before (top) and after (bottom) irradiation (simulated proton beam with the settings in table 3.3). Left group: efficiency map of the 48×48 pixel matrix. Right group: efficiency map of a single pixel in dependence on the particle position.

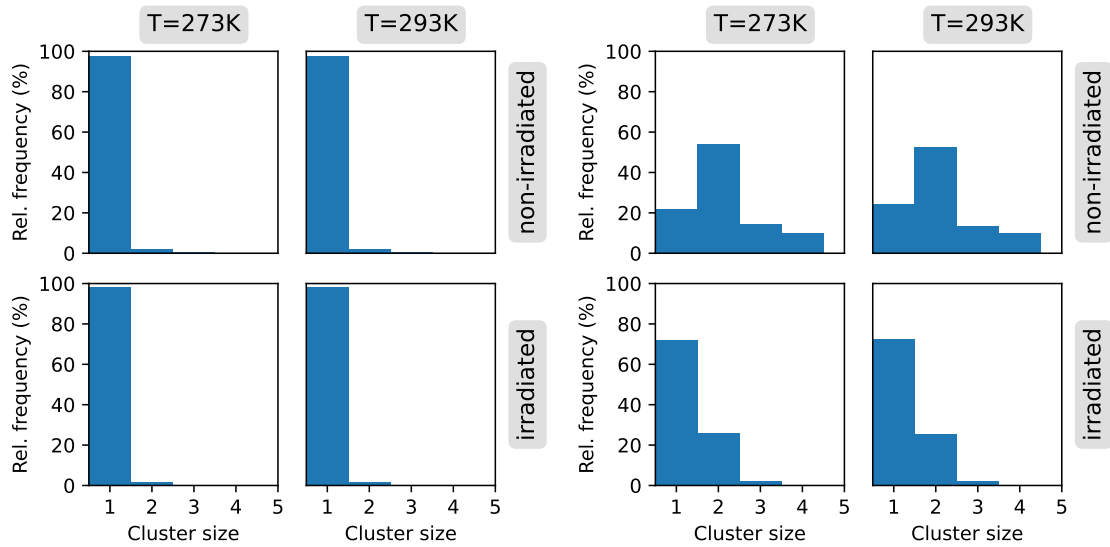


Figure 3.8.: Cluster size in ISO sensors before (top) and after (bottom) irradiation. The left picture group corresponds to the simulation results for protons, the right group for carbon ions.

Table 3.4.: Simulation settings to test the reconstruction algorithms against experimental data. The setup is a HitPix 2 2×5 matrix with the geometry presented in figure B.7. These settings reproduce the experimental setup during the measurement. The frame size amounts to $350 \mu\text{s}$. 10 frames were simulated for each beam position.

Events	N_{tot} (N_{event})	Species
117	1755 (15)	Carbon ions
E (MeV, MeV/u)	FWHM (mm)	\vec{x}_{source} (mm)
5161 (430)	3.4	$(-24, 6, -1000)$ to $(24, 6, -1000)$ in 3 mm steps
Topology	Φ (n_{eq})	T (K)
STD	0	293

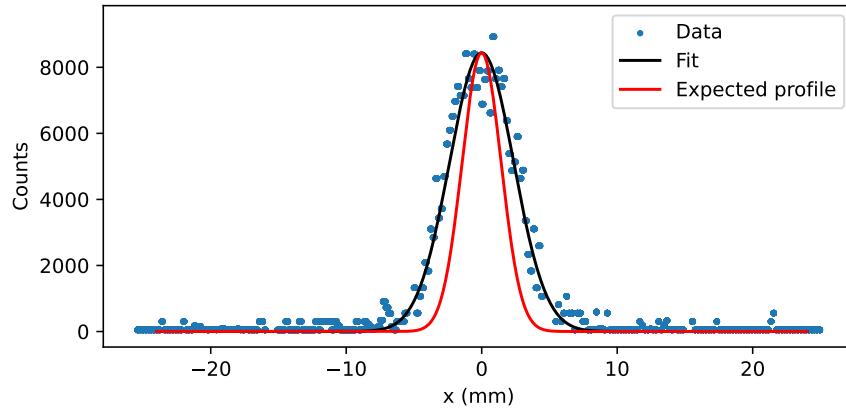


Figure 3.9.: Profile reconstruction from beam test at HIT (carbon ions, $E = 5161 \text{ MeV}$). Depicted are the adders mode data (already propagated as described in section 3.2.1 and projected onto the x -axis), the Gaussian reconstructed profile (with fitted parameters $A = 8439 \pm 3$, $x_0 = (72 \pm 7) \mu\text{m}$ and $\sigma_x = (2.3715 \pm 0.0005) \text{ mm}$) and the comparison profile with same A and x_0 but with the width σ_x set to the expected value ($\sigma_x = 1.44 \text{ mm}$, as stated in the specification sheets).

3.3.5. Algorithm validation

In order to test and validate the interpolation routines presented in section 3.2, the reconstructed beam characteristics in experimental and simulated data are compared. The experimental data from a beam test conducted at HIT which is used in this section was provided by Bogdan Topko (ETP, KIT) [40]. Please note that, due to a decoding error in the detector, the hit counts reported are not accurate and require re-scaling. This is only a scaling problem and should not change the shape of the peak, but will lead to an underestimation of the reconstruction uncertainty. The simulation settings, which mirror the conditions during the experiment, are presented in table 3.4.

Although no problems were found in the position reconstruction in experimental data, the beam width reconstruction has proven to be challenging, since the actual width of the beam at HIT is higher than reported in the specification sheets. Even the Gaussian fit provides overestimated values, as shown in figure 3.9. Future versions of the presented algorithms intended for HIT should consider this aspect carefully.

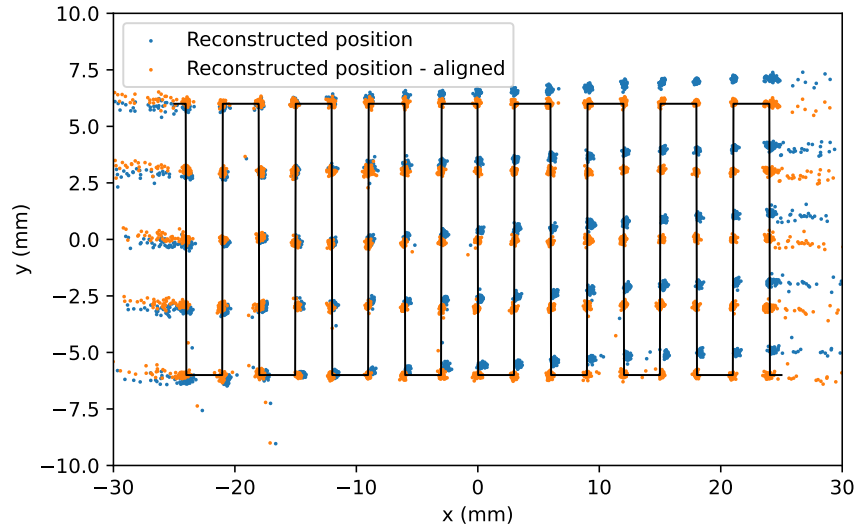


Figure 3.10.: Alignment of the 2×5 matrix to the coordinate system of the beam at HIT. The black line represents the treatment plan (beam path) used for the measurement. The dots (blue and orange) represent the Gaussian-fitted positions of the beam before and after the alignment.

3.3.5.1. Matrix alignment

The local coordinate system of the detector matrix had to be aligned first with the coordinate system of the beam. This was done by using a separate measurement in counters mode with the settings (species, energy and width) in table 3.4.

After cleaning the data of noisy pixels, a Gaussian fit was used to reconstruct the position of the beam in the local coordinate system depicted in figure B.7. The real (reference) position of the beam was deduced from the irradiation plan, which was a rectangular scanning pattern with 3mm spaces which includes the beam central point ($x=0, y=0$), as well as from the beam records from the HIT monitoring system (which helped to understand the path followed by the beam).

In the next step, the reference positions and the fitted values (in the local coordinate system of the matrix) were plotted together for visualisation. All the fitted points within a radius of 1.5 mm from the reference (real) beam position were classified as belonging to that position. The average position then was calculated within each group of points.

The grid formed by the averages was then compared to the grid formed by the reference beam positions. Minimizing the distance between the points in both grids provided the relative rotation and translation between both coordinate systems: the local, as in figure B.7, and the global, given by the treatment plan used for the measurement. There was no re-scaling of the coordinates involved.

The result of the alignment procedure is illustrated in figure 3.10. The relative translation and rotation between the global and local coordinate systems were used to adjust the simulation's geometry to the experimental conditions.

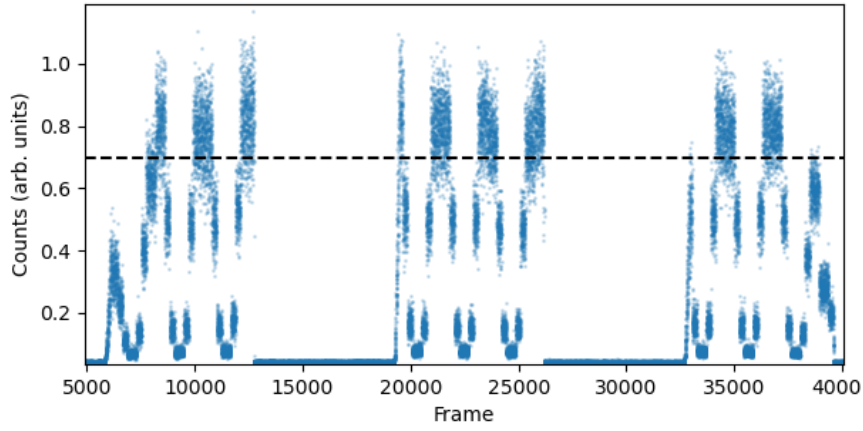


Figure 3.11.: Beam intensity profile at HIT during the measurements with the 2×5 matrix. The counts on one of the rows during one pass of the beam through the detector are shown. The frames with intensities upwards of the dashed line were used for the analysis in section 3.3.5.2. The beam was a carbon beam with $E = 430 \text{ MeV/u}$ and $\text{FWHM} = 3.4 \text{ mm}$. The frame size was $350 \mu\text{s}$. The measured hit counts become lower as the beam leaves the region covered by the detector row.

3.3.5.2. Online reconstruction

The behaviour of the detector under online readout conditions was tested using a measurement in adders mode with the same settings and treatment plan as in the previous section. The measurements were conducted with a HitPix 2×5 array, hence only one adders projection is available and therefore only the x -profile can be reconstructed.

Noisy columns or column clusters were bridged by replacing their hit value with the average of the two closest ones with well behaved values. Only one row of the 2×5 matrix was used for the analysis (see figure 3.12).

It is expected that the reconstructed parameters will fluctuate around a mean during monitoring. To dampen these fluctuations and to provide a somewhat reliable and stable parameter to the monitoring system, the rolling average of the reconstructed values can be used as an estimate. This rolling average considers the state of the beam at previous time points but also is able to react to changes quickly enough to stop the treatment if a meaningful deviation is detected. An exponential rolling average was selected for this task. It is implemented as a time series defined by:

$$s_0 = x_0, s_t = \alpha x_t + (1 - \alpha)s_{t-1} \quad (3.13)$$

Here, the parameter t represents the sequence of frames and is a natural number. Equation 3.13 describes how the reconstructed parameter changes with new information: it weights the current data point with a factor α and the old with the factor $(1 - \alpha)$. The selection of the parameter α hence controls how fast the mean reacts to new input.

As depicted in figure 3.10, the scan covers the whole 2×5 matrix tested in the experiment, but only the upper row is used. To filter the frames in which the beam is mostly contained within that row, only the frames with a high number of hits in the upper row is chosen. Intensity fluctuations of the particle spill were observed during the experiment, which are also documented in [44]. Figure 3.11 is provided to illustrate the intensity profile of the beam measured by the chosen row of the 2×5 matrix.

The results from using different reconstruction algorithms and the performance of the exponential rolling average for experimental data are presented in figure 3.12. The interpolation described in previous sections improves the performance of the simple algorithm and brings it closer to the results obtained from a Gaussian fit, while being faster. It is difficult to ascertain how much quicker the simple algorithm with interpolation will be in the final deployment. It will likely depend on the implementation of the routines on an FPGA.

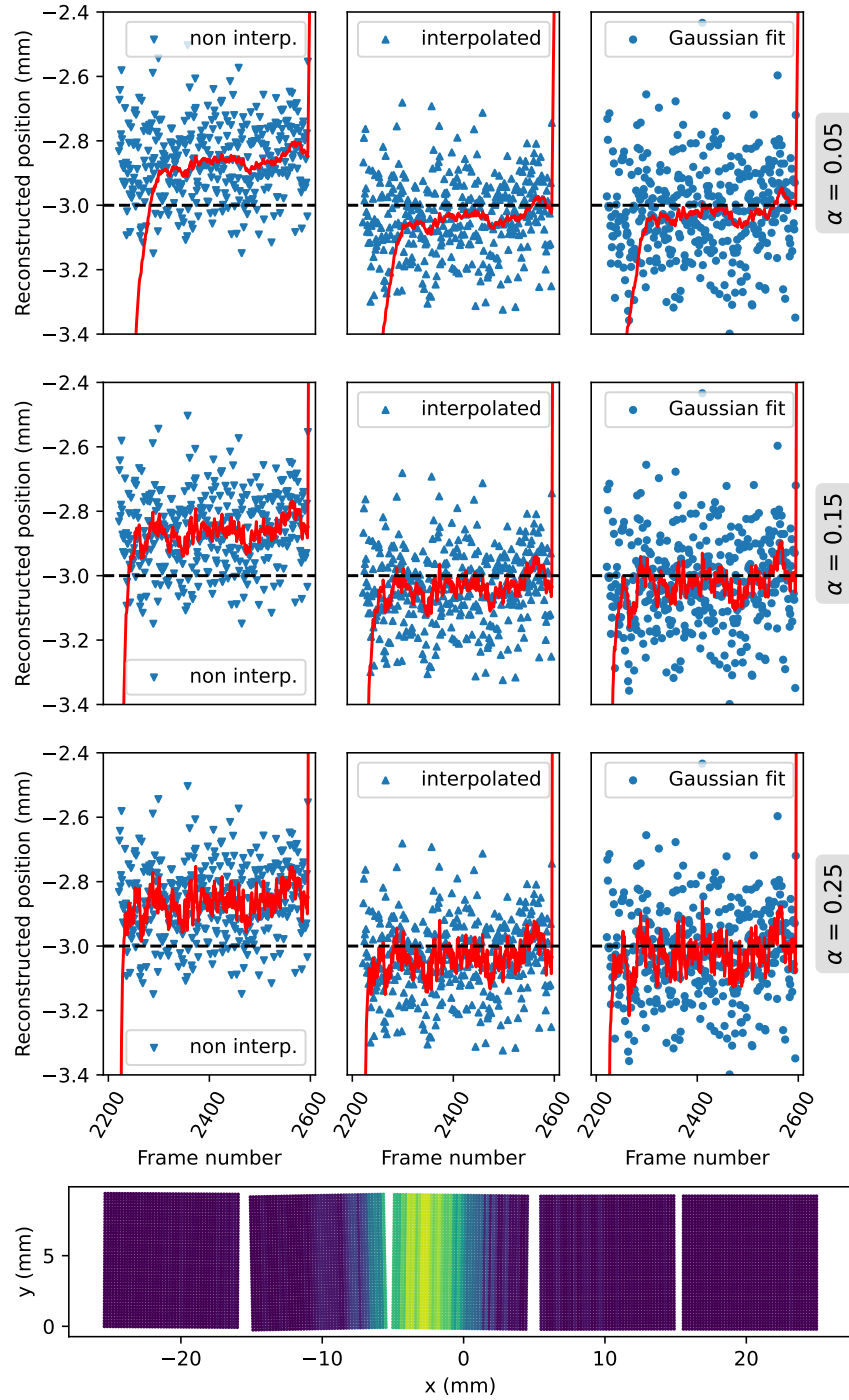


Figure 3.12.: Top: Position reconstruction using the simple algorithm with and without interpolation as well as using a Gaussian fit for the source position $x_s = -3$ mm (indicated by the dashed black line). The beam settings (species, energy and width) are those stated in table 3.4. The frame size amounts to $350 \mu\text{s}$, therefore each spot in the matrix was irradiated for approximately 140 ms. The red lines represent the exponential rolling average with smoothing factors $\alpha = 0.05$ (first row), $\alpha = 0.15$ (second row) and $\alpha = 0.25$ (third row). Notice the faster response of the average for higher values of the smoothing factor α . The red line comes from the area of the graph with the data for $x_s = -6$ mm and continues further to $x_s = 0$ mm. Bottom: Example event with geometry from a real measurement as analyzed with beam at position $x_s = -3$ mm.

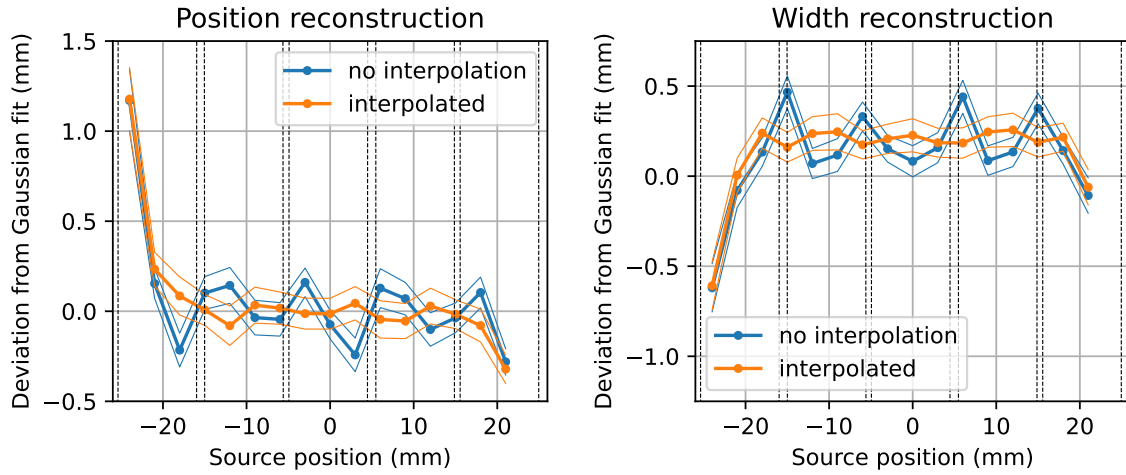


Figure 3.13.: Position and width deviations of the simple algorithm from results using the Gaussian algorithm in experimental adders data of a real 2×5 matrix as a function of the source position. The black dashed vertical lines represent the boundaries between chips. The points represent the mean reconstructed values for ~ 400 frames for each beam position. The thinner lines are drawn one standard deviation (calculated from the reconstructed values for 400 frames for each beam position) above and below those means. The uncertainties of the reconstruction are not presented since the sample size is artificially high as a consequence of a decoding problem in the detector (which reduces the uncertainties).

3.3.5.3. Performance of the simple algorithm with respect to the Gaussian fit in experimental data

The position and width reconstruction in experimental data were further compared to the values obtained from the Gaussian fit to assess the quality of the procedure with the Gaussian approach as reference, the performance of which was presented in figure 3.12.

As seen in figures 3.13, the deviations are greatly reduced by the interpolation. The position deviations remain small for areas away from the matrix borders. This further confirms the effectivity of the approach used to correct the deviation produced by gaps between the chips. The position of beams hitting near the matrix border are systematically over- and underestimated, as discussed in section 3.1. Nevertheless, the beam width is being overestimated in comparison with the Gaussian fit by about $250 \mu\text{m}$, even after the interpolation, although the abrupt variations near the gaps are smoothed.

3.3.5.4. Simple algorithm's performance in simulations

For the simulations, the experimental settings were replicated (see table 3.4). The adders mode is reproduced by taking the normal simulation output and summing the hit counts within a pixel column.

Ten frames for each of the seventeen uppermost beam positions (see figure 3.10) were simulated to check the performance of the simple algorithm. The reason for the reduced number of frames is the computing time required by Allpix Squared. As a reference, the computing time to produce this dataset with the simulation settings presented in the previous sections was approximately 2,5 days with an AMD Ryzen 9 5950X processor.

The simulation results are provided in figures 3.14. The position and width reconstruction is improved by the interpolation. The width is still being overestimated as seen in real data, although not as pronounced. The uncertainty associated with the position reconstruction stays around $40 \mu\text{m}$. The uncertainty of the width reconstruction is relatively high at around $130 \mu\text{m}$.

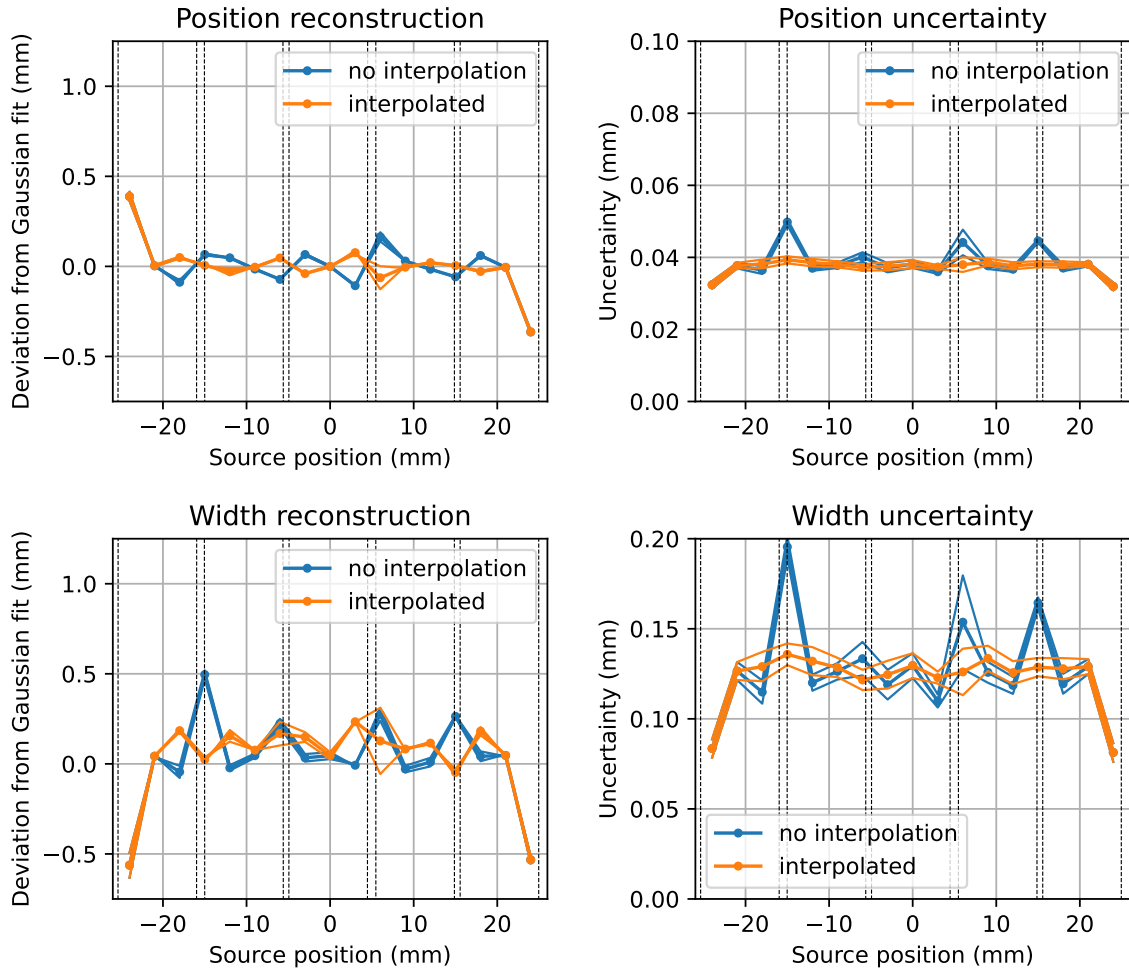


Figure 3.14.: Position and width deviations of the simple algorithm from results using the Gaussian algorithm in simulated adders data of a real 2×5 matrix as a function of the source position. The black dashed vertical lines represent the boundaries between chips. Left column: The points represent the mean reconstructed values for 10 frames for each beam position. The thinner lines are drawn one standard deviation (calculated from the reconstructed values for 10 frames for each beam position) above and below those means. Right column: Each frame is reconstructed with an uncertainty. The means and standard deviations of those uncertainties for each beam position are depicted the same way as in the graphs of the first column.

Table 3.5.: Simulation settings for the test the limits of the interpolation algorithm using different gap widths between the chips of a 1x2 matrix. 10 frames were simulated for each source position and configuration. Since carbon ion beams at HIT have the smallest width, they were chosen for the simulation.

Events	$N_{\text{tot}} (N_{\text{event}})$	Species
30	450 (15)	Carbon ions

E (MeV, MeV/u)	FWHM (mm)	\vec{x}_{source} (mm)
5161.2 (430)	3.4	$(x, 0, -50), x \in [0, 30]$

Topology	Φ (n _{eq})	T (K)
ISO	0	293

3.3.6. Limits of the interpolation algorithm

To test the limits of the algorithm regarding the maximal size of the gap to bridge, a 1x2 matrix was simulated. The chips were placed symmetrically with respect to the y -axis (one on the left, one on the right, both chip centers had the same distance to the y -axis). They were not rotated but were separated by increasingly wide gaps ranging from 0.6 mm up to 2 mm (measured from the to edge of the active areas). The centers of the active areas themselves were 10.2 mm to 11.6 mm apart from each other. The remaining simulation settings are summarized in table 3.5.

The data for the analysis was comprised of ten frames for each beam position and separation of the chips. Each frame consisted of 30 events in which 15 particles were shot at the same time. The position and width reconstruction was performed using the simple algorithm with and without interpolation and for the adders x -projection in HitPix 2 and HitPix 3 (see figure 1.11). The deviations from the configured source position and width were calculated and averaged to produce the graphs in figure 3.15.

The results confirm again the validity of the approach up to a limit in gap width of about 1.2 mm. Beyond that limit, the average deviations become larger than the design tolerances (see section 1.2.1). This is valid for HitPix 2 as well as for HitPix 3. One can also conclude that the differences between the adders projections of both HitPix versions will not be large. The question remains if it is feasible to produce an array with such constraints on the distance between chips. This topic will be discussed in the next section.

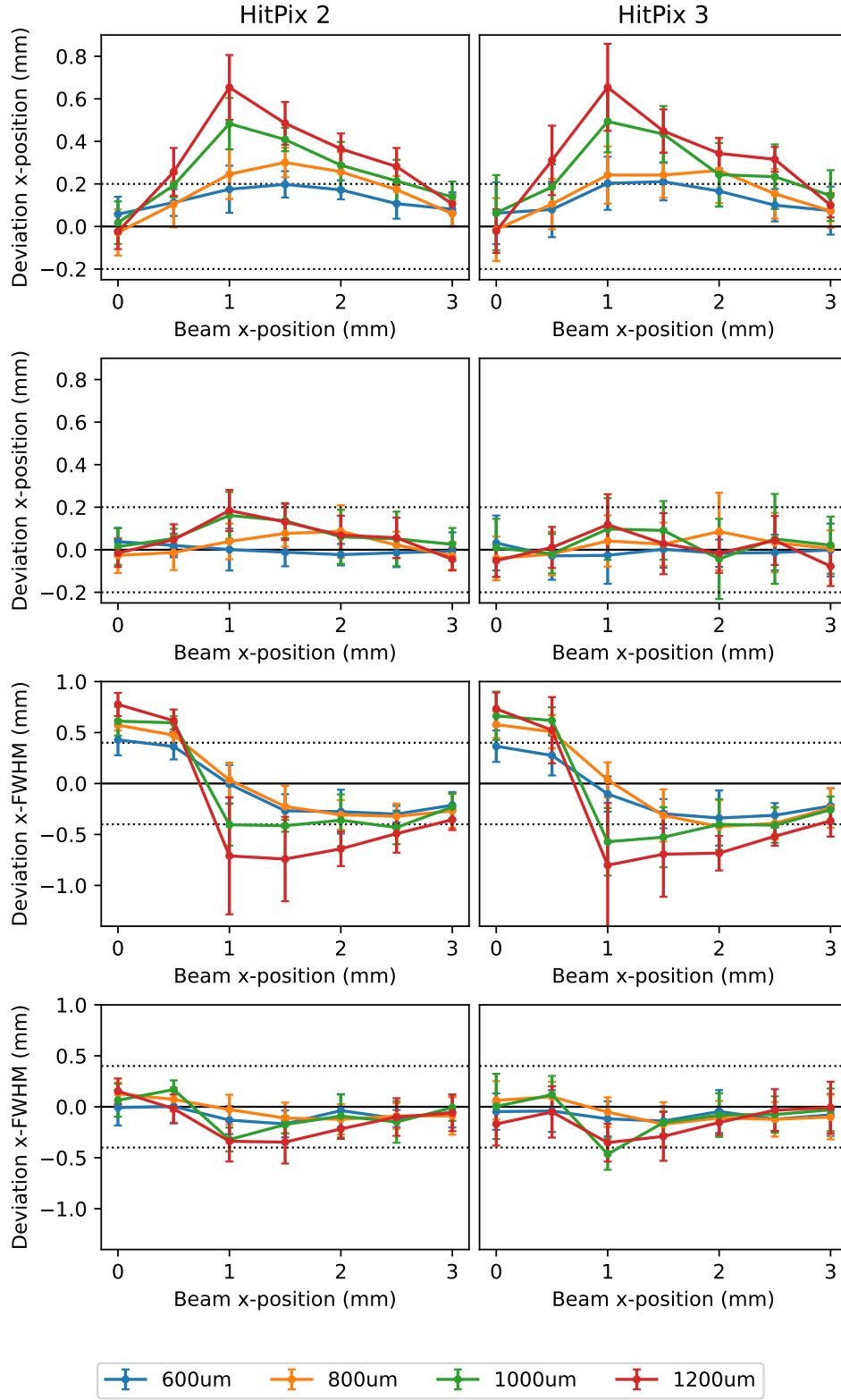


Figure 3.15.: Position and width deviations as a function of the source x -position for varying gap size (between the edges of the active areas of a 1×2 ISO matrix) seen in reconstructions using the adders mode of HitPix 2 (left column) and HitPix 3 (right column) before (first and third rows) and after (second and fourth rows) interpolation. Data taken from the averages of ten frames for each beam position and separation, the error bars represent the standard deviation from those ten frames. The dotted black lines represent the design tolerances discussed in section 1.2.1. Only the gap sizes up to 1.2 mm are plotted for visibility.

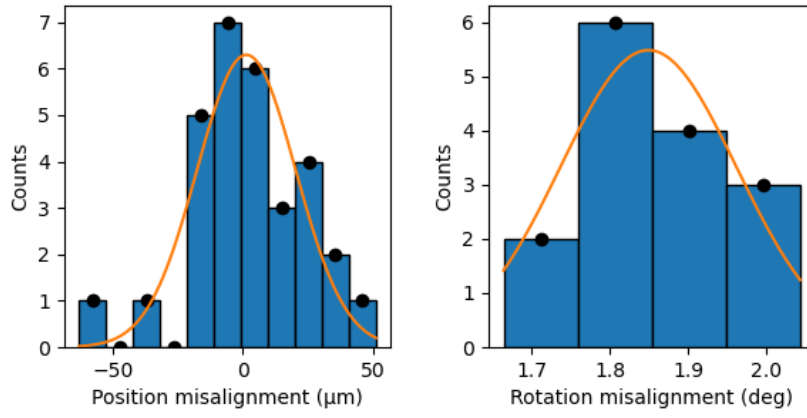


Figure 3.16.: Position and rotation misalignments observed in the 5×5 array mockup in figure 3.1 and corresponding Gaussian fits. The obtained alignment precisions are $\sigma_x = (19 \pm 3) \mu\text{m}$ in position and $\sigma_\alpha = (0.11 \pm 0.04) \text{deg}$ in orientation.

3.3.7. 5x5 matrix geometry simulation, alignment precision

In order to simulate the response of a 5×5 demonstrator matrix a geometry has to be generated. To this end, the precision of process used to arrange the chips on the PCB was assessed by using optical measurements of their position after being placed in the mockup matrix in figure 3.1.

The position of the four outer corners of each chip were measured. From there, the center was calculated by building a simple average. The point grid formed by the centers was fitted to a reference grid with an inter-center distance of the chips given by the PCB design, so as to align both grids. The inter-chip distance in the design is $10\,295 \mu\text{m}$ in x - and $10\,700 \mu\text{m}$ in y -direction, considering that the detector chips are taller than higher, since the pad region is at the bottom of the chips. The deviations (distance in x - and y -direction of each center to the corresponding reference grid point) were then calculated and histogrammed together (given the assumption that the precision of the machine in x - and y -direction is equal).

Furthermore, the rotation of each individual chip was estimated by looking at the slope of each edge using two points at a time, after which the average of the slopes of the four edges was built. The resulting rotation values were then histogrammed. The resulting distribution is not centered around zero since the matrix likely had a minimal global rotation during the optical measurement as a consequence of the manual placement of the device under the microscope.

The histograms were then fitted to Gaussian curves to get the standard deviation of the respective misalignment (position or orientation). This is then used as input for Allpix Squared, which generates a random geometry given the configured precision.

The results of this procedure are presented in figure 3.16. The precision with which the chips are arranged in the matrix is $\sigma_x = (19 \pm 3) \mu\text{m}$ in position and $\sigma_\alpha = (0.11 \pm 0.04) \text{deg}$ in orientation.

Given the parameters obtained, a 5×5 array with horizontal and vertical distances between the chip centers of $10\,295 \mu\text{m}$ and $10\,700 \mu\text{m}$, respectively (which corresponds to gap widths between active areas of $695 \mu\text{m}$ in x - and $1100 \mu\text{m}$ in y -direction) and placed with $25 \mu\text{m}$ precision in the position alignment and 0.15deg in the orientation alignment was randomly generated by Allpix Squared.

Table 3.6.: Simulation settings to test the simplified algorithms in a 5×5 matrix. 10 frames were simulated for each source position and configuration. The random positions were chosen away from the matrix borders.

Events	$N_{\text{tot}} (N_{\text{event}})$	Species
33	19800 (600)	Protons
E (MeV, MeV/u)	FWHM (mm)	\vec{x}_{source} (mm)
221.06 (221.06)	8.1	$z = -50, (x, y)$ random
Topology	Φ (n _{eq})	T (K)
ISO	0 and 10^{15}	273 and 293

All geometries include a PCB on the back and a piece of kapton foil on the front as passive materials to simulate the effects of the board and protection films. An example of how to produce a detector geometry (applied to the case of this section) is provided in the appendix (see B.5).

3.3.8. Algorithm performance in a simulated 5x5 matrix

The geometry from the previous section is used for the final set of simulations. The aim is to assess the performance of the *simple* algorithm in various scenarios: irradiated and non-irradiated sensors at two different temperatures. Furthermore, the HitPix 3 adders mode (with every second pixel contributing to the hit count sum, see figure 1.11) was put to the test against the HitPix 2 adders mode. The simulation settings are summarized in table 3.6. Ten coordinates pairs were randomly generated within a region away from the borders of the matrix (to avoid edge effects) and used as the simulated source position.

An additional simplification of the already simple algorithm was evaluated as well. Instead of propagating the adders counts to all the pixels in a column or row and then projecting all those pixel coordinates onto the axis, only the average x - and y -coordinates from all the pixels belonging to a column or row (respectively) of a given chip were used. The hits of the column or row were assigned to that coordinate and the profile was reconstructed from there. This yields a peak which resembles the one in figure 3.2, but with the average coordinates of the columns (for the x -profile) and rows (for the y -profile) on the horizontal axis of the histogram. The gaps between chips were interpolated in the same way as previously but, this time, only in one dimension: the coordinates of the edge columns or rows of two neighbouring chips were compared, the number and coordinates of the virtual pixels calculated (given the pixel size) and the hits linearly interpolated from edge to edge. This was done for all the chips in a row or column of the matrix, the resulting profiles were overlapped (as seen in figure B.5 but with only one pixel per row or column of pixels instead of 48).

This further simplification is only advisable for matrices with a very low rotation of the chips, as the smearing of the column's (row's) projection is no longer considered. For precisely arranged matrices, however, this is less of a problem, since the smear is negligible. As it will be shown, the simulations warrant the approximation in a geometry with an orientation alignment precision of $\sigma_\alpha \leq 0.15$ deg.

Lastly, these runs were made for the lowered threshold suggested in section 3.3.3 for irradiated sensors as a consequence of the reduced signal (5 ke^-).

The simulations yielded the results presented in figures 3.17 (for the position reconstruction) and 3.18 (for the width reconstruction).

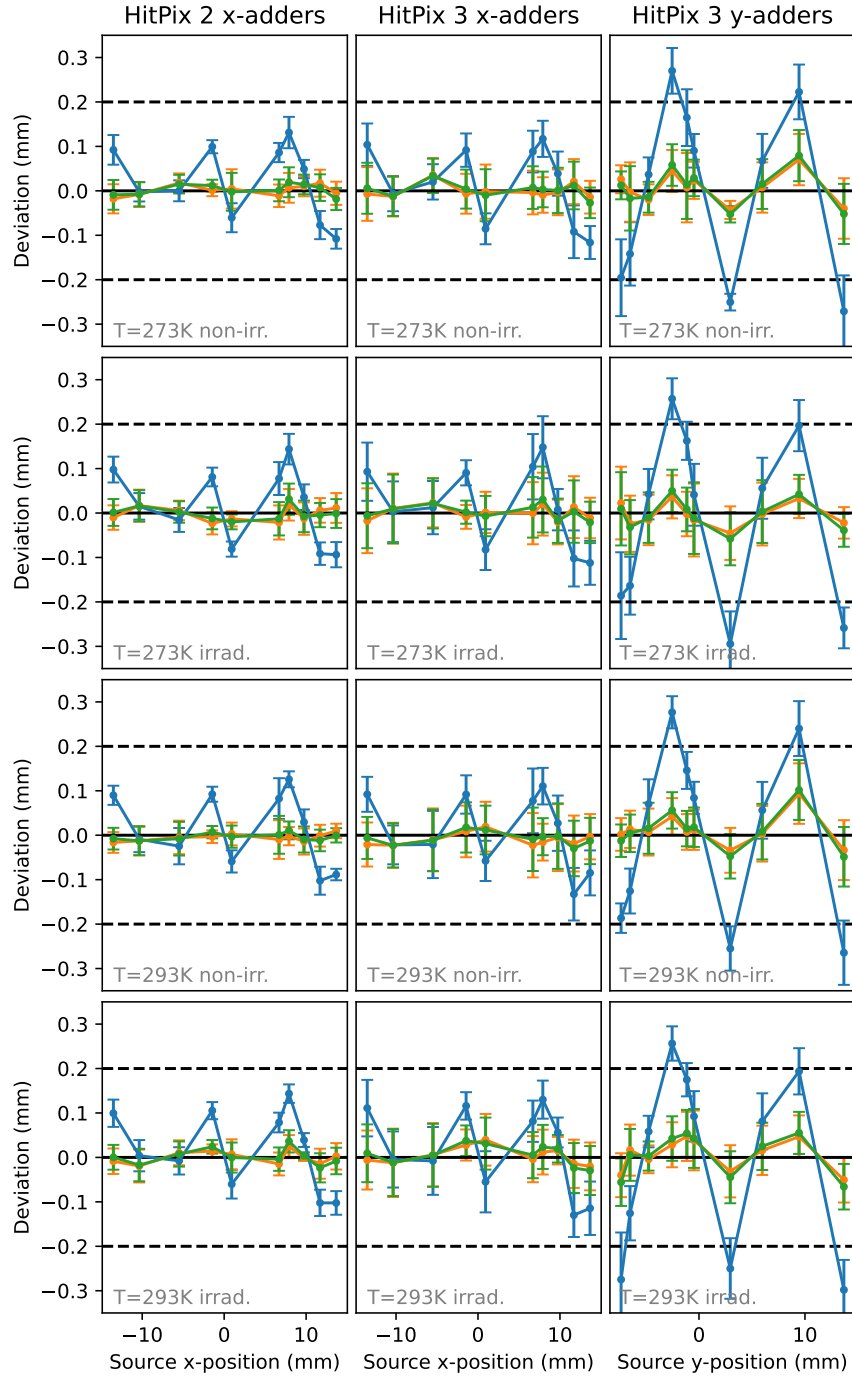


Figure 3.17.: Deviation of the position reconstruction compared to the simulation truth as a function of the source position for the 5×5 matrix geometry derived in 3.3.7 and the settings in table 3.6. The left column depicts the results for the HitPix 2 adders mode, the center column for HitPix 3 adders mode in its x -projection and the right column for HitPix 3 in its y -projection. The blue lines represent the reconstruction without interpolation, orange with the 1D-interpolation and green with the 2D-interpolation. The dash lines shows the design tolerances. The error bars represent the standard deviation of the reconstructed parameters for each source position.

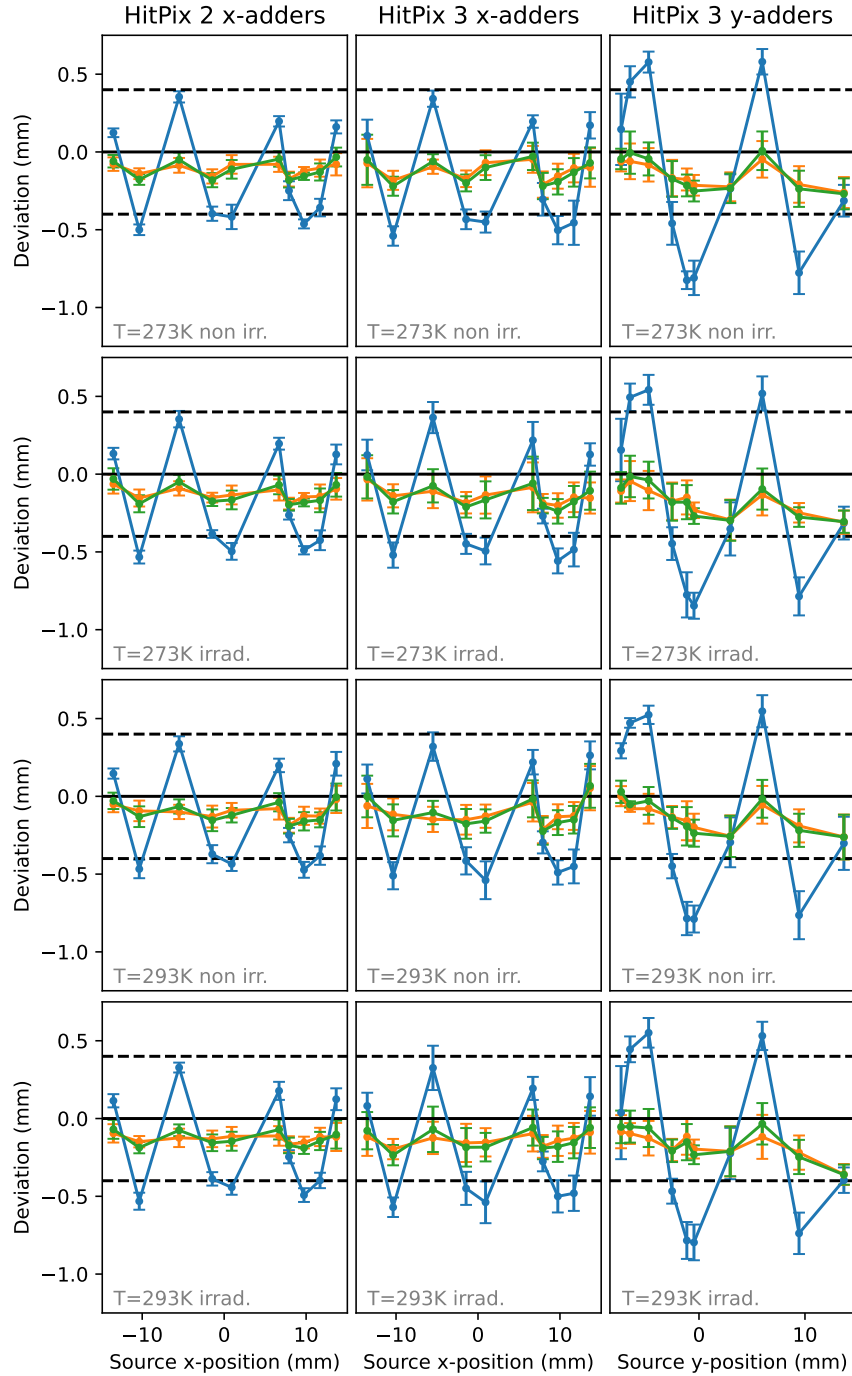


Figure 3.18.: Deviation of the width reconstruction compared to the simulation truth as a function of the source position for the 5x5 matrix geometry derived in 3.3.7 and the settings in table 3.6. The left column depicts the results for the HitPix 2 adders mode, the center column for HitPix 3 adders mode in its x -projection and the right column for HitPix 3 in its y -projection. The blue lines represent the reconstruction without interpolation, orange with the 1D-interpolation and green with the 2D-interpolation. The dash lines represent the design tolerances. The error bars represent the standard deviation of the reconstructed parameters for each source position.

The trend is the same as observed until now: the interpolation is able to reduce the deviations produced by gaps considerably. The one dimensional interpolation method also seems to have a similar performance as the two dimensional counterpart, which will be beneficial in real monitoring scenarios since fast feedback is required. A light underestimation of the reconstructed width is observed, which is probably due to the de-noising algorithm being too aggressive in this case. Since the noise suppression step eliminates counts away from the peak, the variance of the data is reduced, which in turn leads to the observed lower standard deviations. This is intentional, as outliers increase the width significantly. The performance of the HitPix 2 and 3 adders mode is also similar. Larger deviations are nevertheless seen in the y -profile reconstructions of in HitPix 3 adders mode, which are to be expected considering the fact that the gap size in y -direction is greater than in x -direction (see geometry specifications in section 3.3.7).

No detrimental effect caused by the irradiation of the chips can be observed in the simulated scenarios. The average deviations remain within the tolerances and do not show higher variability in irradiated sensors. The standard deviations from the computed means for each position and scenario didn't change noticeably after irradiation. The loss in precision of damaged sensors in real conditions will probably be rather due to damaged noisy pixels and/or columns reporting a high number of counts or an increase in the noise, and not from a reduced charge collection. In scenarios with low particle numbers, however, the decrease in the number of collected charges may lead to higher performance loss, as seen in section 3.3.4.

3.4. Conclusions

Two versions (one and two dimensional) of a simple interpolation algorithm to bridge the gaps between chips and, in doing so, avoiding the systematic deviations in the beam position and width observed near those gaps, have been successfully implemented. Numerous tests (experimental and simulated, online and offline) prove the validity of the approach in minimizing said deviations up to gap widths (between the active areas) of around 1.2 mm (see figure 3.15). The algorithms help maintain the reconstructed beam parameters within the design tolerances and show an accuracy comparable to that of a Gaussian fit.

In the process, Allpix Squared simulation pipelines enhanced by TCAD electric field simulations and tuned to the HitPix detectors have been developed as well. There is agreement between the reconstruction performance observed in experimental and simulated data, as seen in figures from 3.13 and 3.14.

The geometry of a 5×5 demonstrator matrix was simulated using experimental data about the alignment precision in position and orientation. The simulated matrix was put under test in simulated scenarios including irradiated sensors and two different temperatures. There were no noticeable detrimental effects in simulations stemming from the irradiation (and therefore reduced collected charge, as shown in section 3.3.3) or the change in temperature. Simulations run on a simple 1×1 matrix nevertheless show a significant charge collection decrease of approximately 35% and a efficiency loss of the sensors of around 4%. After irradiation, the appearance of an approximately $5 \mu\text{m}$ insensitive area on the boundary regions between pixels was observed.

4. Graphical user interface for the HitPix detectors

During this work, a graphical user interface based on Plotly Dash [45] (and coded in Python) was designed to operate the HitPix detectors. It makes use of the already available Python scripts developed by Martin Pittermann and Bogdan Topko and consolidates them into a more user friendly interface, for which a user manual is presented in the following sections.

The application server can be started by typing `python ~/dash-main-interface.py` in a console. After that, the interface can be opened on a web browser by accessing the server's IP address stated in the console.

4.1. Home screen

The home screen of the application (figure 4.1) contains the controls necessary for a real time readout of the detector. The options in the navigation bar (fig. 4.1-1) give access to additional tools (fig. 4.1-2) to produce current-voltage-curves (IV-curves), pixel efficiency curves (s-curves) and to perform the DAC-tuning (both the latter based in charge injection measurements). Furthermore, the path of the folder in which the real time readout data should be saved can be set under *Configuration*. Advanced users can unlock additional detector settings by inputting the password under *Unlock settings*.

A text area showing the most important events of the home interface is provided on the right side of the page. The field can be enlarged by clicking and dragging the bottom right corner of the field.

4.1.1. Configuration section

The configuration section is depicted in fig. 4.1-3. Before starting a measurement with a given detector, the matching firmware has to be uploaded to the FPGA board. After selecting the correct file from the dropdown menu next to *Setup* (fig. 4.1-4), clicking on *Upload firmware* will initiate the upload process, which should be complete after some seconds.

Selecting the setup in the dropdown menu will also activate the *Data acquisition* section of the home screen (fig. 4.1-7). If the advanced settings are unlocked, the menus containing the device settings (fig. 4.1-5) and scan settings (fig. 4.1-6) will also appear within the configuration section. The menus can be unlocked at any time, even during measurements.

It should be noted that the selection of available firmware files depends on which files are present in the `firmware` folder in the GUI's main path. The names of these files have to coincide with the names set in the `defaults.py` python script for the GUI to be able to load the right settings and default values.

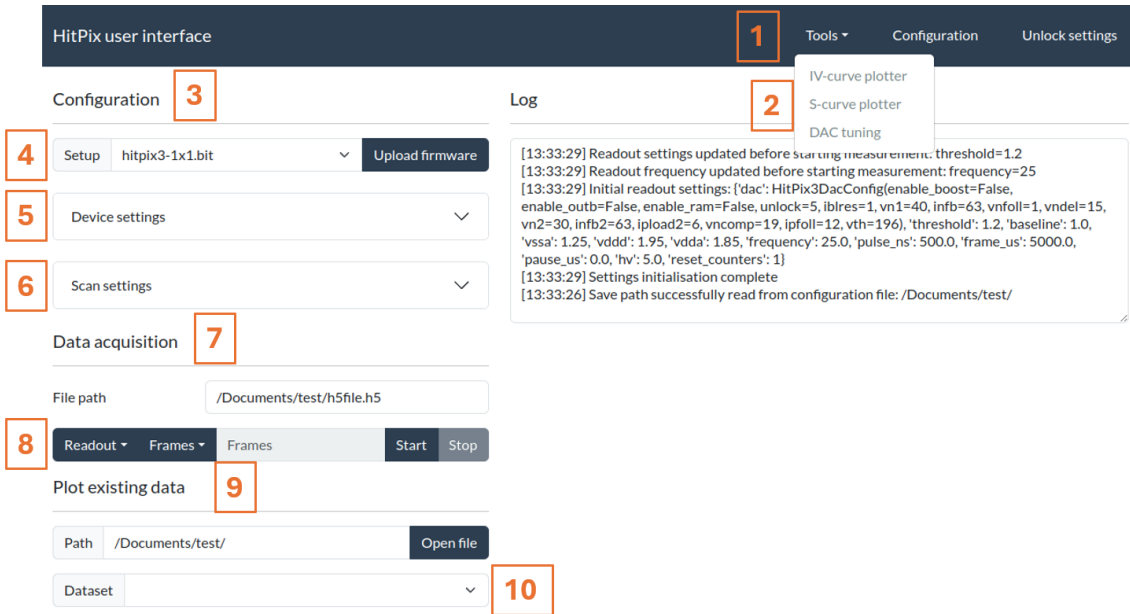


Figure 4.1.: GUI's homepage. **1:** Options in the navigation bar to access additional tools, set the default save folder for the measurement and unlock advanced settings (5-6). **2:** Dropdown menu to access the available additional tools. **3:** Detector configuration section. **4:** Setup selection and firmware upload. **5 and 6:** Device and scan settings only activated after unlocking them via the *Unlock settings* button. **7:** Data acquisition section. **8:** Readout mode (*counters* or *adders*, which can be chosen by clicking on *Readout*) and number of frames to record (*Frames* or *Continuous*, which can be set by clicking on *Frames*). **9:** Data plotting section. **10:** Dataset selection, available after loading the *h5* file by setting the path to it and clicking on *Open file*.)

4.1.2. Data acquisition section

The path to the folder which will contain the readout data is propagated from the input under *Configuration* in the navigation bar (fig. 4.1-1). The standard name for the data file is *h5file.h5*. The user may adapt this name before proceeding.

The readout can be performed in adders or counters mode. Clicking on *Readout* will open a dropdown menu to select one of the two. Furthermore, the interface can either record an indefinite number of frames or only a user defined number of them. This behaviour can be adjusted by clicking on *Frames* and selecting the desired option: *Frames* for a limited number of frames (which should be input to the right of the *Frames* menu) or *Continuous* for an indefinite number of frames (fig. 4.1-8).

After all has been set, the measurement can be started by clicking on the *Start* button. It will take some moments for the user to see the real time data in the histograms which will appear thereafter, since the software has to interface with the power supplies. The same holds if the measurement is stopped via the *Stop* button (it will take some seconds for the readout to be stopped properly).

Two rows of histograms will appear on the home screen after the measurement has started. The first one represents the real time measured number of hits per frame. In HitPix 3's adders mode, two graphs will appear in the first row: one for the *x*-axis adders projection and another one for the *y*-axis projection. The second row will show the result of summing up all hits over a time period, which can be reset by clicking on the graph itself.

An illustration of a live data acquisition is provided in figure 4.2.

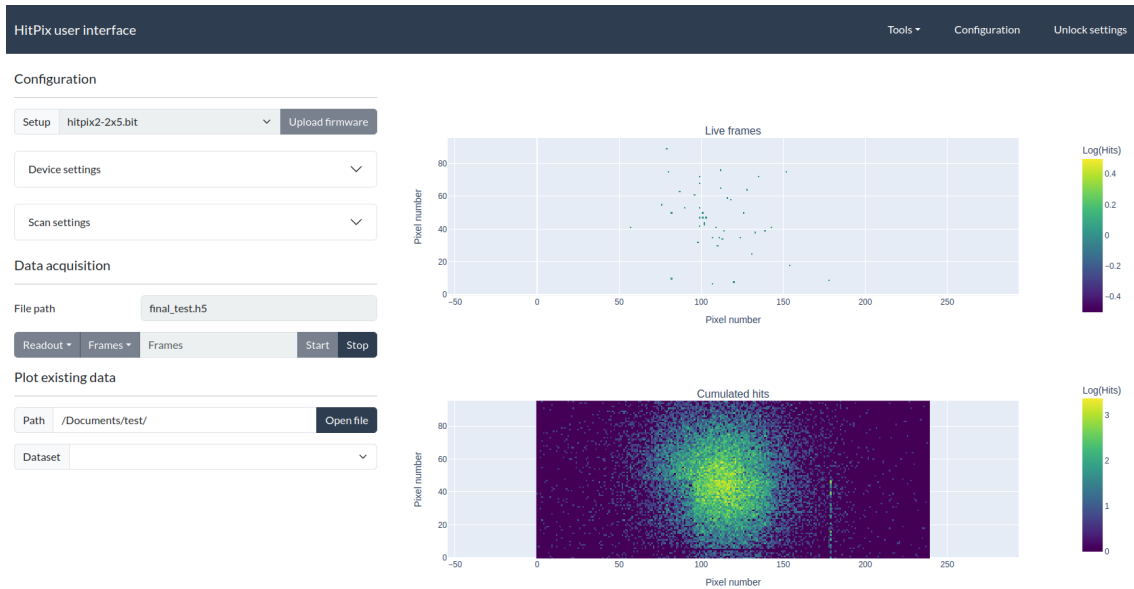


Figure 4.2.: GUI during data acquisition with a 2×5 matrix.

4.1.2.1. Advanced settings

The advanced settings section includes two dropdown menus: the *Device settings* (fig. 4.1-5), containing the different detector's configuration parameters (e.g. threshold, baseline and high voltages; readout frequency and frame size, etc.), and the *Scan settings* (fig. 4.1-6) for the scan mode. Which parameters are available depends on the setup selected in the dropdown menu of the configuration section.

The *Device settings* may be changed before or after the readout has started (with the exception of the frequency, which may only be set before the measurement's start). The changes made under *Device settings* are only applied after pressing enter on the input field. If changed during measurement, the interface will generate a new dataset for the readings performed using the new adjustment. The parameters used for each measurement are stored as attributes of the dataset in the *h5* file and can be consulted later.

The interface allows so-called *Scan measurements*, where the readout is performed for different detector parameters defined within an interval set by the user. More than one parameter to be scanned can be selected, the interface will then measure the selected number of frames for all possible combination of the chosen parameters. The three fields (*Start*, *Stop*, *Step*) have to be populated for each parameter to be scanned. Otherwise, the parameter will be ignored. The current state of the measurement can be viewed under *Device settings*. There, the parameter values will update according to the scan step being performed at each moment.

4.1.3. Plotting section

The measurements can be viewed after readout in the *Plot existing data* section of the home page (fig. 4.1-9). After the path to the file has been set, clicking on the *Open file* button will load the measurement, after which each dataset can be selected by using the respective dropdown menu on the right of *Dataset* (fig. 4.1-10).

Selecting a dataset from those displayed in fig. 4.1-10 will activate the histogram section of the homepage. The settings used to record the data will be displayed along a slider which can be adjusted to view different frames of the same dataset. An illustration is provided in figure 4.4.

Scan settings

threshold	start: 0.6-1.4	stop: 0.6-1.4	step: 0.01
baseline	start: 0.6-1.4	stop: 0.6-1.4	step: 0.01
vssa	start: 1.0-2.1	stop: 1.0-2.1	step: 0.01
vddd	start: 1.0-2.1	stop: 1.0-2.1	step: 0.01
vdda	start: 1.0-2.1	stop: 1.0-2.1	step: 0.01
hv	start: 0.0-120	stop: 0.0-120	step: 0.5
frame_us	start: 0.0-5000.0	stop: 0.0-5000.0	step: 1
pause_us	start: 0.0-0.0	stop: 0.0-0.0	step: 1.0
pulse_ns	start: 0.0-2500.0	stop: 0.0-2500.0	step: 50.0
dac.enable_boost	start	stop	step
dac.enable_outb	start	stop	step
dac.iblres	start: 0-63	stop: 0-63	step: 1
dac.vn1	start: 0-63	stop: 0-63	step: 1
dac.infb	start: 0-63	stop: 0-63	step: 1
dac.vnfol	start: 0-63	stop: 0-63	step: 1
dac.vndel	start: 0-63	stop: 0-63	step: 1
dac.vn2	start: 0-63	stop: 0-63	step: 1
dac.infb2	start: 0-63	stop: 0-63	step: 1
dac.ipload2	start: 0-63	stop: 0-63	step: 1
dac.vncomp	start: 0-63	stop: 0-63	step: 1
dac.ipfol	start: 0-63	stop: 0-63	step: 1
dac.vth	start: 0-255	stop: 0-255	step: 1

Figure 4.3.: Scan settings menu for a HitPix 3 detector. All three fields in a row (*Start*, *Stop*, *Step*) have to be populated, otherwise the program will ignore the input. Boolean parameters cannot be scanned.

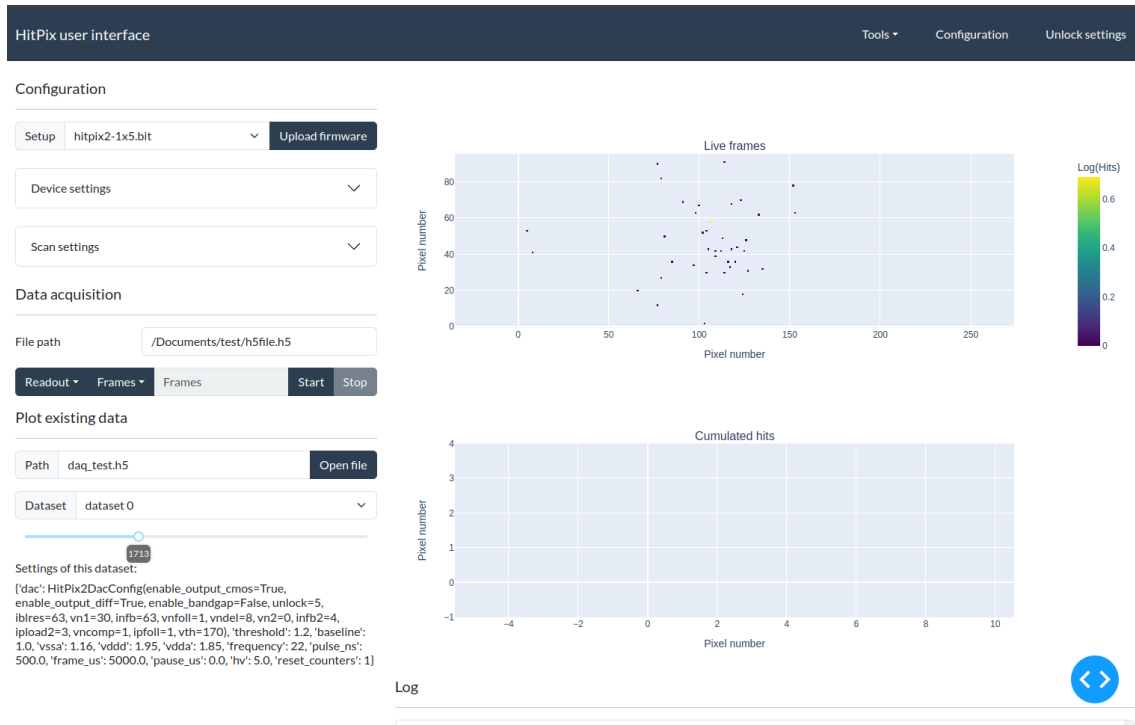


Figure 4.4.: GUI dataset viewer. Notice the slider on the lower left, which allows selecting the frames, and the stored information about the detector settings with which the dataset was recorded.

4.2. IV-curve measurement tool

The current-voltage-characteristic of the detector can be tested with the IV-curve tool (see figure 4.5). Before starting the measurement, the necessary parameters must be set: *Maximum voltage* to be tested, *Voltage step* and the *Compliance current*. The default output directory is the same as the one set in the home page and can be changed there as described in the previous section. It is necessary to add a filename and extension to the path before proceeding, as shown in fig. 4.5-2.

The measurement can be started by pressing the start button. The duration of the measurement will depend on the number of steps resulting from the inputs in the *Maximum voltage* and *Voltage step*.

After the measurement is finished, the results can be plotted under *Plot existing IV-curve data* by opening the file saved in the previous step. The generated graph is interactive. The user may hover over the different data points to view the values (fig. 4.5-3). Using the controls on the top side of the picture, it is also possible to download the plot, zoom into a specific region and move to different parts of the plot by clicking and dragging on the graph (fig. 4.5-4).

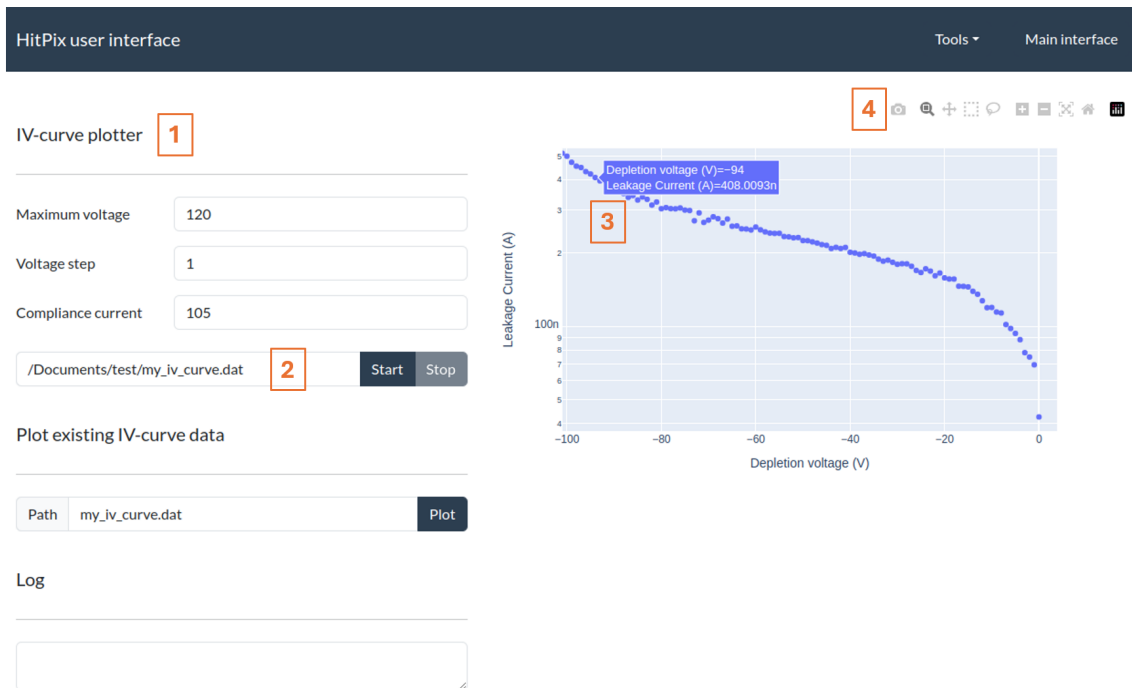


Figure 4.5.: IV-curve measurement tool. **1:** Plotter section, where maximum voltage, voltage step and compliance current have to be set before the measurement starts. **2:** The default folder (where the data file is saved) is propagated from the configuration in the main section, filename and extension have to be added to the path (in this case *my_iv_curve.dat*). **3:** Hovering over the curve shows details about the data points. **4:** Hovering over the graph activates the plot tools to download the graph, zoom into a part of it or move the graph.

4.3. S-curve measurement tool

To check the noise and threshold values of the detector, an S-curve may be measured, where the detection efficiency of the pixels is tested for different injection voltages (which inject different amounts of charge into the detector). This functionality is also available in the HitPix's GUI. The corresponding interface (see figure 4.6) is similar to that of the homepage and can be accessed through the tools dropdown menu. The s-curve tool works in two steps. First, the data is measured in the *S-curve data acquisition* section. The recorded data can be then plotted in the section below (*Plot s-curve data*).

The first section contains three menus: *General settings*, *Scan parameters* and *Set parameters* (figure 4.6-1 to 4.6-3), the last two of which are unlocked via the *Unlock settings* in the navigation bar along with the *Manual drivers* (fig. 4.6-4) in the *General settings* section.

The path of the new data file has to be set under the *General settings*. The default output file directory is propagated from the configuration in the homepage and can be changed there, only the file name and extension need to be appended to the existing path. Before starting the measurement, the setup must be chosen via the dropdown menu in order to load the necessary detector configurations. If the advanced settings are unlocked, the settings for the specific detector under test will appear next in the two menus on the right containing the parameters to be scanned and set. The number of injections (and injections per round) may also be modified from its default value, along with the injection voltage start, stop and step. The user can also decide if only a subset of the detector rows are to be measured. Lastly, the (external) manual control of the voltages can be chosen instead of the control via the interface. This is achieved by toggling the respective switches at the end of the *General settings* dropdown menu (fig. 4.6-4, available if the advanced settings are unlocked).

The working principle of the remaining two dropdown menus in the data acquisition section is very similar. The user can choose to scan a parameter or set it by toggling the respective switch and inputting the values. In the case of the scan, the *Counts* input value determines how many measurements are conducted within the interval defined by *Start* and *Stop*. An overview is provided in figure 4.7.

After all configurations have been set, the measurement may be started by clicking on the *Start* button at the end of the data acquisition section (fig. 4.6-5).

The recorded data can be viewed later by opening the file via the the input field and respective button at the bottom of the page. A new section will appear after processing the data which contains the relevant information about the S-curve. The graphs are interactive. By clicking on a pixel, the efficiency curve of that pixel is shown. If a parameter was scanned, the respective sliders will be available at the bottom to render the graphs corresponding to the different parameters applied during measurement. A depiction of plotted S-curve data is provided in figure 4.8

HitPix user interface

Tools Main interface Unlock settings

S-curve data acquisition

General settings 1

Output file /Documents/test/scurve.h5

Setup

Injections 500/50

Voltages 0 1.2 30

Rows all

Manual drivers

HV

VSSA 4

VDDD

VDDA

Scan parameters 2

Set parameters 3

Start 5

Plot s-curve data

Path /Documents/test/ Plot

Figure 4.6.: GUI S-curve measurement tool. **1:** General settings menu to configure the measurement. **2 and 3:** Dropdown menus to select parameters to be scanned or set to alternative values during the measurement. Only available in advanced mode. **4:** Switches to enable external manual control of the voltages. Only available in advanced mode. **5:** Button to start the S-curve measurement. The data may be plotted later in the section below (*Plot s-curve-data*).

HitPix user interface

Tools Main interface Unlock settings

S-curve data acquisition

General settings

Output file /Documents/test/scurve.h5

Setup hitpix3-1x1

Injections 500/50

Voltages 0 1.2 30

Rows all

Manual drivers

HV

VSSA

VDDD

VDDA

Scan parameters

threshold

Start Stop Count

baseline

Start Stop Count

vssa

Start Stop Count

vddd

Start Stop Count

vdda

Start Stop Count

Set parameters

threshold 1.2

baseline 1

vssa 1.25

vddd 1.95

vdda 1.85

Figure 4.7.: GUI's S-curve measurement tool with expanded menus. The menus are only populated if a setup has been selected in *General settings*. The switches beside each parameter need to be enabled for each parameter to be set or scanned.

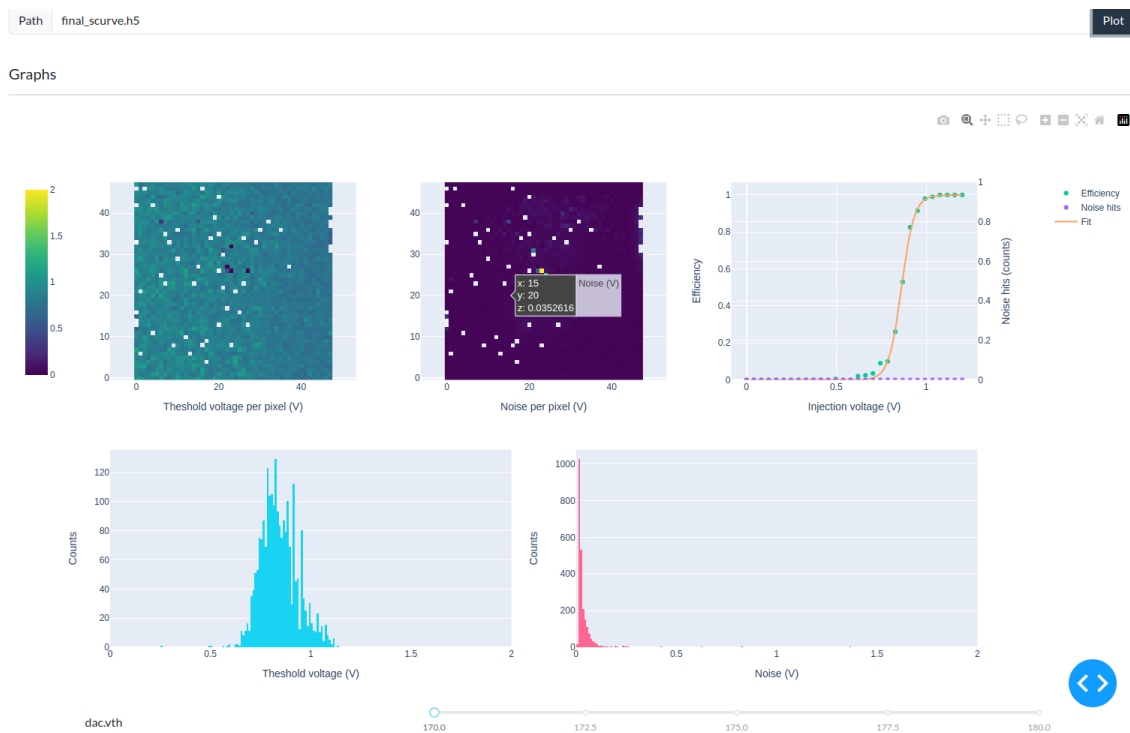


Figure 4.8.: GUI S-curve plot. Clicking on a pixel updates the efficiency curve on the top right to show the data for that pixel. In this example, the parameter *dac.vth* was scanned. The slider on the bottom can be used to see results for each value of that parameter.

4.4. DAC-tuning tool

Pixels within the detector matrix may display different sensitivity to signals, ones being more sensitive than others at different threshold values. This gives rise to an heterogeneous efficiency and, maybe more important, noise map of the detector, which cannot be properly fixed by setting a global threshold (which will affect all pixels in the same way). However, recent developments of HitPix 3 allow an individual pixel threshold adjustment and optimisation based in charge injection measurements measurements: the so-called DAC-tuning (only available from HitPix 3 on). The last tool in this GUI implements this procedure, which consists on two steps: first, a mask is generated which disables noisy pixels and excludes them from the tuning procedure. On the second step, this mask is used to perform the said pixel-by-pixel threshold adjustment.

The tool's layout is presented in figure 4.9. It features two sections corresponding to both the steps enumerated above. As usual, the setup must be selected before starting the measurement. Additional parameters may be set by unlocking the advanced settings in the toolbar, after which a dropdown menu will appear in each section. For each section, a path to a directory (where the tuning files will reside for each step of the process) must be provided.

The mask generation process is simple. The only parameter that the user is asked to provide is the *Noise threshold*, denoting the signal strength above which a pixel is considered as noisy.

Once the mask is created, the path to it must be input in the *DAC tune* section along with the number of injections performed by the s-curve measurement routine (from which the pixel efficiencies will be extracted) and the number of fit points used in the tuning process (between 3 and 16). After the setup selection, the user may start the tuning.

In both steps, and in order to save time, existing files can be used. This behaviour can be enabled by toggling the respective switches. After each step is complete, a graph will show the mask and the result of the DAC tuning procedure. The interface is presented in figure 4.9.

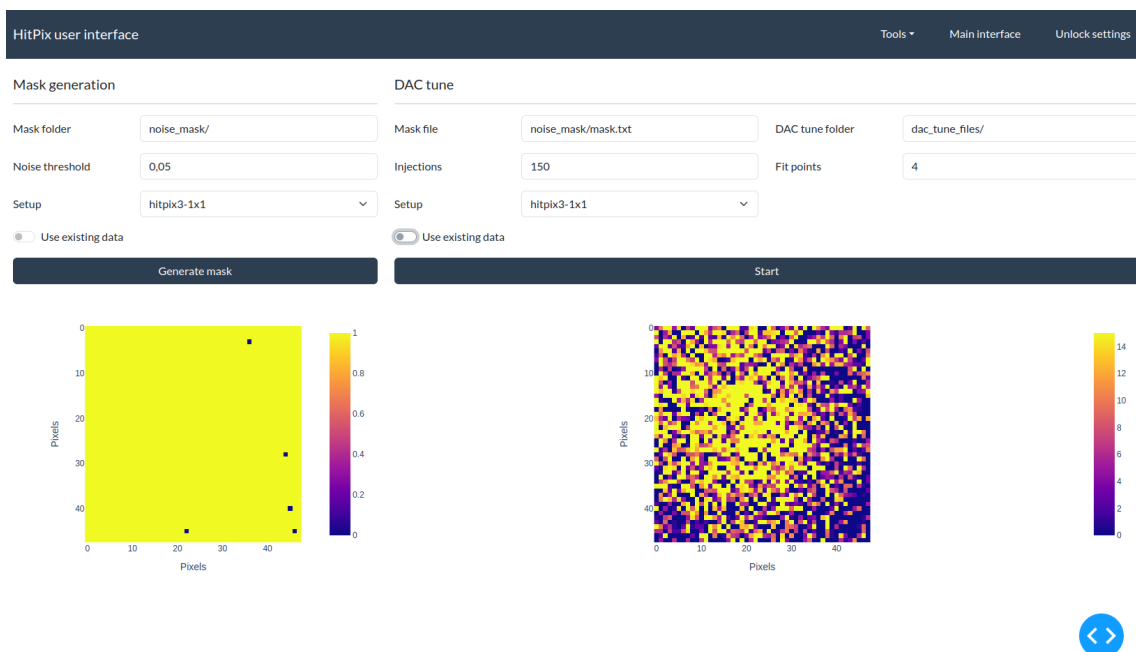


Figure 4.9.: DAC tuning tool. After each step is complete, the figures on the bottom will appear. The left map gives information about which pixels have been disabled (marked with a zero) and, therefore, will not be considered for the tuning. The right map shows the result of the tuning.

5. Conclusions and outlook

The foundation for a simulation framework able to reproduce the behaviour of the HitPix detector family has been set by means of the Allpix Squared and Sentauros TCAD simulation software suites. Thanks to these developments, the charge propagation can be more accurately reproduced in non-irradiated as well as in irradiated sensors considering, among other effects, the reduction of the depletion zone expected in damaged chips. Present and future iterations of HitPix chips (and chip arrays) can make use of the framework developed in this work to better understand the detectors and with the prospect of perfecting them for their application in clinical treatment scenarios. Some aspects have already been studied in this work, like the expected detector efficiency as well as the cluster size for irradiation with protons and carbons. Other aspects require further study. For instance, the detector response within magnetic fields can be researched further applying the same principles as the ones used to integrate the electric fields into the framework. Another open question is the effect of an inhomogeneous irradiation of a future HitPix matrix (in this work, the irradiation was assumed to be homogeneous throughout the matrix). Further improvements can also be made to the `DefaultDigitizer` module tailoring it to the more detailed specifications of the HitPix detectors.

In the scope of this work, the necessary algorithms were implemented to overcome the difficulties stemming from the fact that the detector consists of an array of individual chips with gaps between them. This generates deviations in the reconstructed beam parameters that are to be held within tolerance so as to ensure that the treatment plan is carried out adequately and that the patient is not irradiated unnecessarily. These algorithms are yet to be implemented on an FPGA and tested to determine how much faster the new beam monitoring concept is in comparison with the current system of multi-wire proportional chambers and ionisation chambers.

Lastly, a graphical user interface was designed to integrate the already available python scripts used at the present time to operate and read out the HitPix detectors via the command console. The proposed GUI implementation is flexible and allows an easy adaptation to new version of the sensors.

Appendix

A. Sentaurus simulations

A.1. Pixel topologies and geometry models

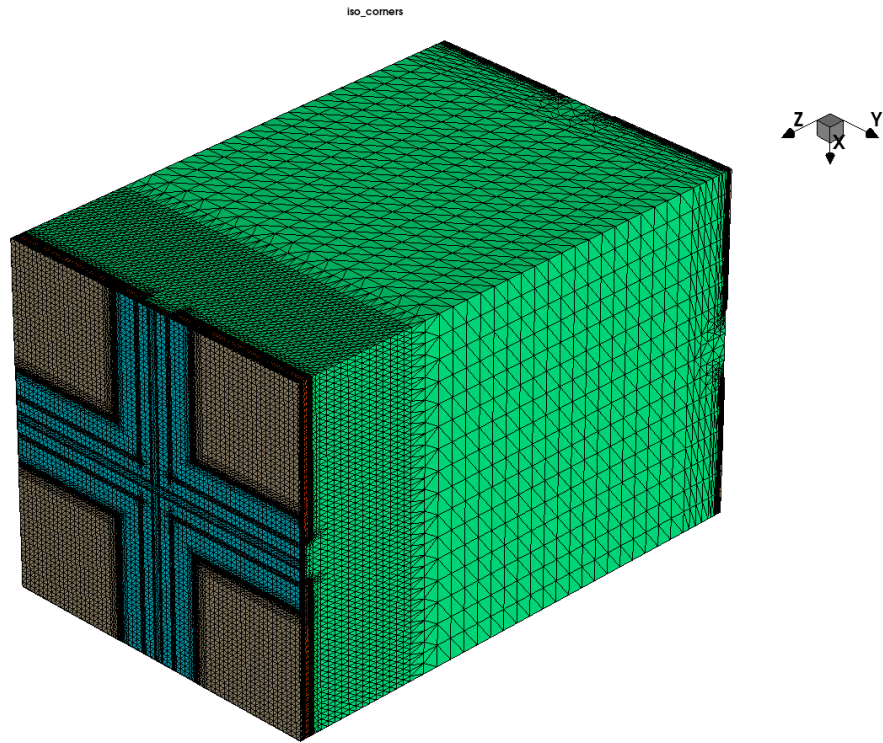


Figure A.1.: Mesh for the ISO topology. The metal contacts (grey) look the same in the front and in the back.

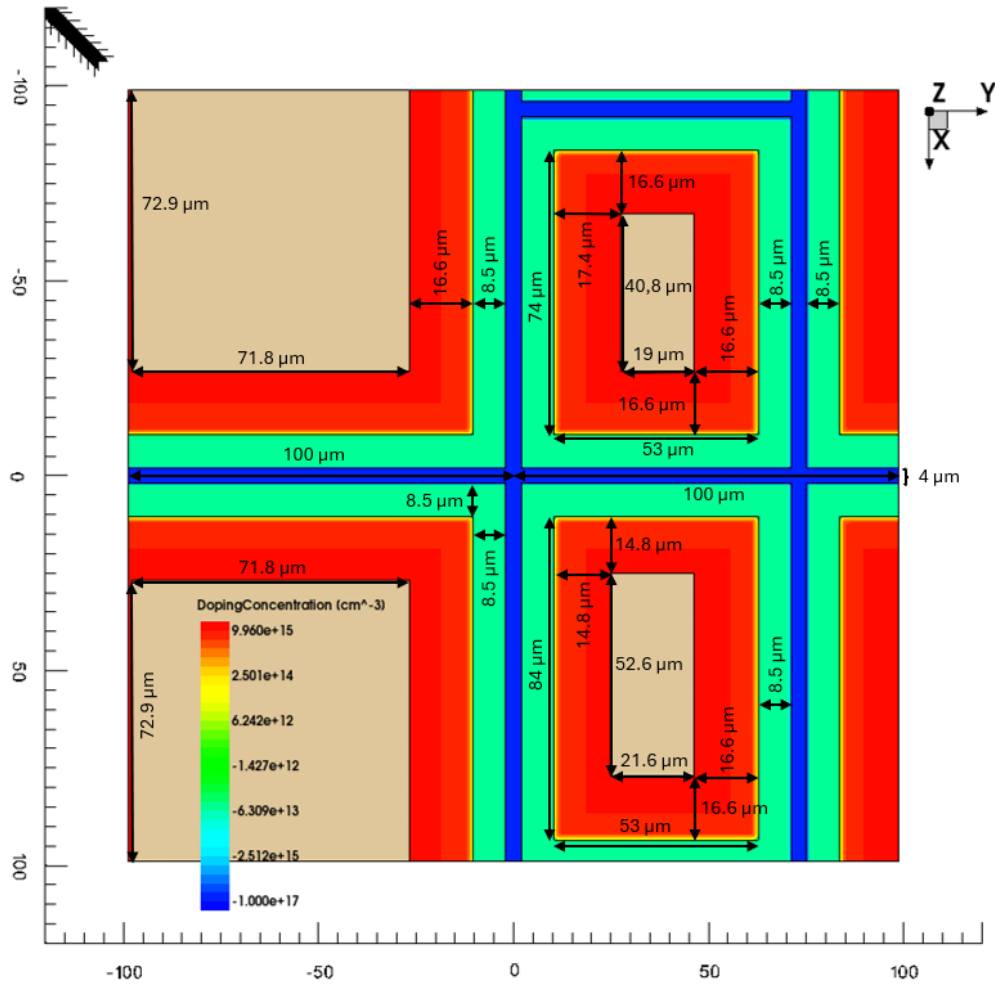


Figure A.2.: Top view of the simulation volume for the STD topology. Axes in micrometers. The silicon oxide layers are placed analogously as in the ISO topology and were omitted for visibility (see figure A.3, bottom subfigure). The grey areas are the metal contacts, the back contacts are the same as in the STD topology.

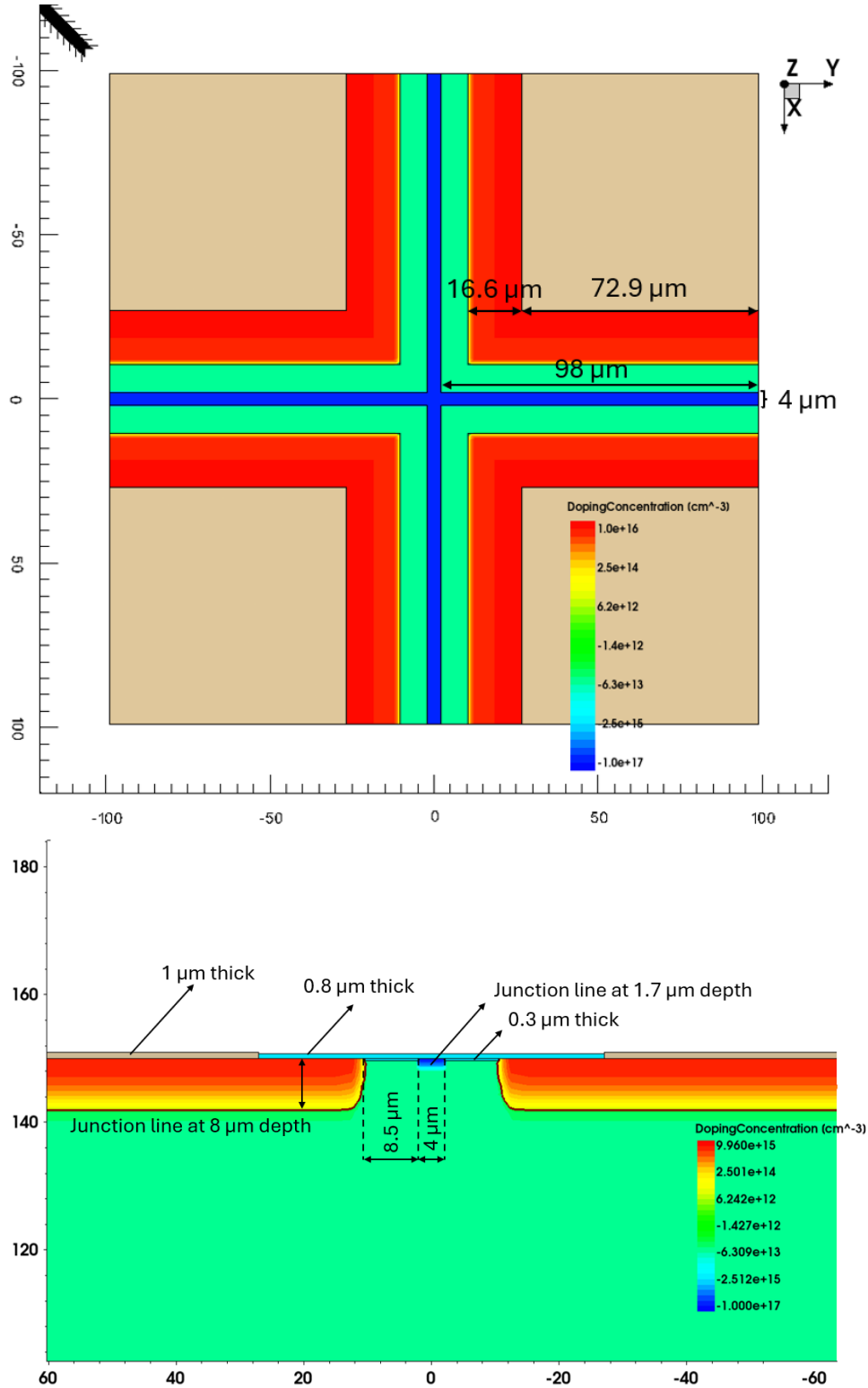


Figure A.3.: Top (first subfigure) and side (second subfigure) views of the simulation volume for the ISO topology. Axes in micrometers. On the first figure, the silicon oxide layers (light blue) were omitted for visibility. Two types of oxide layers were implemented (second figure): a surface oxide layer (0.8 μm thick) and STI (shallow trench isolation) layers (0.3 μm deep). The latter limit undesirable currents between the guards and the n-wells. The gray areas are the metal contacts. The same contacts are present at the back side of the pixels. The ISO topology is symmetric, so the dimensions can be propagated to the remaining axes and directions.

A.2. Sentaurus graphical interface

An overview of the Sentaurus Workbench interface is presented.

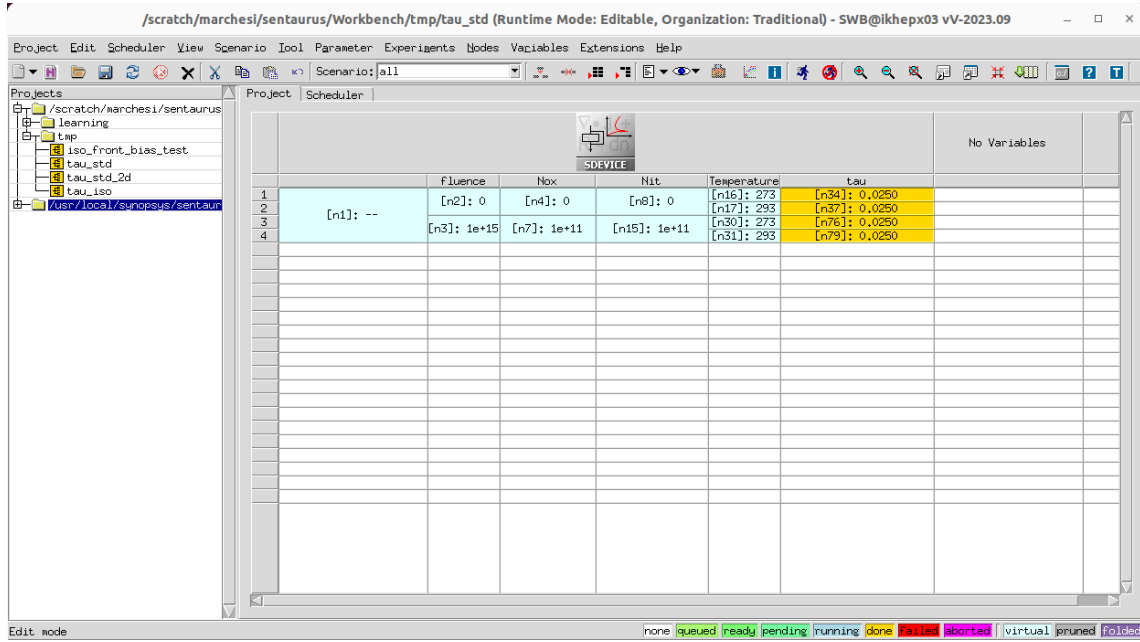


Figure A.4.: Sentaurus Workbench graphical interface, used to set the simulation environment. The individual cells with a number are called *nodes* and represent parameter values which are going to be used during the simulation. The nodes are arranged in a tree pattern, the last cell in the chain represents also the experiment to be conducted. For example: the first (n34) of the four simulations (n34, n37, n76, n79) is carried out using the parameters in the nodes n2, n4, n8, n16 and n34. The color of the last cells gives information about the status of the simulation.

B. AllPix Squared simulations

B.1. Interpolation

An additional example of the effect of the interpolation is provided in figure B.5, where also the overlapping profiles from different chips can be seen.

B.2. Time of arrival

The pixel time of arrival is presented in figure B.6 for the scenario simulated in section 3.3.3.

B.3. Real 2x5 geometry

The real 2x5 matrix geometry and local coordinate system used in section 3.3.5.1 for the matrix alignment is depicted in figure B.7.

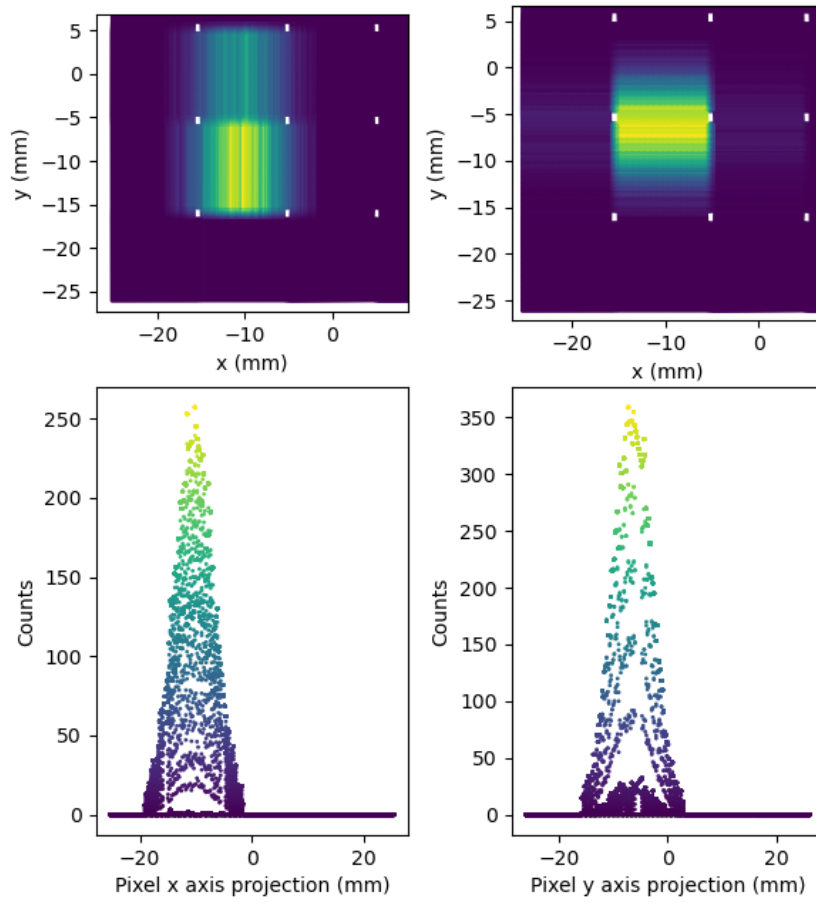


Figure B.5.: Section of an interpolated 5x5 matrix (top) with adders profile projections (bottom). Notice the overlapping profiles of chip rows/columns neighbouring those with the most hits. Also notice the effect of the interpolation, specially in the upper right picture at approximately $y = -5$. The hits at the horizontal gap between the detector chips is the result of a linear interpolation between the edges. The white spaces are areas that the interpolation algorithm does not reach, since it goes from edge to edge but not diagonally between corners.

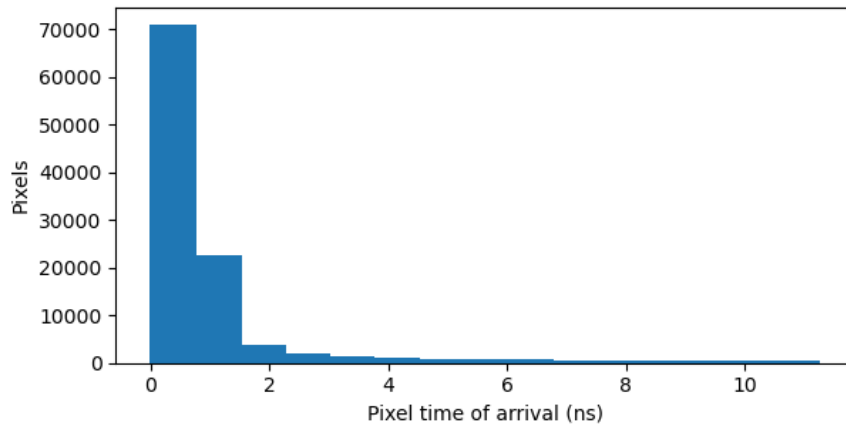


Figure B.6.: Time of arrival histogram depicting the time needed for the pixels to reach the charge threshold and, therefore, detect a hit. The simulation settings are those summarized in table 3.2 for a non-irradiated sensor at $T = 293$ K, 300 events, $N_{\text{tot}} = 180000$ and $N_{\text{event}} = 600$.

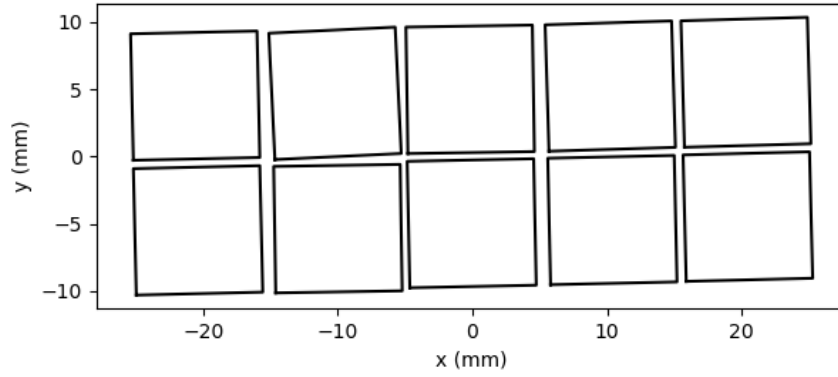


Figure B.7.: Real 2x5 geometry and coordinate system used for matrix alignment. The lines represent the borders of the chip's active area.

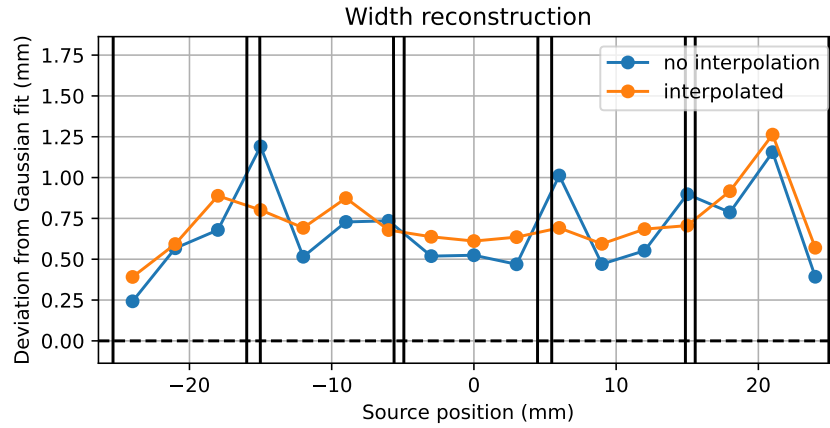


Figure B.8.: Width reconstruction without de-noising step in comparison with values obtained from a Gaussian fit. The dataset is the same as for figure 3.14.

B.4. Reconstruction without de-noising

As seen in section 3.3.8, the de-noising step can be too aggressive in some scenarios. However, it is necessary in order to limit the effect of outliers in the width reconstruction. One can see the importance of this effect in figure B.8, where the de-noising step was omitted during reconstruction for the same dataset as for figure 3.14. The width is greatly overestimated in comparison with the reconstruction using the Gaussian fit.

B.5. Detector definition

The following code creates the detector geometry in AllPix Squared, in this case for a 5x5 matrix with randomized misalignments in position and orientation of the chips. It is imported within the main configuration file with the statement `detectors_file`. To ensure the use of the same randomized geometry on different runs, the statement `random_seed_core` also has to be defined in the main file and has to be constant among runs with the same geometry.

A separate file defines the detector type. The code is also provided for the case of a chip with ISO or STD topology.

```
### Detector geometry definition ###
```

```
[chip00]
type = "chip_iso"
position = 20590um -21400um 0um
orientation_mode = "xyz"
orientation = 0deg 0deg 0deg
alignment_precision_position = 25um 25um 0mm
alignment_precision_orientation = 0deg 0deg 0.15deg
```

```
(...)
```

```
[chip04]
type = "chip_iso"
position = -20590um -21400um 0um
orientation_mode = "xyz"
orientation = 0deg 0deg 0deg
alignment_precision_position = 25um 25um 0mm
alignment_precision_orientation = 0deg 0deg 0.15deg
```

```
(...)
```

```
[chip44]
type = "chip_iso"
position = -20590um 21400um 0um
orientation_mode = "xyz"
orientation = 0deg 0deg 0deg
alignment_precision_position = 25um 25um 0mm
alignment_precision_orientation = 0deg 0deg 0.15deg
```

```
[PCB]
type = "box"
size = 100mm 100mm 2mm
position = 0mm 0mm 1151um
orientation = 0deg 0deg 0deg
material = "g10"
role = "passive"
```

```
[kapton_foil]
type = "box"
size = 100mm 100mm 25um
position = 0mm 0mm -5mm
orientation = 0deg 0deg 0deg
material = "kapton"
role = "passive"
```

```
### Detector type definition ###

type = "monolithic"
geometry = "pixel"

number_of_pixels = 48 48
pixel_size = 200um 200um
sensor_thickness = 300um
sensor_excess_top = 0um
sensor_excess_bottom = 0um
sensor_excess_left = 0um
sensor_excess_right = 0um
chip_thickness = 0um

[implant]

# For ISO topology
type = frontside
shape = rectangle
size = 179um 179um 8um
offset = 0um 0um # from the center of the pixel cell

# # For STD topology
# type = frontside
# shape = rectangle
# size = 179um 105um 8um
# offset = 0um 37um # from the center of the pixel cell

[support]
size = 9800um 9800um
thickness = 1um
location = sensor
material = "G4_SILICON_DIOXIDE"

[support]
size = 9800um 9800um
thickness = 1um
location = sensor
material = "aluminum"
```


Bibliography

- [1] A. Dierlamm, M. Balzer, F. Ehrler, U. Husemann, R. Koppenhöfer, I. Perić, M. Pittermann, B. Topko, A. Weber, S. Brons, *et al.*: *A beam monitor for ion beam therapy based on hv-cmos pixel detectors*. Instruments, 7(1), 2023. <https://doi.org/10.3390/instruments7010009>. Cited on pages v, 2, 3, 4, 8, 10, 11, and 12.
- [2] T. Royce and J. Efstathiou: *Proton therapy for prostate cancer: A review of the rationale, evidence, and current state*. Urologic Oncology: Seminars and Original Investigations, 37(9):628–636, 2019. <https://doi.org/10.1016/j.urolonc.2018.11.012>. Cited on page 2.
- [3] T. Oike, A. Niimi, N. Okonogi, *et al.*: *Visualization of complex dna double-strand breaks in a tumor treated with carbon ion radiotherapy*. Scientific Reports, 6, 2016. <https://doi.org/10.1038/srep22275>. Cited on page 2.
- [4] PDG, R. Workman, *et al.*: *Review of Particle Physics*. Progress of Theoretical and Experimental Physics, 2022(8):083C01, August 2022, ISSN 2050-3911. <https://doi.org/10.1093/ptep/ptac097>. Cited on page 2.
- [5] S. Combs, M. Ellerbrock, T. Haberer, D. Habermehl, A. Hoess, O. Jäkel, A. Jensen, S. Klemm, M. Mütter, J. Naumann, A. Nikoghosyan, S. Oertel, K. Parodi, S. Rieken, and J. Debus: *Heidelberg ion therapy center (HIT): Initial clinical experience in the first 80 patients*. Acta Oncologica, 49(7):1132–1140, 2010. <https://doi.org/10.3109/0284186X.2010.498432>. Cited on pages 2 and 3.
- [6] Ionenstrahl-Therapiezentrum, Heidelberg: *History of the HIT*. www.klinikum.uni-heidelberg.de/interdisziplinaere-zentren/heidelberg-ionenstrahl-therapiezentrum-hit/ueber-uns/geschichte, Accessed February 07, 2024. Cited on page 3.
- [7] M. Pittermann: *Evaluation of hv-cmos sensors in a beam monitoring system for ion therapy*, 2022. Cited on page 4.
- [8] https://commons.wikimedia.org/wiki/File:Band_structure_Si_schematic.svg, Accessed March 29, 2024. Cited on page 6.
- [9] https://commons.wikimedia.org/wiki/File:Silicon_doping_-_Type_P_and_N.svg, Accessed March 9, 2024. Cited on page 6.
- [10] F. Hartmann: *Evolution of Silicon Sensor Technology in Particle Physics*. Springer International Publishing AG, 2017, ISBN 978-3-319-64436-3. Cited on pages 6, 7, and 9.
- [11] https://en.wikipedia.org/wiki/Shockley%E2%80%93Ramo_theorem, Accessed Mai 29, 2024. Cited on page 7.
- [12] <https://commons.wikimedia.org/wiki/File:Pn-junction-equilibrium-graph.svg>, Accessed March 9, 2024. Cited on page 7.

- [13] W. Snoeys, G. Aglieri Rinella, H. Hillemanns, T. Kugathasan, M. Mager, L. Musa, P. Riedler, F. Reidt, J. Van Hoorne, A. Fenigstein, and T. Leitner: *A process modification for cmos monolithic active pixel sensors for enhanced depletion, timing performance and radiation tolerance*. Nuclear Instruments and Methods in Physics Research Section A: Accelerators, Spectrometers, Detectors and Associated Equipment, 871:90–96, 2017, ISSN 0168-9002. <https://www.sciencedirect.com/science/article/pii/S016890021730791X>. Cited on page 8.
- [14] F. Ehrler: *Characterization of monolithic HV-CMOS pixel sensors for particle physics experiments*. PhD thesis, Karlsruher Institut für Technologie (KIT), 2021. <https://doi.org/10.5445/IR/1000133748>, 54.12.01; LK 01. Cited on page 8.
- [15] <https://us.metoree.com/categories/cmos-sensor/>, Accessed March 25, 2024. Cited on page 8.
- [16] A. Weber, F. Ehrler, R. Schimassek, and I. Perić: *High-voltage cmos active pixel sensor chip with counting electronics for beam monitoring*. IEEE Transactions on Nuclear Science, 69(6):1288–1298, 2022. Cited on pages 11, 26, 27, and 39.
- [17] A. Weber: *Development of Integrated Circuits and Smart Sensors for Particle Detection in Physics Experiments and Particle Therapy*. PhD thesis, Heidelberg University, 2021. <https://doi.org/10.11588/heidok.00030650>. Cited on pages 11 and 14.
- [18] S. Spannagel, K. Wolters, D. Hynds, N. Alipour Tehrani, M. Benoit, D. Dannheim, N. Gauvin, A. Nürnberg, P. Schütze, and M. Vicente: *Allpix2: A modular simulation framework for silicon detectors*. Nuclear Instruments and Methods in Physics Research Section A: Accelerators, Spectrometers, Detectors and Associated Equipment, 901:164–172, 2018, ISSN 0168-9002. <https://www.sciencedirect.com/science/article/pii/S0168900218307411>. Cited on pages 13 and 29.
- [19] <https://www.synopsys.com/manufacturing/tcad.html>, Accessed on May 25, 2024. Cited on page 13.
- [20] *Sentaurus Device User Guide, Version V-2023.09, September 2023, Synopsis*. Cited on pages 13, 15, 16, and 18.
- [21] G. Masetti, M. Severi, and S. Solmi: *Modeling of carrier mobility against carrier concentration in arsenic-, phosphorus-, and boron-doped silicon*. IEEE Transactions on Electron Devices, 30(7):764–769, 1983. Cited on page 16.
- [22] S. Choo: *Theory of a forward-biased diffused-junction p-l-n rectifier—part i: Exact numerical solutions*. IEEE Transactions on Electron Devices, 19(8):954–966, 1972. Cited on page 16.
- [23] N. Fletcher: *The high current limit for semiconductor junction devices*. Proceedings of the IRE, 45(6):862–872, 1957. Cited on page 16.
- [24] E. Conwell and V. Weisskopf: *Theory of impurity scattering in semiconductors*. Phys. Rev., 77:388–390, Feb 1950. <https://link.aps.org/doi/10.1103/PhysRev.77.388>. Cited on page 16.
- [25] C. Canali, G. Majni, R. Minder, and G. Ottaviani: *Electron and hole drift velocity measurements in silicon and their empirical relation to electric field and temperature*. IEEE Transactions on Electron Devices, 22(11):1045–1047, 1975. Cited on page 16.
- [26] G. Hurkx, D. Klaassen, and M. Knuvers: *A new recombination model for device simulation including tunneling*. IEEE Transactions on Electron Devices, 39(2):331–338, 1992. Cited on page 16.

- [27] A. Chynoweth: *Ionization rates for electrons and holes in silicon*. Phys. Rev., 109:1537–1540, Mar 1958. <https://link.aps.org/doi/10.1103/PhysRev.109.1537>. Cited on page 16.
- [28] R. Van Overstraeten and H. De Man: *Measurement of the ionization rates in diffused silicon p-n junctions*. Solid-State Electronics, 13(5):583–608, 1970, ISSN 0038-1101. <https://www.sciencedirect.com/science/article/pii/0038110170901395>. Cited on page 16.
- [29] J. Slotboom and H. de Graaff: *Measurements of bandgap narrowing in si bipolar transistors*. Solid-State Electronics, 19(10):857–862, 1976, ISSN 0038-1101. <https://www.sciencedirect.com/science/article/pii/0038110176900435>. Cited on page 16.
- [30] J. Slotboom and H. de Graaff: *Bandgap narrowing in silicon bipolar transistors*. IEEE Transactions on Electron Devices, 24(8):1123–1125, 1977. Cited on page 16.
- [31] J. Slotboom: *The pn-product in silicon*. Solid-State Electronics, 20(4):279–283, 1977, ISSN 0038-1101. <https://www.sciencedirect.com/science/article/pii/0038110177901083>. Cited on page 16.
- [32] D. Klaassen, J. Slotboom, and H. de Graaff: *Unified apparent bandgap narrowing in n- and p-type silicon*. Solid-State Electronics, 35(2):125–129, 1992, ISSN 0038-1101. <https://www.sciencedirect.com/science/article/pii/003811019290051D>. Cited on page 16.
- [33] R. Eber: *Untersuchung neuartiger Sensorkonzepte und Entwicklung eines effektiven Modells der Strahlenschädigung für die Simulation hochbestrahlter Silizium-Teilchendetektoren*. PhD thesis, Karlsruhe Institute of Technology (KIT), 2013. Cited on pages 17, 19, and 20.
- [34] A. Morozzi, F. Moscatelli, T. Croci, and D. Passeri: *TCAD modeling of surface radiation damage effects: A state-of-the-art review*. Frontiers in Physics, 9, 2021, ISSN 2296-424X. <https://www.frontiersin.org/articles/10.3389/fphy.2021.617322>. Cited on pages 20 and 21.
- [35] P. Allport, F. Bögelspacher, K. Bruce, R. Canavan, A. Dierlamm, L. Gonella, P. Knights, I. Mateu, M. Moll, K. Nikolopoulos, B. Phoenix, T. Price, L. Ram, F. Ravotti, C. Simpson-Allsop, and C. Wood: *Experimental determination of proton hardness factors at several irradiation facilities*. Journal of Instrumentation, 14(12):P12004, dec 2019. <https://dx.doi.org/10.1088/1748-0221/14/12/P12004>. Cited on page 21.
- [36] W. Shockley and W. T. Read: *Statistics of the recombinations of holes and electrons*. Phys. Rev., 87:835–842, Sep 1952. <https://link.aps.org/doi/10.1103/PhysRev.87.835>. Cited on page 22.
- [37] R. Hall: *Germanium rectifier characteristics*. Phys. Rev., 83:228, 1951. Cited on page 22.
- [38] *Allpix Squared User Manual, Version v3.0.0-350-g4fa539bea*. <https://project-allpix-squared.web.cern.ch/usermanual/>, Downloaded November 21, 2023. Cited on pages 22, 23, 37, and 41.
- [39] O. Moritz: *Evaluation of the radiation hardness of HitPix3 MAPS*, 2024. Cited on pages 23, 26, 27, and 42.
- [40] B. Topko, M. Balzer, A. Dierlamm, F. Ehrler, U. Husemann, R. Koppenhöfer, I. Perić, M. Pittermann, and J. Naumann: *Monolithic hv-cmos sensors for a beam*

monitoring system of therapeutic ion beams. Journal of Instrumentation, 19(03):C03043, mar 2024. <https://dx.doi.org/10.1088/1748-0221/19/03/C03043>. Cited on pages 33 and 44.

- [41] https://en.wikipedia.org/wiki/Variance#Distribution_of_the_sample_variance, Accessed Mai 28, 2024. Cited on page 35.
- [42] https://geant4-userdoc.web.cern.ch/UsersGuides/PhysicsListGuide/html/reference_PL/FTFP_BERT.html, Accessed on May 8th 2024. Cited on page 37.
- [43] *Sentaurus Data Explorer User Guide, Version V-2023.09, September 2023, Synopsis*. Cited on page 37.
- [44] C. Schoemers, E. Feldmeier, J. Naumann, R. Panse, A. Peters, and T. Haberer: *The intensity feedback system at Heidelberg Ion-Beam Therapy Centre*. Nuclear Instruments and Methods in Physics Research Section A: Accelerators, Spectrometers, Detectors and Associated Equipment, 795:92–99, 2015, ISSN 0168-9002. <https://www.sciencedirect.com/science/article/pii/S0168900215007135>. Cited on page 46.
- [45] <https://dash.plotly.com/>, Accessed Mai 26, 2024. Cited on page 59.

Acknowledgements

*Deus meus es tu, et confitebor tibi; Deus meus es tu, et exaltabo te.
Confitebor tibi quoniam exaudisti me, et factus es mihi in salutem.
Psalm 118 (117)*

I would like to thank Professor Husemann for the opportunity to work in this project, as well as for the quick corrections to my draft. Also thanks Prof. Klute for agreeing to be my second reviewer and Dr. Alexander Dierlamm along with Bogdan Topko for their support and input during my thesis.

A ti mamá, y a ti, papá, infinitas gracias por todo. Habéis vivido conmigo todos estos años a pesar de la distancia. Vuestro apoyo ha sido crucial y decisivo. Me habéis enseñado y transmitido, entre otras muchas cosas, el valor de la persistencia. Gracias a vosotros estoy donde estoy y soy lo que soy.

Ein großes Dankeschön geht an Familie Schiel. Ihr auch habt mich auf diesem Weg begleitet, eine aktive Rolle übernommen und mir ermöglicht, in Deutschland ein neues Leben anzufangen. Danke, dass ihr mich als Teil eurer Familie zahlt. Auch ohne euch wäre ich nicht da, wo ich bin.

And, last but not least, to my dear friends, who have laughed and cried with me: thanks for being there in my deepest and in my best moments, for the regular company and encouragement.